



Calhoun: The NPS Institutional Archive
DSpace Repository

Theses and Dissertations

1. Thesis and Dissertation Collection, all items

2012

In situ Raman Spectroscopy Study of the Formation of Graphene from Urea and Graphite Oxide

Mowry, Michael N.

Monterey, California. Naval Postgraduate School

<http://hdl.handle.net/10945/17424>

This publication is a work of the U.S. Government as defined in Title 17, United States Code, Section 101. As such, it is in the public domain, and under the provisions of Title 17, United States Code, Section 105, is not copyrighted in the U.S.

Downloaded from NPS Archive: Calhoun



Calhoun is the Naval Postgraduate School's public access digital repository for research materials and institutional publications created by the NPS community. Calhoun is named for Professor of Mathematics Guy K. Calhoun, NPS's first appointed -- and published -- scholarly author.

Dudley Knox Library / Naval Postgraduate School
411 Dyer Road / 1 University Circle
Monterey, California USA 93943

<http://www.nps.edu/library>



NAVAL POSTGRADUATE SCHOOL

MONTEREY, CALIFORNIA

THESIS

***IN SITU* RAMAN SPECTROSCOPY STUDY OF THE
FORMATION OF GRAPHENE FROM UREA AND
GRAPHITE OXIDE**

by

Michael N. Mowry

September 2012

Thesis Advisor:
Second Reader:

Sebastian Osswald
Claudia Luhrs

Approved for public release; distribution is unlimited

THIS PAGE INTENTIONALLY LEFT BLANK

REPORT DOCUMENTATION PAGE			<i>Form Approved OMB No. 0704-0188</i>	
Public reporting burden for this collection of information is estimated to average 1 hour per response, including the time for reviewing instruction, searching existing data sources, gathering and maintaining the data needed, and completing and reviewing the collection of information. Send comments regarding this burden estimate or any other aspect of this collection of information, including suggestions for reducing this burden, to Washington headquarters Services, Directorate for Information Operations and Reports, 1215 Jefferson Davis Highway, Suite 1204, Arlington, VA 22202-4302, and to the Office of Management and Budget, Paperwork Reduction Project (0704-0188) Washington DC 20503.				
1. AGENCY USE ONLY (Leave blank)		2. REPORT DATE September 2012	3. REPORT TYPE AND DATES COVERED Master's Thesis	
4. TITLE AND SUBTITLE <i>In situ</i> Raman Spectroscopy Study of the Formation of Graphene from Urea and Graphite Oxide			5. FUNDING NUMBERS	
6. AUTHOR(S) Michael N. Mowry				
7. PERFORMING ORGANIZATION NAME(S) AND ADDRESS(ES) Naval Postgraduate School Monterey, CA 93943-5000			8. PERFORMING ORGANIZATION REPORT NUMBER	
9. SPONSORING /MONITORING AGENCY NAME(S) AND ADDRESS(ES) N/A			10. SPONSORING/MONITORING AGENCY REPORT NUMBER	
11. SUPPLEMENTARY NOTES The views expressed in this thesis are those of the author and do not reflect the official policy or position of the Department of Defense or the U.S. Government. IRB Protocol number ____N/A____.				
12a. DISTRIBUTION / AVAILABILITY STATEMENT Approved for public release; distribution is unlimited			12b. DISTRIBUTION CODE A	
13. ABSTRACT (maximum 200 words) Graphene, 10 or fewer atomic layers of carbon atoms, has attracted much attention during recent years due to its unique structure and exceptional physical properties. While there exist a wide range of potential applications, as with many nanomaterials, new synthesis techniques are required that allow for a production of graphene on an industrial scale. In this study, <i>in situ</i> Raman spectroscopy was used to study the formation and doping of graphene during urea-assisted thermal exfoliation of graphite oxide (GO), a promising new synthesis method that can be scaled to industrial levels. Thermogravimetric analysis (TGA), differential scanning calorimetry (DSC), and mass spectroscopy were used complementary to Raman spectroscopy to assist with the interpretation of the obtained data. Raman spectroscopy is a powerful characterization tool for the analysis of carbon nanomaterials, such as graphene. While several researchers have reported on the reaction of urea and GO, none of the studies found in literature has provided deeper insights on the evolution of the graphene structure and the simultaneous incorporation of nitrogen into the honeycomb lattice during synthesis. The knowledge gained from this work allows for a better understanding of the graphene production process and provides further evidence for the potential nitrogen-doping of graphene via deposition of urea.				
14. SUBJECT TERMS carbon nanomaterials, graphene, single layer graphite, 2-D graphite, Raman spectroscopy, thermogravimetric analysis, differential scanning calorimeter, mass spectroscopy			15. NUMBER OF PAGES 107	
			16. PRICE CODE	
17. SECURITY CLASSIFICATION OF REPORT Unclassified	18. SECURITY CLASSIFICATION OF THIS PAGE Unclassified	19. SECURITY CLASSIFICATION OF ABSTRACT Unclassified	20. LIMITATION OF ABSTRACT UU	

THIS PAGE INTENTIONALLY LEFT BLANK

Approved for public release; distribution is unlimited

***IN SITU* RAMAN SPECTROSCOPY STUDY OF THE FORMATION
OF GRAPHENE FROM UREA AND GRAPHITE OXIDE**

Michael N. Mowry
Lieutenant, United States Navy
B.S., Florida Institute of Technology, 2005

Submitted in partial fulfillment of the
requirements for the degree of

MASTER OF SCIENCE IN MECHANICAL ENGINEERING

from the

**NAVAL POSTGRADUATE SCHOOL
September 2012**

Author: Michael N. Mowry

Approved by: Sebastian Osswald
Thesis Advisor

Claudia Luhrs
Second Reader

Knox Millsaps
Chair, Department of Mechanical and Aerospace Engineering

THIS PAGE INTENTIONALLY LEFT BLANK

ABSTRACT

Graphene, 10 or fewer atomic layers of carbon atoms, has attracted much attention during recent years due to its unique structure and exceptional physical properties. While there exist a wide range of potential applications, as with many nanomaterials, new synthesis techniques are required that allow for a production of graphene on an industrial scale.

In this study, *in situ* Raman spectroscopy was used to study the formation and doping of graphene during urea-assisted thermal exfoliation of graphite oxide (GO), a promising new synthesis method that can be scaled to industrial levels. Thermogravimetric analysis (TGA), differential scanning calorimetry (DSC), and mass spectroscopy were used complementary to Raman spectroscopy to assist with the interpretation of the obtained data. Raman spectroscopy is a powerful characterization tool for the analysis of carbon nanomaterials, such as graphene. While several researchers have reported on the reaction of urea and GO, none of the studies found in literature has provided deeper insights on the evolution of the graphene structure and the simultaneous incorporation of nitrogen into the honeycomb lattice during synthesis.

The knowledge gained from this work allows for a better understanding of the graphene production process and provides further evidence for the potential nitrogen-doping of graphene via deposition of urea.

THIS PAGE INTENTIONALLY LEFT BLANK

TABLE OF CONTENTS

I.	INTRODUCTION.....	1
A.	GRAPHENE.....	1
	1. Structure.....	1
	2. Properties.....	3
	3. Potential Applications.....	4
	4. Synthesis.....	5
	5. Characterization of Carbon Nanomaterials.....	8
B.	RAMAN EFFECT	12
	1. Background	12
	2. Basic Theory.....	13
	<i>a. The “Classical” Approach.....</i>	<i>13</i>
	<i>b. The “Quantum” Approach.....</i>	<i>19</i>
C.	RAMAN SPECTROSCOPY.....	23
	1. Signal Intensity.....	23
	2. Raman Spectrometer Functional Description.....	24
	3. Uses and Advantages of Raman Spectroscopy.....	27
	4. Resonant Raman Spectroscopy	27
D.	THESIS OBJECTIVES.....	31
II.	EXPERIMENTAL.....	33
A.	MATERIALS	33
	1. Graphite Oxide.....	33
	2. Urea	33
	3. Production of Graphene via Thermal Exfoliation	34
B.	METHODS AND CHARACTERIZATION	35
	1. Raman Spectroscopy	35
	<i>a. Raman Experimental Parameters</i>	<i>37</i>
	<i>b. Determination of Experimental Parameters.....</i>	<i>37</i>
	2. Thermal Gravimetric Analysis, Differential Scanning Calorimetry, and Mass spectroscopy	41
	3. X-ray Diffraction.....	45
III.	RESULTS AND DISCUSSION	47
A.	THERMAL GRAVIMETRIC ANALYSIS.....	47
	1. Pure GO	49
	2. GO/urea 1:1	49
	3. GO and GO/urea 1:1 Major Differences	51
B.	MASS SPECTROSCOPY	52
	1. Pure GO	53
	2. GO/urea 1:1	54
	3. Nitrogen Containing Gases	55
C.	DIFFERENTIAL SCANNING CALORIMETRY	58
	1. Pure GO	59

2.	GO/urea 1:1	60
D.	X-RAY DIFFRACTION	61
E.	RAMAN SPECTROSCOPY	63
1.	Determination of Nitrogen Doping.....	64
2.	GO/urea 1:1 Experiment 1	65
3.	GO/urea 1:1 Experiment 2	72
IV.	CONCLUSION	83
	LIST OF REFERENCES	85
	INITIAL DISTRIBUTION LIST	89

LIST OF FIGURES

Figure 1.	Schematic diagram of graphitic structures (From [1]).	2
Figure 2.	Graphene electronic band structure (From [6]).	3
Figure 3.	SEM of Graphite Oxide (GO); thermally reduced graphene (GP _{TR}); chemically reduced graphene (GP _{CR}) (From [21]).	9
Figure 4.	Second order Raman spectra of 1-layer graphene, few layer graphene, and bulk graphite (From [25]).	12
Figure 5.	Induction of a dipole moment from exposure to an EM field (From [29]).	14
Figure 6.	Waveforms of Rayleigh and Raman scattering (From [29]).	16
Figure 7.	Discrete Rayleigh and Raman photon interactions (From [26]).	17
Figure 8.	Molecular Stretching effects on the first derivative of polarizability (From [28]).	18
Figure 9.	Generic Morse curve.	20
Figure 10.	Schematic representation of the Raman Spectrometer light path (Renishaw).	25
Figure 11.	Renishaw inVia Raman Spectrometer setup in NPS nanomaterials laboratory.	26
Figure 12.	Renishaw inVia Raman Spectrometer internal optics.	26
Figure 13.	Comparison between Standard Raman Spectroscopy and RR Spectroscopy for both Stokes and Anti-Stokes scattering (From [32]).	29
Figure 14.	Temperature Profile used for study.	34
Figure 15.	Experimental setup used for all Raman experimentation. The TS1500 high temperature stage is mounted under the spectrometer's microscope objective with the argon and cooling water connected.	36
Figure 16.	D1/G1 Intensity ratio vs. temperature for GO/urea 1:1 <i>in situ</i> Raman preliminary experiments varying argon gas flow rate.	40
Figure 17.	Diagram of NETZSCH STA449 F3 Jupiter (left) (NETZSCH), picture of setup in NPS laboratory (right).	42
Figure 18.	Diagram of the TA-QMS 403 Aëolos (left) (NETZSCH), picture of setup in NPS laboratory (right).	43
Figure 19.	Picture of the TGA/DSC and mass spectrometer coupled setup in NPS laboratory.	44
Figure 20.	Picture of the inside of NPS XRD (left), picture of NPS XRD outside (right).	46
Figure 21.	TGA of (left) pure GO and (right) GO/urea 1:1 mixture.	47
Figure 22.	TGA and 1 st derivative (dw/dT) of (left) pure GO and (right) GO/urea 1:1 mixture.	48
Figure 23.	TGA of 1 st derivative (dw/dT) of GO and GO/urea 1:1 overlay	51
Figure 24.	Mass spectroscopy results of Pure GO (left) and GO/urea 1:1 (right)	53
Figure 25.	TGA results and mass spectra for nitrogen containing gases.	56
Figure 26.	Mass spectra of nitrogen gases associated m/z for pure GO and GO/urea 1:1 mixture	57
Figure 27.	DSC initial heat-up results for (left) pure GO and (right) GO/urea 1:1	58

Figure 28.	Combined DSC of initial heat-up for pure GO (black) and GO/urea 1:1 (blue).....	59
Figure 29.	XRD results on produced GO powder.....	62
Figure 30.	XRD of GO and other materials (From [38] left, [8] right).....	62
Figure 31.	Curve Fitting of an arbitrary graphene sample Raman spectra.....	63
Figure 32.	Raman spectra of varying GO/urea concentrations.	64
Figure 33.	GO/urea Experiment 1, heating/cooling 1 Raman spectra.....	66
Figure 34.	GO/urea Experiment 1, heating/cooling 2 Raman spectra.....	67
Figure 35.	GO/urea Experiment 1, heating/cooling 3 Raman spectra.....	68
Figure 36.	GO/urea Experiment 1, D1 Position.	70
Figure 37.	GO/urea Experiment 1, G1 Position.	70
Figure 38.	GO/urea Experiment 1, D/G intensity ratio.	71
Figure 39.	GO/urea Experiment 2, heating/cooling 1 Raman spectra.....	73
Figure 40.	GO/urea Experiment 2, heating/cooling 2 Raman spectra.....	74
Figure 41.	GO/urea Experiment 2 Raman spectra.	75
Figure 42.	GO/urea Experiment 2, (left) D1 position and (right) G1 position.....	76
Figure 43.	GO/urea Experiment 2, D/G intensity ratio.	77
Figure 44.	GO/urea Experiment 2, D1/G1 intensity ratio.	77
Figure 45.	GO/urea Experiment 2, D1/G1 area ratio.	78

LIST OF TABLES

Table 1.	NPS Raman Spectrometer lasers	30
Table 2.	Raman experimental parameters.....	37
Table 3.	TGA/DSC experimental parameters.....	44
Table 4.	XRD measurement parameters.....	61

THIS PAGE INTENTIONALLY LEFT BLANK

LIST OF ACRONYMS AND ABBREVIATIONS

0D	Quasi-zero-dimensional
1D	Quasi-one-dimensional
2D	Two-dimensional
3D	Three-dimensional
AFM	Atomic force microscopy
DSC	Differential scanning calorimetry
ED	Electron diffraction
EDS	Energy dispersive x-ray analysis
EELS	Energy electron loss spectroscopy
EM	Electromagnetic
FET	Field-effect transistor
GO	Graphite oxide
HCl	Hydrochloric acid
HRTEM	High resolution transmission electron microscope
QHE	Quantum Hall effect
RR	Resonant Raman
SEM	Scanning electron microscope
$\text{SnCl}_2 \cdot 2\text{H}_2\text{O}$	Stannous Chloride
STM	Scanning tunneling microscopy
TEM	Transmission electron microscope
TGA	Thermal gravimetric analysis
UAV	Unmanned aerial vehicle
UUV	Unmanned undersea vehicle
XRD	X-ray diffraction
STDEV	Standard deviation
m/z	Mass-to-charge ratio

THIS PAGE INTENTIONALLY LEFT BLANK

ACKNOWLEDGMENTS

First, I would like to acknowledge the entire faculty and staff of NPS USW, physics, and Mechanical/Aerospace Engineering Departments. The experience that I have had through classroom instruction and laboratory work will prove to be invaluable throughout my naval career. All of my instructors have done an outstanding job allowing me to build academically upon my field experience as a naval officer which created a learning environment that has been more effective than any other during my lifetime. I would like to especially thank Dr. Daphne Kapolka for her guidance through the USW curriculum and Master's degree program.

I would also like to especially thank my thesis advisor, Dr. Sebastian Osswald, for his guidance and mentoring through the thesis writing process. Without his assistance and guidance, I would not have been able to create this document. Furthermore, I would like to thank Dr. Claudia Luhrs for her expert instruction on different materials characterization techniques and her assistance in constructing this thesis along with the collaboration of two of her thesis student, LT Ashley Maxson and LT Ryan Palaniuk.

Lastly, I would like to thank my wife, Alisha, and my son, Evan, for always standing by my side and consistently filling my life with joy.

THIS PAGE INTENTIONALLY LEFT BLANK

I. INTRODUCTION

A. GRAPHENE

1. Structure

Although the existence of graphene has been known for many years as the base material for three-dimensional (3D) graphite, until recently it was theorized that purely two-dimensional (2D) crystals were thermodynamically unstable and therefore could not exist in a free standing condition [1]. While, quasi-zero-dimensional (0D) (fullerenes), quasi-one-dimensional (1D) (nanotubes), and 3D crystals have been well documented, experimental data on 2D crystals remained sparse. In 2004, Andre Geim and Kostya Novoselov; who later received the 2010 Nobel Prize in Physics for their ground-breaking work, retrieved individual graphene layers from bulk graphite and interest into 2D graphene began to skyrocket [2]. Their work not only definitively showed that 2D crystals can exist, but also enabled the study of this novel material and its exceptional properties. For example, unlike any other materials, graphene crystals allow charge carriers to have a mean free path on the order of $0.5\text{ }\mu\text{m}$, which equates to charge carriers traveling thousands of interatomic distances without scattering [3].

Graphene is a one-atom-thick, flat sheet of carbon atoms bonded in a honeycomb lattice. It is the base structure that makes up other types of graphitic structures including fullerenes, carbon nanotubes, and graphite (see Figure 1). Graphene sheets have strong interatomic bonding and when stacked, the sheets are shifted horizontally resulting in the well documented AB stacking sequence with relatively weak Van der Waals-type interlayer bonding. These stacks of graphene sheets are what make up the commonly known graphite found in our daily lives [4].

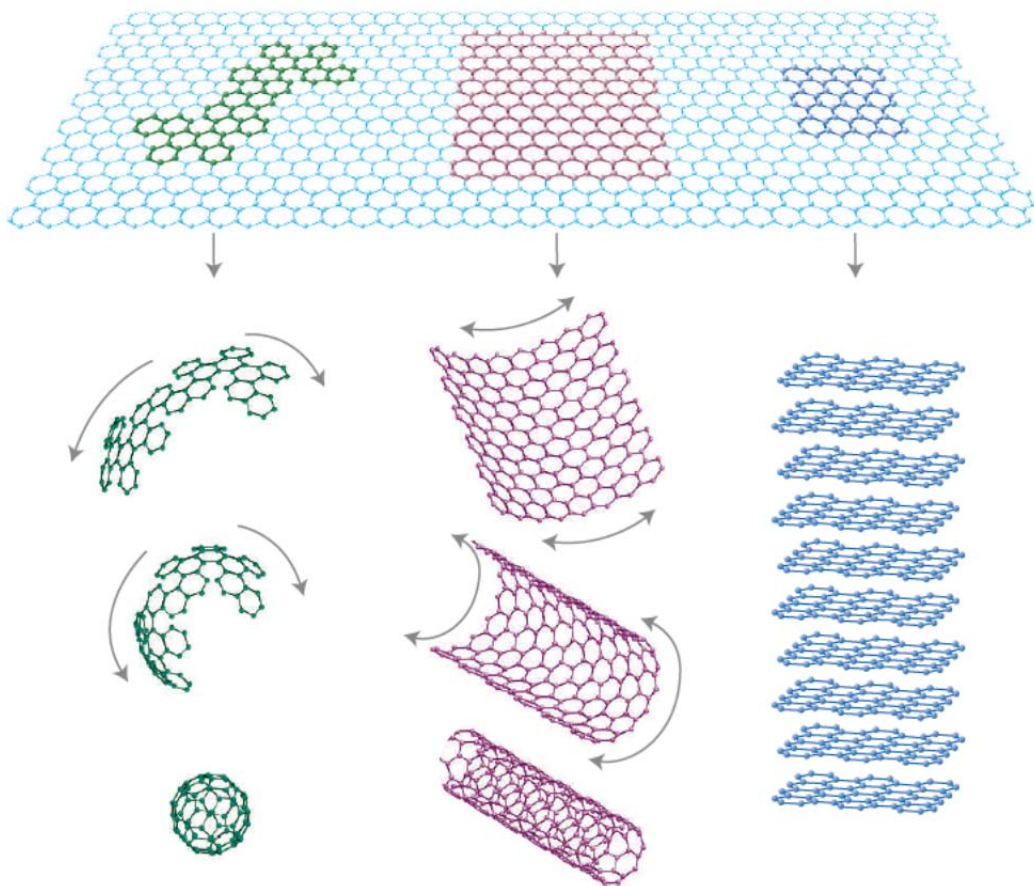


Figure 1. Schematic diagram of graphitic structures (From [1]).

Clearly any crystal that has a thickness of a single atom is a 2D crystal, and any crystal thick enough to be observed by the naked eye is a 3D crystal, but the exact thickness which constitutes an essentially 2D crystal depends on the material in question. In the case of graphitic structures, it has been shown that single layer graphene sheets have electronic properties that are very different from bulk graphite. As the number of graphene layers is increased, the material behaves more and more like bulk graphite. Once the graphene sheets are stacked 11 or more layers thick, the difference between the electronic structure from bulk graphite is only 10% [4]. Therefore, graphene shall refer to layers of carbon atoms with hexagonal symmetry that are not more than 10 layers thick and crystal structures that consist of more than 10 layers shall be considered thin graphite films.

2. Properties

The property that makes graphene so attractive to researchers around the world is its electronic structure. Single layered graphene is a zero band-gap semiconductor, while two layer graphene is truly a semi-metal but with a very small overlap [4]. As the number of layers of graphene increases, the band overlap increases until the crystal is essentially a thin graphite film (11+ layers). The two-dimensionality of the crystal gives rise to graphene being very resistant to the formation of crystalline defects such as dislocations. The inherent lack of crystalline defects allows for an extremely high electron (and hole) mobility. The electron mobility can be as high as $100,000 \text{ cm}^2\text{V}^{-1}\text{s}^{-1}$ at room temperature [1]. The high purity of graphene is also demonstrated by the existence of the quantum Hall effect at room temperature which has not been observed in any other material [5].

Graphene has a unique molecular structure of carbon atoms tightly packed into a benzene-ring structure, referred to as a honeycomb lattice. This unique structure and the fact that graphene is 2D, allows for the low energy band structure of graphene to be approximated as cones located at the corners of the 2D lattice (see Figure 2). At the Dirac point (the apex of these cones) the charge carriers in graphene exhibit a vanishing mass giving rise to a unique half-integer quantum Hall effect (QHE) [6]. The truly remarkable property is that graphene, unlike any other material known to date, exhibits the QHE even at room temperature. Several attempts have been made to observe the QHE in other semiconductors with small effective masses, but failed at temperatures above 30 K [5].

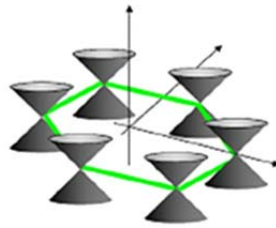


Figure 2. Graphene electronic band structure (From [6]).

Chemical doping of semiconductors is a long standing method of controlling the electronic properties of materials. However, because chemical doping adds more donor or acceptor ions to a material, the electron and hole mobility decreases with increasing

levels of doping. Interestingly, even when chemical doping was performed on graphene which introduced impurities in concentrations as high as 10^{12} cm^{-2} the electron and hole mobility remained essentially constant [7]. These experiments showed that graphene exhibits quasi-ballistic transport of electrons and holes.

3. Potential Applications

The discovery of 2D graphene and its revolutionary electronic properties as a zero band-gap semiconductor in 2004 lead to a whole set of potential applications. Over the past several decades dramatic advances have been made in the performance of “traditional” semiconductor materials, namely silicon. However, as we advance in the 21st century, increases in the performance of silicon seem to be reaching the fundamental limit and there is a growing interest in developing new materials that may replace silicon in the semiconductor industry [3]. Graphene can potentially be used to create transistors of very small sizes that require less energy and that could operate at higher frequencies than the current silicon-based devices. There are far too many potential uses of graphene to describe or even to imagine at this point in its development, however it is important to highlight some of the more advanced applications.

The ultimate dream for graphene based applications is to produce nanometer-sized, fully functional processors. However, the realization of this dream is still a long way off. Since graphene production is relatively inexpensive and scalable, its immediate application is in the area of composite materials. Some composite materials made of polymer nanofibers containing graphene nanoplatelets have proven to have an improved Young’s modulus as compared to other composite materials [8]. Graphene also exhibits dramatic electronic and structural changes when molecules are absorbed, which lend it to being the primary material for gas and bio sensors. In fact, graphene is so sensitive to molecular absorption that it is possible to create a device with the sensitivity to detect individual gas molecules [7]. In addition to functioning as an excellent detector, it has been suggested that graphene has the capacity to absorb a large amount of molecules and gases, including hydrogen [1], making graphene a candidate material for hydrogen storage applications.

In today's world there is an ever increasing demand for energy generation and energy storage with the proliferation of portable electronics, unmanned aerial vehicles (UAVs), unmanned undersea vehicles (UUVs), etc. Hence the main focus of much materials research, including graphene research, is in the area of electronics applications. As stated earlier, graphene is a candidate material for carbon-based field-effect transistors (FETs) [9]. In fact, dual gate graphene FETs have been synthesized with promising results [10]. Graphene is also a very intriguing material for energy storage devices including battery, fuel cell, and solar cell applications [1]. The promise of graphene as an energy storage material arises from the fact that it is a 2D material yielding an essentially infinite surface to volume ratio. This combined with the aforementioned electronic properties makes graphene a promising contender for future energy storage devices.

4. Synthesis

Because of the layered structure of graphite, it was known for many years that one could use the “scotch tape method” to removing graphene layers from bulk graphite. However, the resultant graphene layers were not conclusively shown to exist until Konstantin Novoselov and Andre Geim; for which they were awarded the Nobel Prize in physics in 2010, produced sheets of single layered graphene that were nearly macroscopic in the plane. They described the method as “drawing by chalk on a blackboard” [2]. This simple method of rubbing a graphite crystal onto a hard surface produced what can only be described as a pencil trace. The graphitic flakes that were produced were placed on an oxidized silicon wafer. They noticed that amongst the millions of graphite flakes produced, there were some flakes that were extremely thin. The oxidized silicon wafer was the key to observing the proverbial needle in the haystack.

In the 8 short years since the discovery of 2D crystals, an enormous number of methods have been proposed and tested for the fabrication of graphene. The similarities between 2D graphene and 1D carbon nanotubes have driven efforts to “grow” graphene on silicon substrates, as is done with carbon nanotubes [11]. Albeit successful, “growing” graphene is time consuming, relatively expensive, and difficult to scale up for industrial

applications. Another approach for the production of graphene that was adopted from other carbon nanostructures; such as nanodiamond, was to synthesize graphene sheets in the gaseous phase using a substrate-free, atmospheric-pressure microwave plasma reactor. Experiments showed that this method is capable of continuously producing single and bilayer, substrate-free graphene sheets [12]. Once again however, although this method is capable of producing bulk graphene, it is rather complicated and expensive for large scale commercial use.

A different approach is to attempt to chemically reduce graphitic structures, such as graphite oxide (GO), in order to remove the oxygen containing groups. This arises from the fact that the oxygen in GO alters the Van der Waals-like bonding between the graphite sheets and allows for the formation of stable thin sheets of GO when dispersed in an aqueous media [13]. Therefore, simply removing the oxygen groups from the GO will yield graphene. Different variations of this approach have been attempted by using reducing agents such as water with hydrazine [14]; an aqueous solution of HCl, $\text{SnCl}_2 \cdot 2\text{H}_2\text{O}$, and urea [15]; and a dimethylformamide solution [16], to mention a few. All of these attempts were successful in producing graphene sheets; however, in all cases the properties and the quality of the graphene sheets produced varied substantially.

Probably the most promising method of inexpensively producing large quantities of graphene for industrial application is the simple method of thermally exfoliating GO. Naturally, several processes have been developed and reported using this technique. It has been found that rapidly heating GO flakes to 1000 °C causes a violent release of gases and a visible volume expansion of the GO resulting in the formation of one and few-layered graphene sheets and has the added benefit of reversing the oxidation of the graphite [17]. It has also been found that the more rapidly GO flakes are heated, the greater the exfoliation and oxygen removal processes occur. This was shown by rapidly heating GO flakes by using a hydrogen discharge arc similar to methods used to produce carbon nanotubes [18].

One study investigated the effects of changing the oxidation and exfoliation parameters on the GO used. It was found that size of the resultant graphene flakes was approximately 10 μm and independent of the original graphite flakes (study used 400

and 45 μm graphite flakes) [19]. This study also found that the gaseous products formed during the thermal exfoliation were due to the exothermic decomposition of the hydroxyl and epoxide groups of the GO and not from vaporization of other introduced compounds. Therefore it is this exothermic reaction that adds sufficient heat to the GO sample allowing for rapid pressure buildup leading to exfoliation. The graphene produced by this method was found to be approximately 80% single graphene sheets [19]. A similar study found that during oxidation of graphite flakes, it is essential to remove the 0.34 nm inter-graphene layer spacing that can be seen in x-ray (XRD) and electron diffraction (ED) [20]. It is important to ensure that there is no residual water in the GO prior to thermal expansion as the vaporization of water is an endothermic reaction which tends to counteract the exothermic reaction of the GO thermal exfoliation. If the graphite flakes are properly prepared and adequately dried, the GO will undergo a volumetric expansion of 500–1000 times the original volume during the thermal exfoliation process [20].

Perhaps the most intriguing variant of the GO thermal exfoliation method to produce graphene sheets is the method of mixing a solid precursor (namely urea) with GO flakes prior to thermally expanding the GO. The urea serves as an expansion-reduction agent which produces volatile species that will expand the GO upon thermal decomposition of the urea, which occurs at lower temperatures than the previously mentioned methods. It has been shown that the expansion caused by urea decomposition is sufficient to overcome the inter-layer graphene bonding and produce single layer graphene [8]. The species produced by the decomposition of urea are also reducing agents which very effectively remove the oxygen containing groups from the GO. This method is very promising as it does not require the use of solvents or stabilizers eliminating the need to remove them after graphene production. It is also capable of producing graphene at more modest temperatures and heating rates than previously mentioned methods [8], and it is based on using the widely available materials of graphite and urea. These qualities all lend this process nicely to being inexpensively scaled up for industrial applications.

5. Characterization of Carbon Nanomaterials

As with any material, there are several techniques available to study the formation process of graphene and the resulting graphene sheets. In order to first confirm the existence of 2D crystallites, potential crystallites were identified using visual microscopy on an oxidized silicon wafer and then positively identified as 2D crystallites using atomic force microscopy (AFM) [2]. AFM continues to be the most prevalent characterization technique for graphene [2], [9], [11], [13], [14], [16–20] as it is a relatively inexpensive piece of equipment that has the resolution capable of measuring a single atomic thickness thereby confirming the presence of a 2D crystal [2]. Due to the electronic structure of graphene discussed earlier, scanning tunneling microscopy (STM), which operates on slightly different principles than AFM but produces a similar output, has also been used by several authors [9], [11], [18]. However, after the graphene revolution in the materials science area, several other characterization techniques have been determined for which graphene shows distinctive signatures.

Another common method of observing GO and graphene is via a scanning electron microscope (SEM) or a transmission electron microscope (TEM) [2], [8], [11], [12], [14–16], [18], [19], [21], [22]. The SEM clearly shows the carpet-like surfaces of GO in contrast to the crumpled sheets of graphene [21]. Using a TEM can then demonstrate that these surfaces observed in the SEM are actually extremely thin sheets of material (see Figure 3). A TEM can also be used to perform electron diffraction (ED), which gives information as to the graphene lattice parameters and structural order of the crystal; and energy electron loss spectroscopy (EELS), which gives information as to the bonding environment in the sample. However, ED [11], [12] and EELS [12] have seldom been used to characterize graphene [11], [12]. Additionally, a high resolution transmission electron microscope (HRTEM) can be used to observe graphene as it gives near atomic resolution of the graphene sheets. Just as the TEM can be used to perform ED, given the appropriate equipment (a backscattered electron detector), an SEM has the additional advantage of being able to conduct elemental analysis of the samples [21]. By coupling either an SEM or a TEM with an x-ray detector, either piece of equipment can

perform energy dispersive x-ray analysis (EDS), which has been used by numerous authors for elemental determination [13-16], [18], [21].

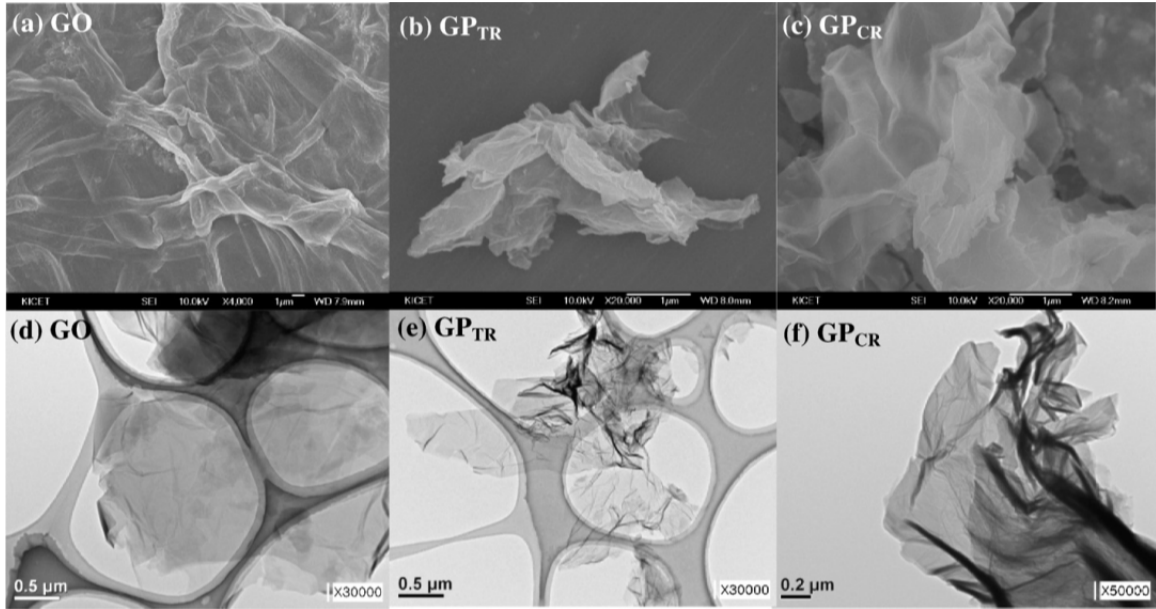


Figure 3. SEM of Graphite Oxide (GO); thermally reduced graphene (GP_{TR}); chemically reduced graphene (GP_{CR}) (From [21]).

As alluded to previously, XRD is a common analysis method for the characterization of GO and graphene samples. XRD data shows a very distinctive shift from graphite flakes to GO when oxidized and to graphene when thermally exfoliated. Graphite flakes have a characteristic (002) diffraction peak at approximately $2\theta = 26.6^\circ$ when using CuK α radiation. A simple application of Bragg's Law;

$$n\lambda = 2d \sin \theta, \quad (1.1)$$

where: n = order of reflection, λ = x-ray wavelength, d = interlayer spacing, and θ = refraction angle. This corresponds to an interlayer spacing of 3.35 \AA [18]. Once oxidized, the (002) diffraction peak for GO appears between 10.6 and 12.6° , corresponding to an interlayer spacing between 8.3 and 7.025 \AA , respectively [8], [18]. Finally, after thermally exfoliating the GO, the XRD patterns do not show any strong (002) diffraction peak rather they exhibit a much broader peak from 20 - 30° showing that the stacking of graphene layers is disordered [8], [18]. All of the techniques mentioned to this point have

proven to be very useful tools for characterizing the base materials used to produce graphene; namely graphite flakes, GO, and solid precursors, and the resultant graphene sheets. However, without additional highly specialized and expensive equipment, none of these techniques can be performed during the graphene production process. Even with the appropriate equipment, *in situ* studies using the above techniques are extremely challenging.

One method of studying the graphene production process of thermal exfoliation is using thermal gravimetric analysis (TGA) which is typically coupled with differential scanning calorimetry (DSC). This technique allows a sample of GO by itself or mixed with any precursor to be heated in a furnace thereby thermally exfoliating the GO to produce graphene, all the while measuring for any weight or energy changes in the sample (TGA and DSC, respectively). This technique clearly shows the weight loss of GO as a function of temperature and under the appropriate heating conditions different steps of weight loss can be observed corresponding to removal of absorbed water and decomposition of the surface groups attached to the GO [16]. If any precursors were mixed with the GO, then DSC/TGA analysis can further be broken down to show the decomposition of the GO and the precursors as a function of temperature [8]. TGA/DSC analysis is also performed in a controlled atmosphere of the users choosing and therefore is a very versatile technique as graphene formation can be studied using an inert argon atmosphere or adding oxygen, hydrogen, nitrogen, etc. or any combination thereof to the atmosphere [18]. Additionally, TGA/DSC instruments are very easily coupled with a mass spectrometer which can then measure the evolved gases from the sample as a function of time/temperature. Although this technique has proven to be very useful for studying the formation of graphene produced from thermally exfoliated GO, it cannot be used to positively identify the resultant material as 2D graphene as it provides insights into the graphene formation reactions, but does not offer structural information on the as-produced materials

Lastly, Raman spectroscopy is a technique that allows for an *in situ* study of the formation process of graphene from thermal exfoliation of GO (or GO with any precursor) and is capable of positively identifying the resultant material as 2D graphene.

A Raman spectrometer is also a relatively inexpensive piece of equipment as compared to an SEM or TEM, which makes this technique accessible to more research groups around the world than some of the more expensive and specialized techniques previously mentioned. Raman spectroscopy is easily performed *in situ* by measuring the Raman spectra through a sealed stage while heating the sample in an inert atmosphere, as was done in this study. Raman spectroscopy is also a non-destructive technique that allows for a rapid characterization of graphene as opposed to other positively identifying techniques such as AFM or STM. Raman spectroscopy is capable of positively identifying one, two, or few layer graphene due changes in the electronic structure of graphene as it increases in layers [23] as well as characterizing the transition of bulk graphite to GO which is used for the production of graphene [24]. Defects in the crystal lattice produce characteristic peaks that are distinctive to graphene and very different to the corresponding peaks in bulk graphite. Additionally, as the number of graphene layers increases, these peaks show a slow morphology tending towards bulk graphite (see Figure 4), allowing for positive identification of 2D and few layer graphene. At approximately 10 layers, the Raman spectra is nearly indistinguishable from that of bulk graphite which corresponds nicely to the electron structure of graphene, thin film graphite and bulk graphite discussed earlier.

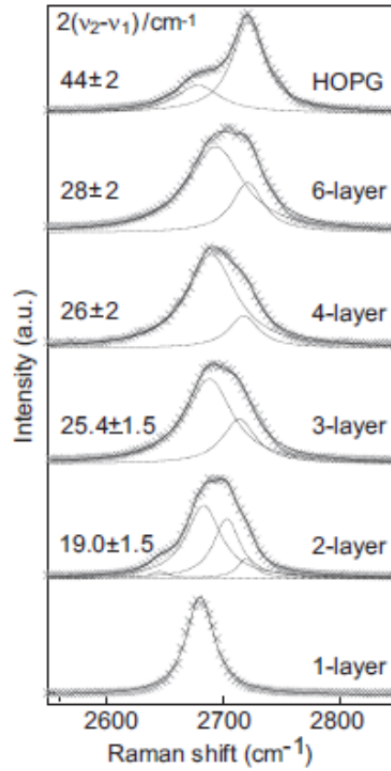


Figure 4. Second order Raman spectra of 1-layer graphene, few layer graphene, and bulk graphite (From [25]).

B. RAMAN EFFECT

1. Background

Raman spectroscopy is a widely available tool which utilizes the inelastic scattering of light to characterize the physical and chemical structure of materials as well as identify the composition of materials. The inelastic scattering of light (termed the Raman effect) was first postulated by Adolf Smekal in 1923 and later named after Sir Chandrasekhara Venkata Raman who experimentally observed this phenomenon in 1928 [26]. Sir Raman was awarded the Nobel Prize in Physics in 1930 “for his work on the scattering of light and the discovery of the effect named after him” [27]. The Raman effect is simply that when light; or any electromagnetic (EM) radiation, interacts with matter some of that light will be scattered. By collecting the scattered light, it has been shown that some of this light has a different frequency than the incident light. Later it

was determined that the exact nature of this frequency shift is a property of the material and the incident EM radiation, and therefore this technique could be used as a characterization tool.

2. Basic Theory

a. The “Classical” Approach

There are two different methods to conceptualize the Raman effect: the “classical” approach and the “quantum” approach. First the classical approach, utilizes classical wave theory to describe the scattering of light by matter including inelastic scattering which is the basis of the Raman effect. This approach is based on the fact that the scattering of light from a molecular structure originates from the interaction of an EM field (light) with the electronic structure of the molecule [28]. This interaction is characterized by the incident EM field inducing a dipole moment in the sample by disturbing the electronic charge distribution of the molecules according the formula for an induced dipole moment, μ .

$$\mu = \alpha E \quad (1.2)$$

In this equation, α is the molecular polarizability, which is simply a proportionality factor between the induced dipole moment; μ , and the external EM field; E . Figure 5 illustrates the induction of a dipole moment in a molecule by exposing the molecule to an external EM field (both a field produced by charged plates and a photo-electric field).

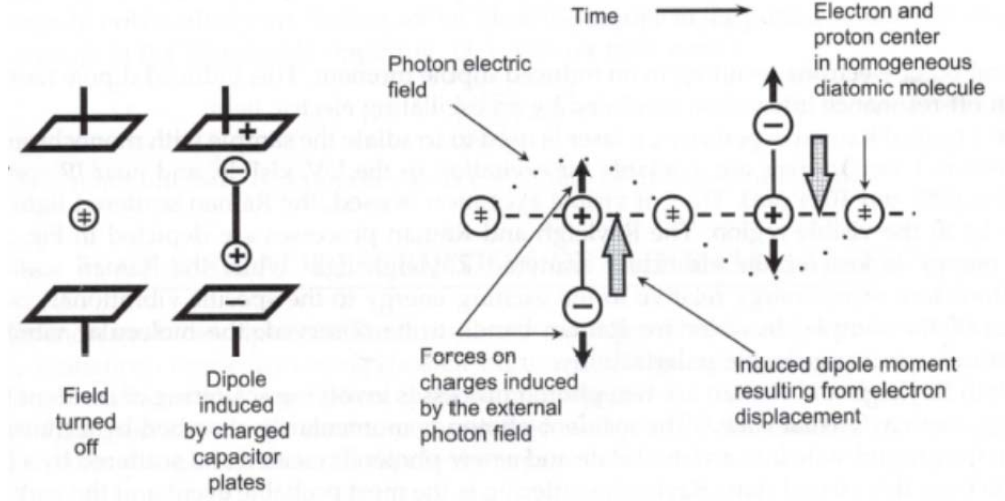


Figure 5. Induction of a dipole moment from exposure to an EM field (From [29]).

The concept that in nature all things will continuously adjust to minimize the overall energy of a system extends to the molecular nuclear geometry. Since the nuclear geometry of a molecule is constantly changing, the polarizability of an electronic system is also constantly changing and therefore cannot be treated as a constant quantity [28]. In order to account for this effect it is necessary to perform a Taylor series expansion of the polarizability around the equilibrium nuclear geometry, Q_0 .

$$\alpha = \alpha(Q) = \alpha_0 + \sum_{q=1}^N \left[\left(\frac{\partial \alpha}{\partial q} \right)_{q_0} \cdot q + \frac{1}{2} \left(\frac{\partial^2 \alpha}{\partial q \partial q'} \right)_{q_0 q'_0} \cdot q \cdot q' + O(q^3) \right] \quad (1.3)$$

where, Q represents the group of individual normal modes q [28]. Additionally since the EM field is characterized by its vector amplitude \vec{E}_0 and its oscillation frequency ω_0 , the real part of the EM field is expressed as

$$\vec{E} = \vec{E}_0 \cdot \cos(\omega_0 t) \quad (1.4)$$

Now by using a representative mode q ; which is excited by a characteristic frequency ω_q , q can be expressed as

$$q = q_0 \cdot \cos(\omega_q t) \quad (1.5)$$

Then, by only considering the first order Taylor expansion and simply substituting (1.5) into (1.3) then substituting the result and (1.4) into (1.2), yields [28]

$$\mu(t) = \left[\alpha_0 + \left(\frac{\partial \alpha}{\partial q} \right)_{q_0} \cdot q_0 \cdot \cos(\omega_q t) \right] \cdot E_0 \cdot \cos(\omega_0 t) \quad (1.6)$$

Finally, to obtain the electrical harmonic approximation, simply re-write (1.6) using the standard trigonometric formula for the product of cosines.

$$\begin{aligned} \mu(t) &= \alpha_0 \cdot E_0 \cdot \cos(\omega_0 t) \\ &+ \frac{1}{2} \left(\frac{\partial \alpha}{\partial q} \right)_{q_0} \cdot q_0 \cdot E_0 \cdot \cos[(\omega_0 - \omega_q)t] \\ &+ \frac{1}{2} \left(\frac{\partial \alpha}{\partial q} \right)_{q_0} \cdot q_0 \cdot E_0 \cdot \cos[(\omega_0 + \omega_q)t] \end{aligned} \quad (1.7)$$

Equation (1.7) is composed of three distinct components, each representing a different type of scattering based upon the interaction between the frequency of the incident EM field (the laser frequency) and the mode excitation frequency. The first term; $\alpha_0 \cdot E_0 \cdot \cos(\omega_0 t)$, represents Rayleigh scattering [28]. In this case, essentially no energy from the incident EM radiation is absorbed by the sample and therefore the scattered EM radiation is of the same frequency as the incident EM radiation. Rayleigh scattering is by far the dominant mechanism for radiation scattering from materials, however it does not produce any nuclear motion [26] and therefore contains no information as to the material's nuclear structure [28].

The second term; $\frac{1}{2} \left(\frac{\partial \alpha}{\partial q} \right)_{q_0} \cdot q_0 \cdot E_0 \cdot \cos[(\omega_0 - \omega_q)t]$, represents one type

of inelastic scattering dubbed Stokes scattering. In this process, energy from the incident EM radiation is transferred to the material resulting in a downshift in the scattered frequency which then oscillates at a frequency equal to the difference between the incident EM radiation frequency and the mode excitation frequency. Information as to the sample's molecular structure is contained in this scattered radiation due to the frequency

dependence on ω_q [28]. This is the typical scattered radiation measured and presented as Raman spectroscopy; however it is very weak as compared to Rayleigh scattering as only one in approximately every 10^6 to 10^8 photons scatter in this fashion [26].

The last term; $\frac{1}{2} \left(\frac{\partial \alpha}{\partial q} \right)_{q_0} \cdot q_0 \cdot E_0 \cdot \cos[(\omega_0 + \omega_q)t]$, represents the other

type of inelastic scattering dubbed Anti-Stokes scattering. In this process, energy is given off by the material and combines with the energy of the incident EM radiation resulting in an upshift in the scattered frequency which then oscillates at a frequency equal to the addition between the incident EM radiation frequency and the mode excitation frequency. The Anti-Stokes spectrum is identical to the Stokes spectrum however due to the very unusual nature of material giving off energy, Anti-Stokes scattering is typically a much weaker signal based upon the thermal energy of the sample material [26], [28].

These three distinct effects can also be visualized as the derivative of the polarizability of the molecule producing a modulation of the dipole moment oscillation. The resultant radiation waveform can then be resolved into the three types of scattering described above as shown in Figure 6.

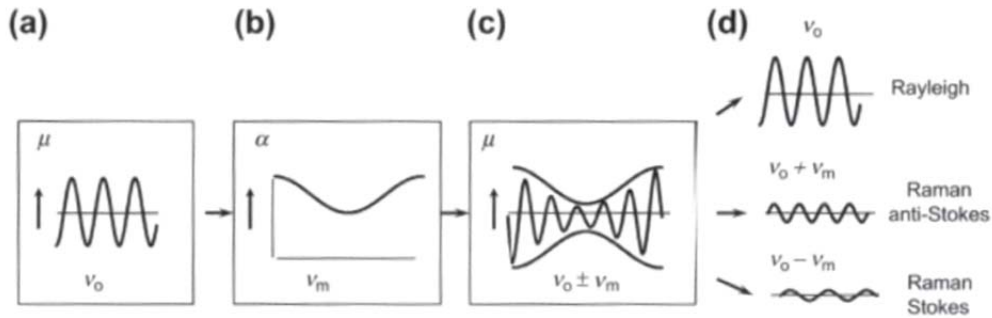


Figure 6. Waveforms of Rayleigh and Raman scattering (From [29]).

From a semi-quantum standpoint (described in detail later in this chapter), the scattering processes described above mathematically can also be visualized as the incident photons interacting with a molecule causing that molecule to increase to a higher, but unstable energy vibrational state (see Figure 7). In this visualization, Rayleigh

scattering can be seen as a molecule immediately dropping back down to its original state resulting in no energy change in the incident photons. Stokes scattering can be seen as the molecule immediately dropping back down to a slightly higher energy state than the original state resulting in a loss of energy of the incident photon. Finally Anti-Stokes scattering can be seen as the molecule immediately dropping down to a slightly lower energy state than the original state resulting in a gain of energy of the incident photon.

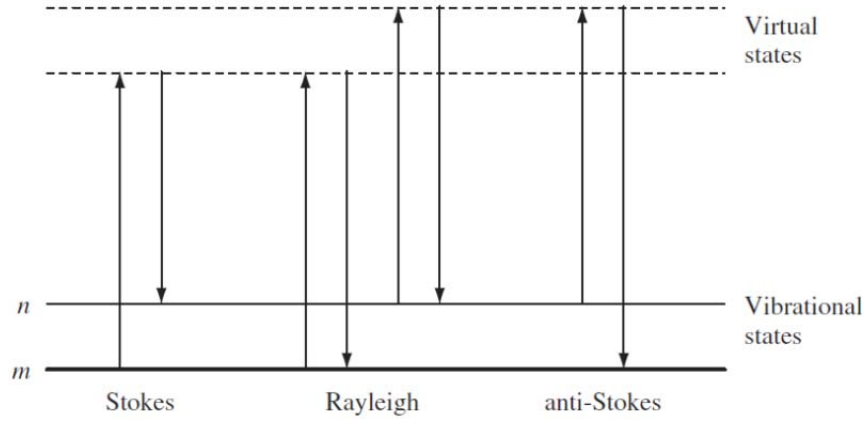


Figure 7. Discrete Rayleigh and Raman photon interactions (From [26]).

It is important to realize that based upon the mathematical model presented earlier, in order for a sample to have Raman scattering, that is to say be “Raman active,” the derivative of the electronic polarizability at the equilibrium position must be non-zero $\Rightarrow \left(\frac{\partial \alpha}{\partial q} \right)_{q_0} \neq 0$. In contrast, in order for a sample to undergo infrared

absorption, the derivative of the induced dipole moment must be non-zero $\Rightarrow \left(\frac{\partial \mu}{\partial q} \right)_{q_0} \neq 0$

A material is only Raman active when the molecule undergoes symmetric stretching of the interatomic bonds. During symmetric stretching, the internuclear distance between atoms is either expanding or contracting, resulting in a positively or negatively changing polarizability of the molecule, respectively, and therefore a non-zero derivative of polarizability. While at the same time the overall dipole moment of the molecule remains essentially constant and therefore there is no infrared absorption by the molecule. On the

other hand, if the molecule undergoes asymmetric stretching, the overall dipole moment is constantly changing and therefore the molecule is undergoing infrared absorption, while at the same time the overall polarizability of the molecule is essentially harmonic with a derivative of zero and therefore the molecule is not Raman active. Figure 8 is provided as an excellent illustration of this principle.

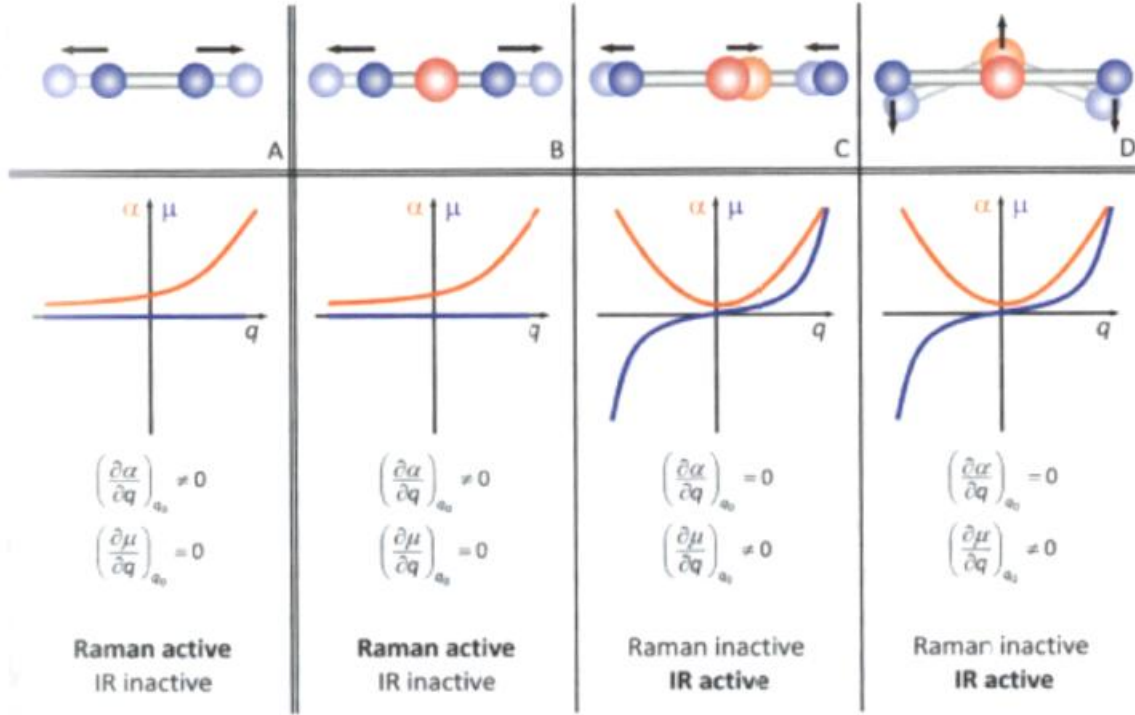


Figure 8. Molecular Stretching effects on the first derivative of polarizability (From [28]).

As mentioned previously, very little of the incident radiation undergoes inelastic scattering, but it is this scattering that gives rise to Raman spectroscopy. Looking at only the Stokes scattering in order to calculate the observed intensity from a Raman spectroscopy experiment, i.e.,

$$\mu^{\text{Stokes}}(t) \propto \left(\frac{\partial \alpha}{\partial q} \right)_{q_0} \cdot q_0 \cdot E_0 \cdot \cos[(\omega_0 - \omega_q)t] \quad (1.8)$$

The induced dipoles act as a Hertzian dipole from which the power emitted is calculated as [28]

$$P = \frac{|\ddot{\mu}|^2}{6\pi \cdot \epsilon_0 \cdot c^3} = \frac{q_0^2}{12\pi \cdot \epsilon_0 \cdot c^3} \cdot \left(\frac{\partial \alpha}{\partial q} \right)_{q_0}^2 \cdot (\omega_0 - \omega_q)^4 \cdot E_0^2 \quad (1.9)$$

Since the intensity seen from the Raman experiment is proportional to the overall power emitted from the induced dipole moment [28], [29]

$$I_{\text{Stokes}} \propto \left(\frac{\partial \alpha}{\partial q} \right)_{q_0}^2 \cdot (\omega_0 - \omega_q)^4 \cdot E_0^4 \quad (1.10)$$

Equations (1.7) and (1.10) constitute the result of the classical approach to Raman spectroscopy. They both show the dependence on experimental parameters of incident frequency and intensity; ω_0 and E_0^2 , respectively, as well as the dependence on the molecular parameters of excitation frequency and the changing polarizability; ω_q and $\left(\frac{\partial \alpha}{\partial q} \right)_{q_0}$, respectively [28].

Although the classical approach to the Raman effect provides an intuitive understanding as to the interactions between light and matter, it does not provide as much information as to the relationship between molecular properties and Raman scattering as the quantum approach. This is due to an inherent lack of the classical approach to account for the quantized nature of vibrations [26]. The classical approach is therefore not able to explain important processes in Raman spectroscopy such as resonance Raman scattering and surface-enhanced Raman scattering [28].

b. The “Quantum” Approach

The quantum approach to the Raman effect differs from the classical approach in that it takes into account the discrete nature of energy/vibrational states in a molecular structure. The idea of discrete energy levels in a molecule is best conceptualized by looking at a typical Morse curve for a general molecule (Figure 9).

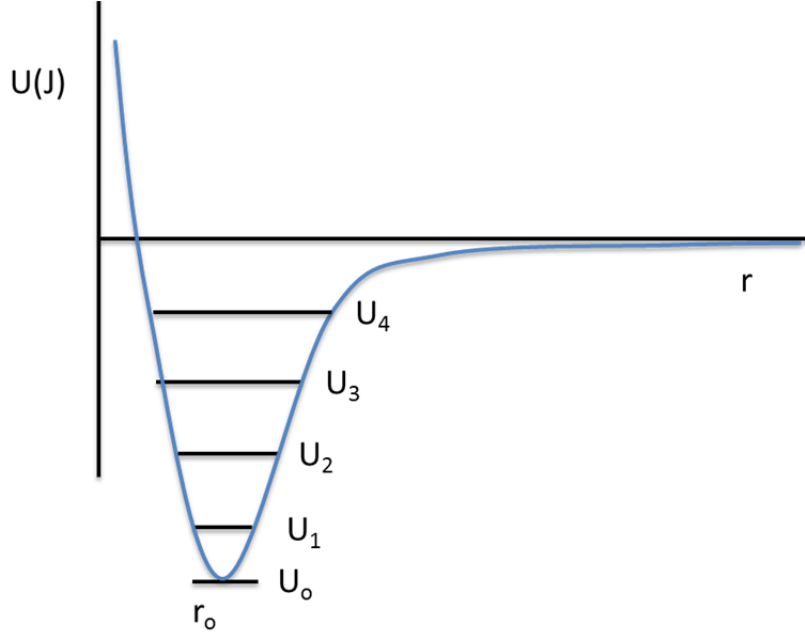


Figure 9. Generic Morse curve

In Figure 9, the horizontal axis; r , represents the interatomic distance between two atoms in a molecule, while the vertical axis; U , represents the free energy of the system. This simple yet effective curve shows that as r approaches infinity, the forces between two atoms goes to zero. As the atoms move closer together, they are attracted to a greater and greater extent until they are so close to one another that the nuclear forces generate a very strong repulsion. This results in the interatomic distances being such that they minimize the free energy of the system and at the lowest energy state the distance is fixed at r_0 . If energy is added to the molecule, it will no longer be static at the lowest energy state, but it will begin to vibrate at a higher energy state. However, this vibration must occur at discrete vibrational energies and thus the amount of energy required to induce vibration is not a continuous function, rather a specific amount of energy (one quantum [26]) is required to boost the molecule to the next highest energy state and induce a different vibrational mode. The allowed energy levels were derived by Philip M. Morse to be a finite polynomial of the form [30]

$$E(n) = E_e + h\omega_0 \left(n + \frac{1}{2} \right) - h\omega_0 x \left(n + \frac{1}{2} \right)^2 \quad (1.11)$$

The derivation of (1.11) is not important to this discussion, rather it simply shows that there are discrete energy levels possible for a molecule and only those energy levels can be achieved as represented by U_0, U_1, U_2 , etc., in Figure 9.

The fact that the vibrational states of a molecule are quantized also means that the polarizability of a molecule is also quantized. This fact then must be taken into account in when calculating the Raman scattering intensity. Including both the Stokes, and Anti-Stokes scattering, the slightly simpler version of the Raman intensity equation is [26], [29]

$$I_R = KI_L \alpha^2 \omega_0^2 \quad (1.12)$$

where I_L is the laser intensity and K is a proportionality constant which includes the speed of light. In order to describe the quantized nature of the polarizability of a molecule, Heisenberg and Dirac derived a quantum mechanical description in the 1920s of the form [26], [28]

$$(\alpha_{\rho\sigma})_{GF} = k \sum_I \left(\frac{\langle F | \mu_\rho | I \rangle \langle I | \mu_\sigma | G \rangle}{\omega_{GI} - \omega_0 - i\Gamma_I} + \frac{\langle I | \mu_\rho | G \rangle \langle F | \mu_\sigma | I \rangle}{\omega_{IF} + \omega_0 - i\Gamma_I} \right) \quad (1.13)$$

At first glance this expression appears quite menacing, however with a little explanation and elemental analysis it can be simplified to a more manageable form. In order to follow Equation 1.13 it is important to first define the terms and the mathematical symbols used as they are not the most common symbols seen in mathematics.

$\alpha \equiv$ molecular polarizability
 $\rho \equiv$ incident polarization direction
 $\sigma \equiv$ scattered polarization direction
 $\Sigma \equiv$ sum of all vibronic states of the molecule
 $G \equiv$ ground vibronic state
 $I \equiv$ excited vibronic state
 $F \equiv$ final vibronic state
 $\mu_{\sigma,\rho} \equiv$ dipole operator
 $\omega \equiv$ frequency of radiation
 $i\Gamma \equiv$ frequency term relating the lifetime of an excited electron state
 $\langle F|\mu|G \rangle \equiv$ Dirac bra-ket notation for describing quantum states

In order to quickly simplify Equation 1.13, first look at the denominators of the two terms inside the summation. The first denominator will always be smaller than the second due to the fact that ω_{GI} and ω_0 are subtracted vice added and therefore the second term will always be much less than the first term and can be neglected. This can also be thought of in the context that in the first expression the molecule begins in the ground state, is excited, and then drops to some other final state (i.e., Stokes scattering), whereas in the second expression the molecule begins in the excited state and ends in the ground state (i.e., Anti-Stokes scattering), which is not nearly as likely.

Now, just looking at the first term, the numerator mixes the energies of the excited vibrational state and the final vibrational state $\langle F|\mu_\rho|I \rangle$ which when summed over all states describes the scattering process. It also mixes the energies of the ground vibrational state and the excited vibrational state $\langle I|\mu_\sigma|G \rangle$, which when summed over all states describes the excitation process [26].

The base Raman scattering equation described above is used to mathematically describe the effect of resonance Raman scattering. Using the assumptions above, Equation 1.13 can be simplified to:

$$(\alpha_{\rho\sigma})_{GF} = \sum_I \left(\frac{\langle F|\mu_\rho|I \rangle \langle I|\mu_\sigma|G \rangle}{\omega_{GI} - \omega_0 - i\Gamma_I} \right) \quad (1.14)$$

which neglects the second term of the equation and the fitting constant k . Furthermore, because the electronic transitions in a excited molecule occur on a much shorter timescale (10^{-13} seconds) [26] than the vibrational transitions (10^{-9} seconds) [26], the Born – Oppenheimer approximation can be utilized to separate the total wave functions in the numerator of Equation 1.14 into an electronic part and a vibrational part. Raman spectroscopy is then concerned with the vibrational part of the polarizability tensor which reduces to [28]

$$(\alpha_{\rho\sigma})_{GF} = \sum_{\varepsilon'} \left(\frac{\langle \nu_F | \nu_{\varepsilon'} \rangle \langle \nu_{\varepsilon'} | \nu_I \rangle}{\omega_{GI} - \omega_0 - i\Gamma_{\varepsilon' \nu_{\varepsilon'}}} \right) \quad (1.15)$$

Although Equation 1.15 is still cumbersome, it provides some insight into the physics behind quantum Raman scattering. Essentially, Equation 1.15 shows mathematically how to calculate the polarizability of a molecule from its quantized vibrational states which then affects the received Raman intensity via Equation 1.12 [28].

C. RAMAN SPECTROSCOPY

1. Signal Intensity

In modern Raman spectroscopy, a monochromatic laser of intensity I_0 is used as an excitation source on a given piece of material. The intensity of the Raman scattered radiation I_R (described in detail in section B) can also be expressed as [29]

$$I_R \propto \nu^4 I_0 N \left(\frac{\partial \alpha}{\partial Q} \right)^2 \quad (1.16)$$

where N is the number of scattering molecules in a given state, ν is the frequency of the exciting laser, α is the polarizability of the molecules, and Q is the vibrational amplitude. Inspection of Equation 1.16 shows that the resultant intensity of the Raman scattered radiation which is measured by a sensor in Raman spectroscopy is dependent on several variables. First, the dependence on N clearly shows as the sample size increases so does the resultant intensity. Second, is the dependence on I_0 meaning that the more laser power that is used the larger the resultant signal intensity. However, increasing laser power can

also have the undesired effect of causing thermal heating of the sample from the incident laser. Third, there is the dependence on the choice of laser wavelength. As it appears from Equation 1.16, a higher frequency laser will give a larger signal, however this effect is more complicated. As was discussed in section B, choosing the appropriate laser wavelength is very important because it has a profound effect on the polarizability of a molecule which is also a major term in the signal intensity. Lastly, only molecular vibrations that cause a change in the polarizability of a molecule are Raman active (see section B.2.a), that is to say $\left(\frac{\partial\alpha}{\partial Q}\right) \neq 0$ [29].

2. Raman Spectrometer Functional Description

The general concept of how a Raman spectrometer works is fairly simple. A laser of a specific wavelength is generated and then passed through neutral density and spatial filters. The laser is then reflected off of several carefully aligned mirrors into a microscope objective. The microscope focuses the laser to the desired magnification level (selected by the operator) onto the sample. As the incident laser interacts with the sample, Rayleigh and Raman scattered light are emitted from the sample and travel back through the microscope objective and into a notch filter which removes all light that is at the incident laser wavelength (i.e., removes Rayleigh scattering). The remaining Raman scattered light must then be decomposed into its composite wavelengths in order to obtain useable Raman spectra. This is accomplished by the use of a diffraction grating which essentially splits the remaining light into its constituent wavelengths. The diffraction grating used is specific to the wavelength of the incident laser. The split light is then focused onto a silicon charge-couple device detector which measures the intensity and wavelength of the resultant scattered light. Figure 10 from the Renishaw Corporation shows a schematic representation of this light path.

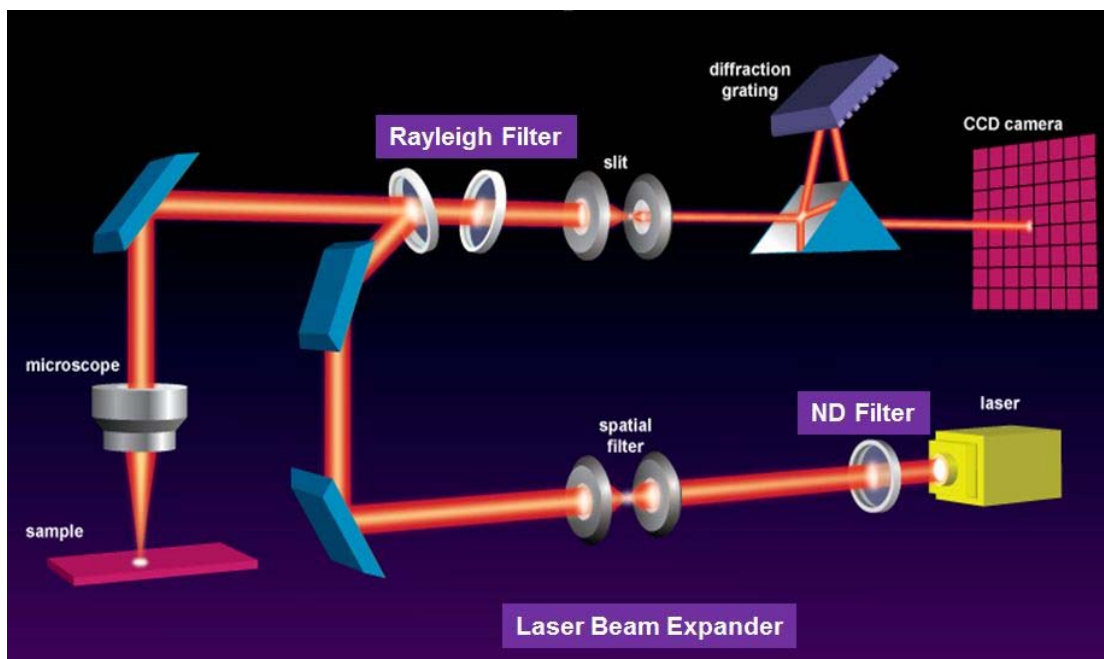


Figure 10. Schematic representation of the Raman Spectrometer light path (Renishaw).

Once the data is collected by the detector, it is sent to a computer terminal which displays the Raman data on a two-dimensional plot where the horizontal axis is the Raman shift (wavelength or wave number) and the vertical axis is the intensity counts. The operating terminal allows the user to select the incident laser power. The software also has the operator select the magnification level (used only for visual scale bar on computer—actual magnification level is selected by choosing the appropriate lens just as in a traditional optical microscope), incident laser wavelength (selected in computer for processing purposes—actual wavelength is set by the operator based on physical laser used), and the grating used (selected in computer for alignment purposes—must match the incident laser used and equipment automatically aligns grating). The resultant spectra can then be analyzed in the computer software to obtain information about the molecular structure of the sample being analyzed.

The Raman spectrometer used in this study was the Renishaw inVia Raman Spectrometer. Figures 11 and 12 are pictures of the Renishaw Raman Spectrometer as it is set up in the NPS nanomaterials laboratory. Figure 11 shows the overall system setup, and Figure 12 shows the internal optics of the system and the laser light path.

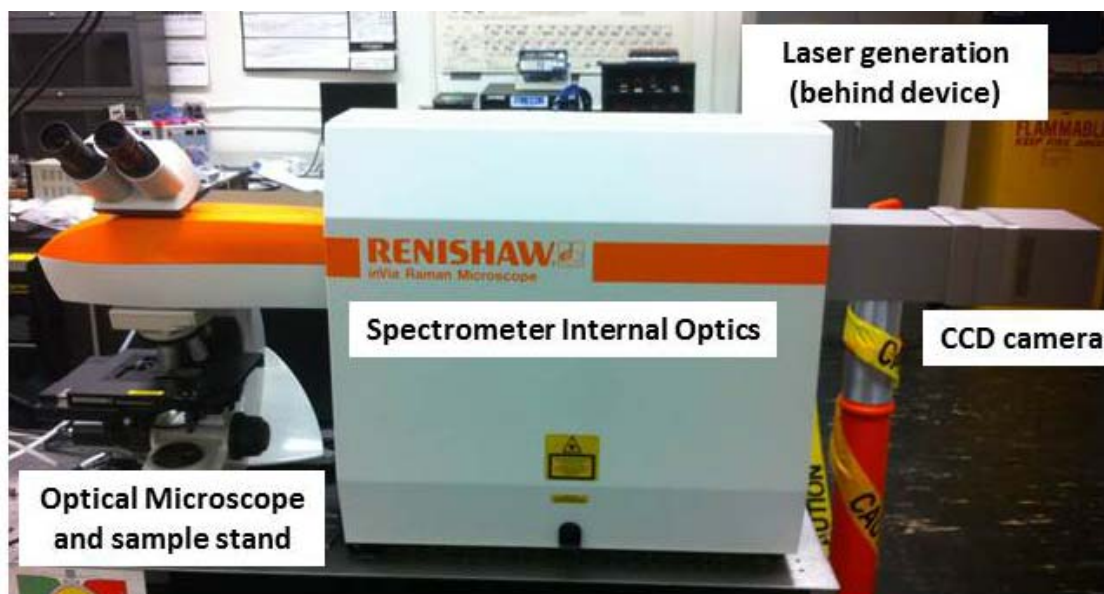


Figure 11. Renishaw inVia Raman Spectrometer setup in NPS nanomaterials laboratory.

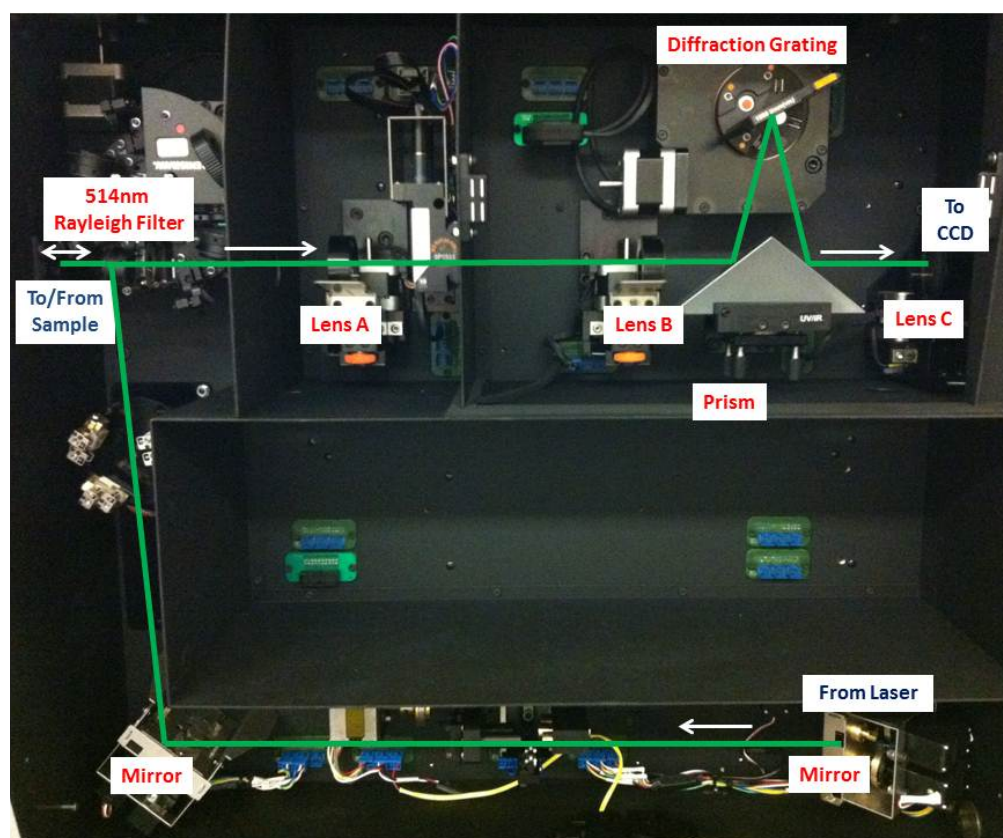


Figure 12. Renishaw inVia Raman Spectrometer internal optics.

Note that the Lenses A, B, and C along with the diffraction grating need to be changed by the operator as appropriate for the specific incident laser wavelength used. In the NPS laboratory, the available laser wavelengths are 325 nm (Helium-Cadmium), 514 nm (Argon-Ion), 633 nm (Helium-Neon), and 785 nm (Diode).

3. Uses and Advantages of Raman Spectroscopy

Raman spectroscopy has become a widely used tool for characterizing various materials. Raman is a non-destructive technique that requires very little sample preparation and is relatively inexpensive. There are very few restrictions on what type of sample can be measured. Experiments can be conducted on samples that are openly exposed to the atmosphere or samples that are contained in a controlled environment as Raman can be accomplished through a containment window.

In addition to Raman spectroscopy being relatively easy to perform on a variety of materials and under different conditions, it is also a very powerful characterization technique that gives information as to the bonding environment in a sample of material. This information can be used to determine material composition (via characteristic Raman signatures), identify stress/strain state in a sample (via changes in the position of Raman peaks), and determine the crystalline quality of a sample (via width of Raman peaks).

Most notably, Raman spectroscopy can characterize the formation/decomposition of a sample by performing the study *in situ* with the transformation process. In this *in situ* study, Raman spectroscopy is performed utilizing a heating stage (sample holder with programmable temperature control and controlled environment) and producing graphene from thermal exfoliation of a GO/urea mixture while measuring the Raman spectra throughout the heating/formation process.

4. Resonant Raman Spectroscopy

Resonant Raman (RR) scattering is an enhancement technique for Raman spectroscopy that utilizes the discrete nature of a molecules allowable energy states in order to boost the signal to noise ratio without necessarily increasing laser power which

can have undesirable effects or increasing detector sensitivity which can be extremely expensive if at all possible. However, operating in RR also leads to new source of noise that is not observed in non-resonant Raman, namely fluorescence/luminescence [28].

RR scattering and luminescence occur simultaneously however they originate from two different physical phenomena. RR occurs as a direct two photon process where a molecule absorbs and incoming photon increasing its energy state, then immediately releases a photon of a slightly different energy decreasing its energy state to some other state. In contrast, luminescence is a two-step process caused by the radiant decay of excess molecules excited by the incident radiation to an intermediate state. When the excitation source is removed, RR will stop abruptly while luminescence will follow an exponential decay as the excess excited molecules decay [31]. Since the cross-section for luminescence is approximately six orders of magnitude larger than the cross-section for RR, if RR scattering and luminescence occur from the same excited energy state then the RR spectra can be completely masked by that of luminescence. However, this issue can be avoided by two methods. First, luminescence typically occurs at the closest energy state to the ground state, whereas RR can occur at higher energy states depending on the excitation wavelength meaning that the resultant energy release from RR and luminescence are different and easily distinguishable in the spectra. Second, since the process for luminescence is more involved it takes significantly more time to occur (typically on the order of 10^{-9} s) vice the direct two-photon process of RR (typically on the order of 10^{-15} s), using an ultrafast shutter can enable observation of only the RR signal [28].

As alluded to previously, the operator's choice of the excitation laser wavelength is extremely important to achieve a high quality signal to noise ratio in the Raman spectra. As with any characterization technique, scientific experimentation with different configurations and settings is the best method to determine the optimal settings as was done in this study which will be discussed at the end of this chapter. In order to determine a good starting point however, it is important to understand the RR enhancement. Figure 13 highlights the enhancement achieved by utilizing the RR phenomenon. Figure 13 illustrates that when the excitation laser wavelength is chosen appropriately, molecules

can jump to a much higher real energy state vice a virtual energy state in standard Raman spectroscopy. This also means that stronger Raman signals are generated and the signal to noise ratio is greatly increased. This occurs when the excitation laser energy is such that it corresponds to the band gap between energy states allowing the molecules in the sample to absorb this energy and jump to an energy state that is several orders of magnitude higher than it would otherwise.

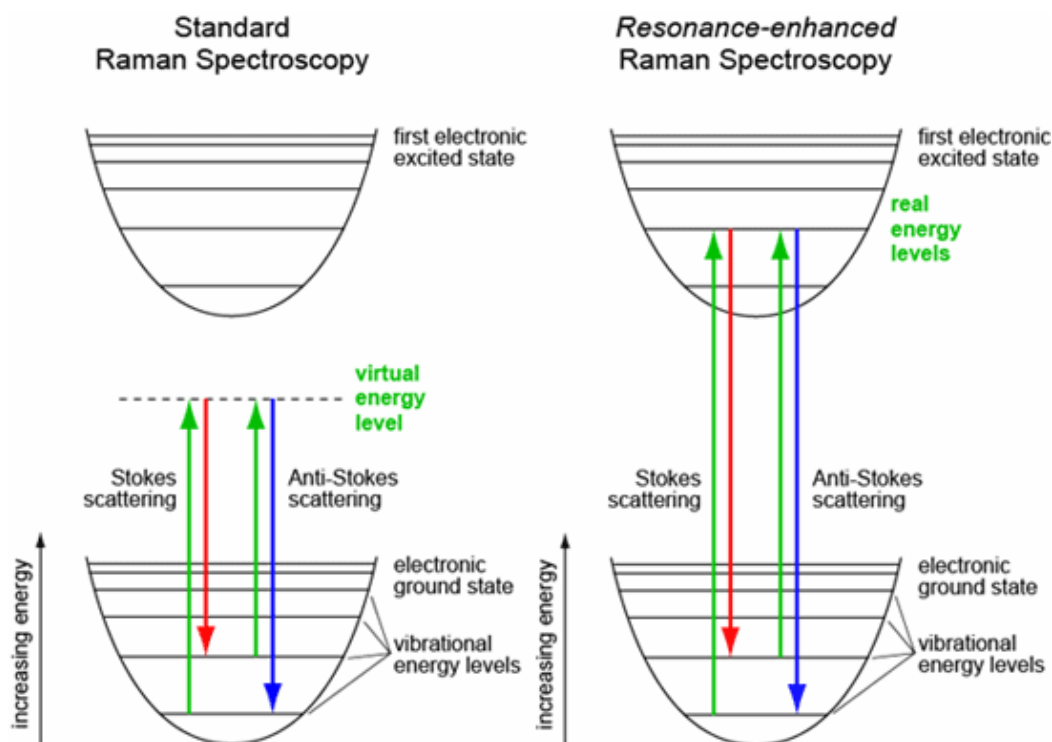


Figure 13. Comparison between Standard Raman Spectroscopy and RR Spectroscopy for both Stokes and Anti-Stokes scattering (From [32]).

Even though the ideal wavelength is one that corresponds to the band gap between two energy states of the molecule, the vast majority of Raman experimentation in literature has been done using visible, infrared, or near-infrared excitation lasers due to the relative abundance and low cost in the current market. That being said, sometimes these wavelengths are not the optimal choices because; especially in the case of longer wavelength lasers, they do not poses enough energy to cover the band gap of the material

being studied. Table 1 is a list of available lasers in the NPS Nanomaterials Laboratory with their corresponding wavelength and energies.

Table 1. NPS Raman Spectrometer lasers

Laser	Wavelength (nm)	Energy (eV)
Helium-Cadmium	325	3.825
Argon-Ion	514	2.419
Helium-Neon	633	1.964
Diode	785	1.584

The energy associated with the infrared laser in the NPS laboratory is down to 1.584 eV, which is lower than the band gap in most engineering materials of interest and therefore Raman experimentation done with this long wavelength laser will result in a poor signal to noise ratio without a RR enhancement for most materials. Instead the laser wavelength should be chosen such that the energy falls within the material of interest's electronic structure.

Fortunately for this study, there are several different laser wavelengths to choose from in the NPS laboratory, but also graphene is a “zero-gap semiconductor” meaning that even very low energy lasers such as the infrared laser should allow for the RR enhancement. On the other hand, if the study was on a substance such as diamond that has a very large band gap, the shortest wavelength ultraviolet laser would be more appropriate. In this study two different lasers were tested on graphene samples in order to determine the optimal laser wavelength for the *in situ* study of graphene formation by thermal exfoliation. As stated earlier, pure graphene has no band gap and in fact it has been found that even nitrogen doped graphene (similar to the GO/urea graphene used in this study) has a band gap of only 0.98 eV [33] so it would be logical to start with the longest wavelength laser for the study. Unfortunately, however, due to the nature of the study being done *in situ* while heating a GO/urea sample, the thermal radiation, which is

in the near infrared spectral range, would overshadow the weaker Raman signal. Therefore, the 633 nm and the 514 nm lasers were tested on several different graphene samples at room temperature and while heating up to 900 °C in an inert argon atmosphere.

First, the 633 nm laser showed quality spectra for several graphene samples at room temperature. However, when heating the graphene samples the interference with thermal radiation emitted from the sample become noticeable at approximately 450 °C. As the temperature of the samples was further increased, the thermal background dominated the spectra and the characteristic Raman features of graphene were no longer distinguishable. The 514 nm laser showed significant improvement in background reduction over the 633 nm laser, particularly at higher temperatures. The 514 nm laser allowed for *in situ* Raman studies at temperatures as high as 750 °C and was therefore chosen to be the laser used for this study. However, even with the 514 nm laser additional data processing, such as background subtractions, is required at higher temperatures. The reason behind not using the ultraviolet laser is simply that the energy is too high for graphene samples and would very quickly result in localized heating of the sample from the laser. In this study, this could result in essentially thermally exfoliating the GO/urea mixture rapidly with the laser vice in a controlled manor with the temperature program and defeat the purpose of the *in situ* study.

D. THESIS OBJECTIVES

In this study, *in situ* Raman spectroscopy is employed to monitor the transformation of a GO/urea mixture into nitrogen doped graphene via thermal exfoliation of the GO/urea. Specifically, this study aims to:

- Characterize the graphene formation process by identifying the critical chemical reaction steps in the temperature profile.
- Show conclusively that nitrogen is inserted into the graphene crystal lattice by the use of urea during thermal exfoliation of GO.
- Utilize Raman spectroscopy to characterize the nitrogen doping level of graphene.

- Determine if the nitrogen inserted into the graphene during formation is stable by conducting subsequent heating and cooling study of the produced graphene.
- Utilize complimentary techniques (XRD, TGA, DSC, and mass spectroscopy) to support Raman data

II. EXPERIMENTAL

A. MATERIALS

The graphene for this study was produced via a thermal exfoliation technique of pure GO and a GO/urea mixture. This technique was developed by NPS professor Claudia C. Luhrs [8]. The GO used for the production was also produced by professor Luhrs' research group at NPS.

1. Graphite Oxide

The graphite oxide (GO) was produced by LT Ashley Maxson and LT Ryan Palaniuk from Prof. Claudia C. Luhrs' research group. The graphite used was a synthetic graphite powder (less than 20 μm particle size) from Sigma Aldrich. The basic procedure for the production of GO from graphite powder is a slight variation of the procedure developed by William S. Hummers, Jr., in 1958 [34]. For further details on the synthesis, the reader is referred to the theses of LT Ashley Maxson and LT Ryan Palaniuk.

For this experiment, the GO was allowed to dry for three days in the beaker and then the beaker was placed under vacuum for an additional two days in order to remove it from exposure to water vapor and all atmospheric gases. The GO was then placed into a glove box under an Ar atmosphere and mechanically ground into a powder using a hand mortar. The GO as well as the GO/urea mixture samples were then stored inside the glove box under Ar until used for experimentation.

2. Urea

The urea used for this study is commercially available urea obtained from the Sigma Aldrich Corporation, lot number 120M0127V. The urea was received in small pellets from the manufacturer and then hand ground in a mortar to form a powder. Two hundred mg of urea powder was then mixed with 200 mg of the ground GO powder attempting to produce a homogeneous mixture of GO/urea powder in a 1:1 weight ratio.

3. Production of Graphene via Thermal Exfoliation

Thermal exfoliation of the GO/urea mixture was done *in situ* with Raman spectroscopy, while a corresponding TGA/DSC/Mass spectroscopy experiment was completed on both pure GO as well as the GO/urea mixture. Several experiments were completed with a different batch of GO and GO/urea in order to determine the desired temperature profile. Figure 14 shows the temperature profile used for this study for both the Raman spectroscopy and the TGA/DSC analysis.

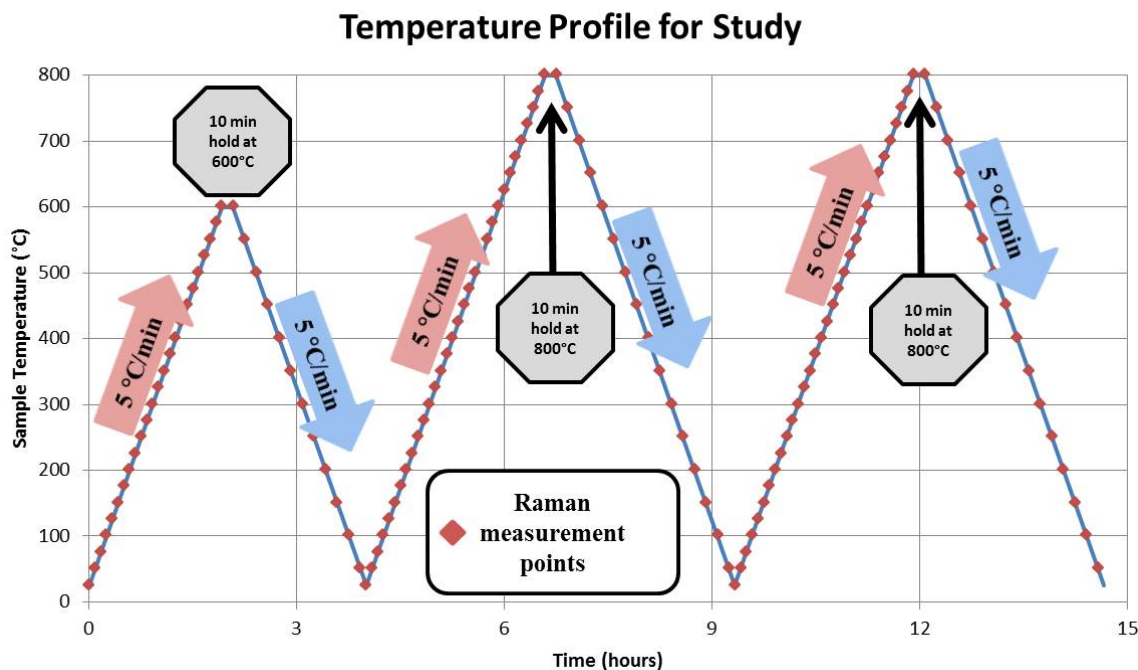


Figure 14. Temperature Profile used for study.

The thermal decomposition of urea begins at approximately 150 °C with melting and a vaporization process that results in the evolution of ammonia and cyanic acid [8]. At approximately 200 °C the cyanic acid and remnant urea begin to react producing biuret and cyanuric acid. As the temperature continues to rise, the biuret decomposes to produce some additional cyanic acid and ammonia which then reacts with the cyanuric acid forming ammelide. By approximately 250 °C, the biuret is mostly depleted and the

cyanuric acid is at its peak concentration [35]. At 350 °C, the cyanuric acid has nearly completely decomposed and all remnants of urea and biuret have been lost [35]. Then by 435 °C the ammelide also decomposes.

The decomposition process described above is the reasoning behind the initial heating/cooling cycle of Figure 14 going to 600 °C. This ensures that the sample has been completely exfoliated and all remnant urea and urea decomposition products have been eliminated leaving only graphene. The Raman spectra were recorded every 25 °C in order to capture the transformation processes as they occur during sample heating. The second heating/cooling cycle to 800 °C in Figure 14 is to study higher temperature effects on the resultant graphene, specifically investigating the absorption of nitrogen into the graphene matrix. Finally, the last heating/cooling cycle to 800 °C was completed in order to confirm and duplicate the results from the higher temperature study. These three temperature cycles were performed as one temperature profile for the TGA/DSC experimentation, and on consecutive days for the Raman experimentation. Due to the fact that each ramp takes seven or more hours to complete when doing the Raman spectroscopy, each ramp was completed in one day with the following ramps completed on subsequent day pausing at room temperature overnight. During the entire experiment, the sample was left in the heating stage with a constant flow of Ar.

B. METHODS AND CHARACTERIZATION

1. Raman Spectroscopy

Raman spectra were obtained using an inVia Confocal Raman Microspectrometer (Renishaw, UK) utilizing a 514 nm argon-ion laser as discussed previously. The setup included an Olympus SLMPlan N 20x microscope objective, and an 1800 l/mm (lines per millimeter) visible light diffraction grating. Prior to each experiment the spectrometer was calibrated using a silicon wafer mounted onto a glass slide to ensure that the Raman peak is at 520 cm^{-1} . All *in situ* Raman experiments were conducted using a programmable water-cooled Linkam TS1500 high temperature stage. The samples were placed onto a quartz slide within the stage for measurement. A constant flow of argon through the stage was used as a controlled environment for the

experiments, while the exact flow rate used will be discussed later. The spectrometer's experimental parameters (discussed later) were controlled using Renishaw's Wire 2.0 computer software. This software was also used for all data analysis and curve fitting. Figure 15 is a picture of the experimental setup with the TS1500 high temperature stage placed under the spectrometer's microscope objective with the argon and cooling water connections.

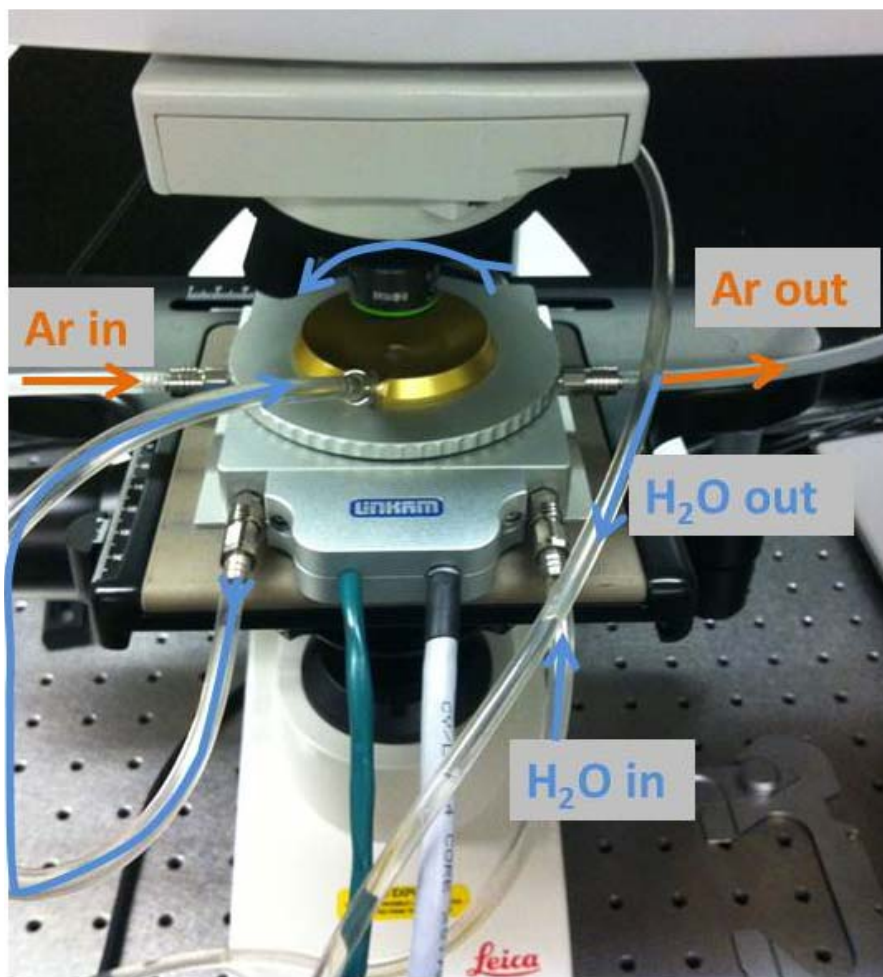


Figure 15. Experimental setup used for all Raman experimentation. The TS1500 high temperature stage is mounted under the spectrometer's microscope objective with the argon and cooling water connected.

a. Raman Experimental Parameters

The choices of excitation wavelength and temperature profile for this study were described in detail in sections I.C.4 and II.A.3, respectively. As stated previously, experimentation was completed on several different graphene, GO, and GO/urea samples in order to determine the best experimental parameters to use for this Raman study. The samples analyzed in these preliminary experiments were produced from a different batch of GO using the same procedure as described in section 2.A.1, with the exception that they were not stored under argon after production. Table 2 summarizes the parameters used for this study with a detailed explanation of each of these parameters following in section 2.B.1.b.

Table 2. Raman experimental parameters.

<i>Parameter</i>	<i>Value</i>	<i>Unit</i>
Laser Wavelength	514	nm
Laser Power	10	% of maximum
Accumulations	10	Total accumulations
Time of each accumulation	20	Seconds
Microscope Objective	20	X magnification
Raman Spectra center	1,500	cm ⁻¹
Argon flow rate	20	mL/min

b. Determination of Experimental Parameters

The series of preliminary experiments included several room temperature Raman measurements on graphene samples produced from thermal exfoliation of GO/urea mixtures of different ratios, two *in situ* Raman experiments heating graphene

produced from pure GO (first heating from room temperature to 650 °C and second heating from room temperature to 800 °C), four *in situ* Raman experiments heating a GO/urea 1:1 mixture (first heating from room temperature to 385 °C then three heating from room temperature to 450 °C), and finally one *in situ* Raman experiment heating graphene produced from thermal exfoliation of a GO/urea 1:1 mixture from room temperature to 900 °C. This series of experiments was completed while varying the parameters listed in Table 2. The exact parameters and spectra obtained from each experiment is not of concern here, rather what is important is the lessons learned from these experiments which led to the decision on the parameters in Table 2.

First, the laser power, number of accumulations, and time of each sweep all have similar effects. Increasing laser power will obviously increase the signal to noise ratio, however it can result in localized sample heating from laser input and therefore deviate from the controlled temperature profile of interest and have a local temperature that is unknown. Increasing the total number of accumulations can also help to obtain a better signal to noise ratio because the software simply sums the spectra obtained from each accumulation to obtain the overall spectra. Therefore, peaks that are just slightly above background noise in the first accumulation will grow faster than background as the spectra is summed with additional accumulations resulting in a higher background but also larger peaks as the accumulations are increased. On the down side, increasing the accumulations is essentially taking additional Raman measurements which requires more time. The heating of the sample is suspended during each Raman measurement, so the longer each measurement takes the more the heat-up rate deviates from the nominal 5 °/min heat-up/cool-down rate. Lastly, increasing the time of each accumulation will also result in a better signal to noise ratio in the same way that increasing the power of the laser increases the signal to noise ratio. However, in the case of accumulation time, the detrimental effects of localized sample heating as well as increased time of measurement are both present. The values of these three parameters were chosen for this study because in the preliminary experimentation these values yielded acceptable spectra

in terms of signal to noise ratio while both maintaining a relatively short measurement time and showing no signs of localized sample heating (characteristic down-shift in Raman peaks).

The selection of the Olympus SLMPlan N 20x microscope objective was based on two equally important criteria. First, it was noticed in preliminary experimentation that the GO/urea mixtures were not completely homogeneous mixtures. This was observed both visually through the optical microscope and by obtaining slightly different Raman spectra on different parts of the samples while using a 50x objective. This non-homogeneity was addressed by attempting to achieve homogeneous mixing of the GO and urea during preparation of the mixture and also by using a lower magnification objective and thereby obtaining Raman spectra on a larger portion of sample. Second, the Raman spectra using the 50x objective were taken outside of the Linkam stage and due to dimensional constraints even the 50x “long focus” objective cannot focus into the stage and only the Olympus SLMPlan N 20x microscope (“long focus”) objective works for this application.

The Raman spectra center was chosen because in a static scan this allows from the spectrometer to measure Raman shifts from 550 cm^{-1} to 2318 cm^{-1} , where the nominal first order peaks of interest for graphene have centers located at 1360 cm^{-1} (D-band) and 1600 cm^{-1} (G-band). As part of the preliminary experimentation, extended Raman measurements were taken on several graphene samples measuring the Raman shift from 900 cm^{-1} to 3500 cm^{-1} , which showed both the first order and the second order Raman peaks which occur between 2680 cm^{-1} and 3200 cm^{-1} . However, extended Raman measurements involve the spectrometer mechanically moving the diffraction grating which extends the time required for the measurement by a factor of 10. Therefore, static Raman measurements were conducted centered at 1500 cm^{-1} .

Last was the selection for the argon flow rate through the stage. This was determined from the results of the three preliminary *in situ* Raman experiments heating a GO/urea 1:1 mixture three heating from room temperature to $450\text{ }^{\circ}\text{C}$. After completion of these experiments, all of the Raman spectra obtained for each experiment were processed

and curve fit using the Renishaw Wire 3.2 software as shown in Figure 16. There are two main Raman peaks associated with graphene that each are composed of two separated peaks (D1, D2, G1, and G2).

These experiments were conducted using different flow rates of argon through the stage. The ratio of intensities of the D1 and G1 peaks from the curve fitting data for each experiment are plotted in Figure 17. It was determined that the different flow rates have a profound effect on the thermal exfoliation process due to the fact that the first step in the decomposition of urea is to produce gaseous ammonia and cyanic acid which is removed quickly under a high argon gas flow.

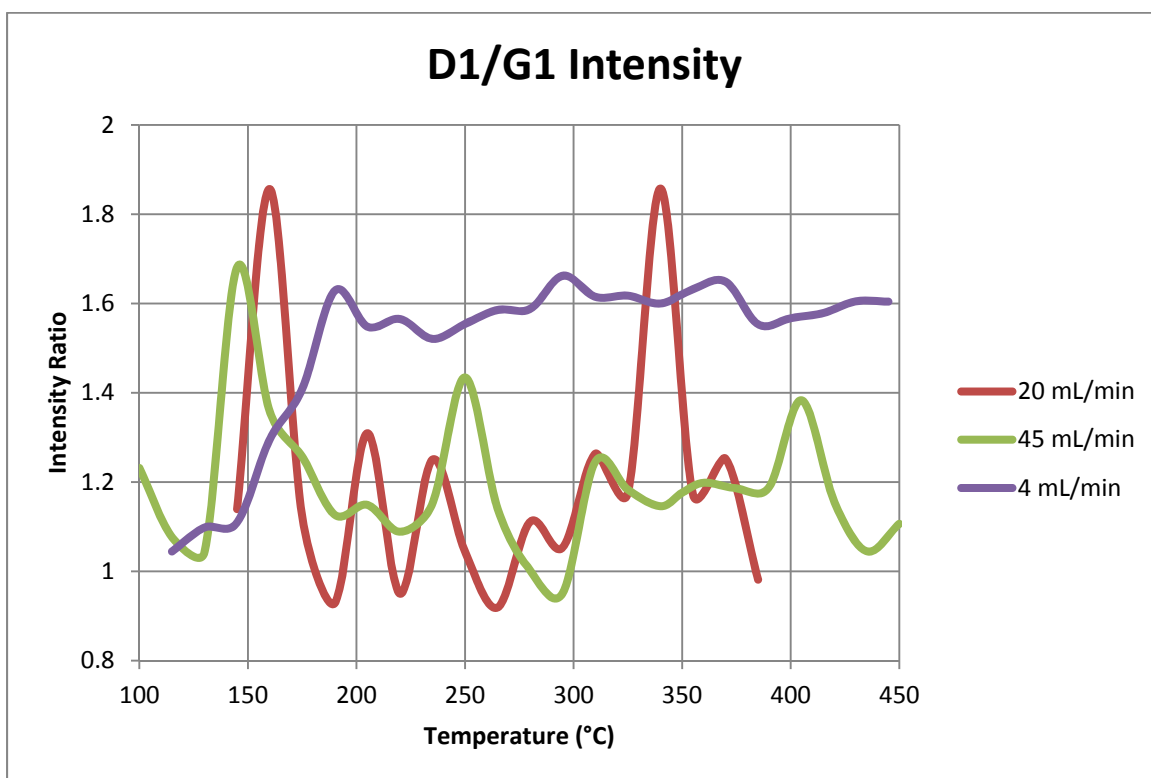


Figure 16. D1/G1 Intensity ratio vs. temperature for GO/urea 1:1 *in situ* Raman preliminary experiments varying argon gas flow rate.

Although there is a significant amount of data scatter, it can be seen in Figure 16 that a higher gas flow rate results in the reaction occurring at slightly lower temperature and a fast drop off as the ammonia and cyanic acid are removed quickly during the first stage of urea decomposition. In the case of the 4 mL/min flow rate, the

extremely slow removal of urea decomposition byproducts creates a very thick “fog” inside the stage and makes laser focusing extremely difficult. It also causes a significant amount of laser intensity to be lost due to scattering off the “fog” and results in poor spectra. This “fog” problem is essentially eliminated when using the higher argon flow rate of 45 mL/min; however the extremely rapid removal of cyanic acid and ammonia changes the dynamics of the urea decomposition and thermal expansion of GO. The 20 mL/min flow rate was chosen in order to mitigate as much as possible both of these effects while still ensuring that the sample is studied under a controlled atmosphere.

2. Thermal Gravimetric Analysis, Differential Scanning Calorimetry, and Mass spectroscopy

The thermal gravimetric analysis (TGA) and differential scanning calorimetry (DSC) were conducted using the NETZSCH STA 449 F3 Jupiter simultaneous thermal analysis machine (Figures 17 and 19). Additionally, the evolved gases from the samples were analysed by coupling the TGA/DSC with the NETZSCH TA-QMS 403C Aëolos quadruple mass spectrometer (QMS) (Figures 18 and 19).

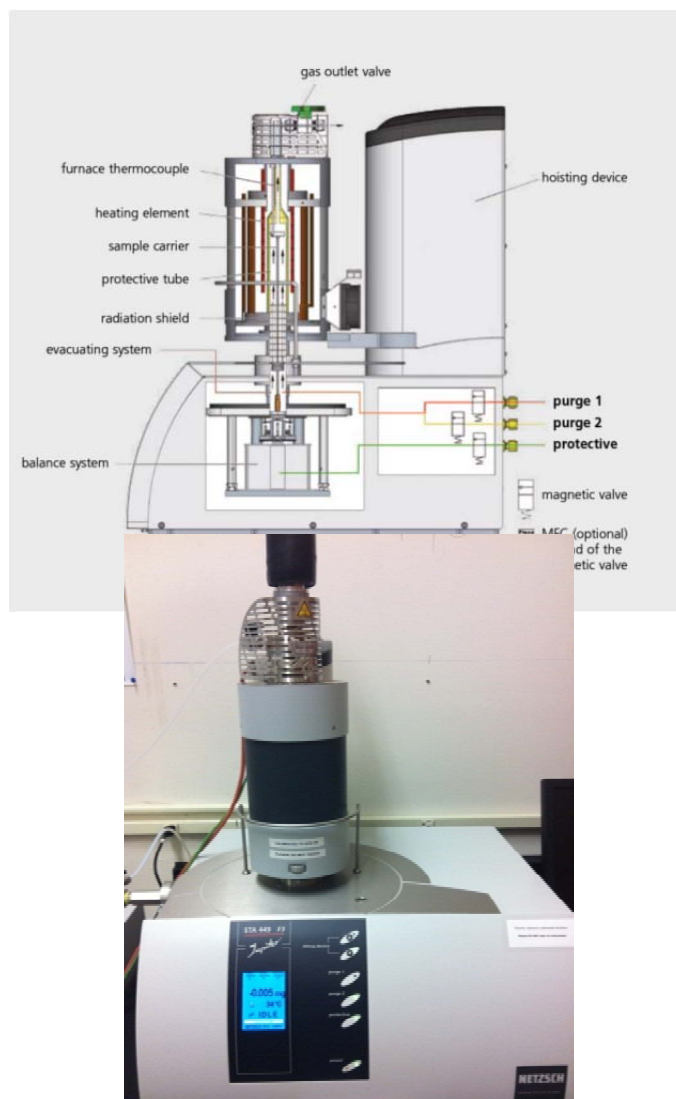


Figure 17. Diagram of NETZSCH STA449 F3 Jupiter (left) (NETZSCH), picture of setup in NPS laboratory (right).



Figure 18. Diagram of the TA-QMS 403 Aëolos (left) (NETZSCH), picture of setup in NPS laboratory (right).

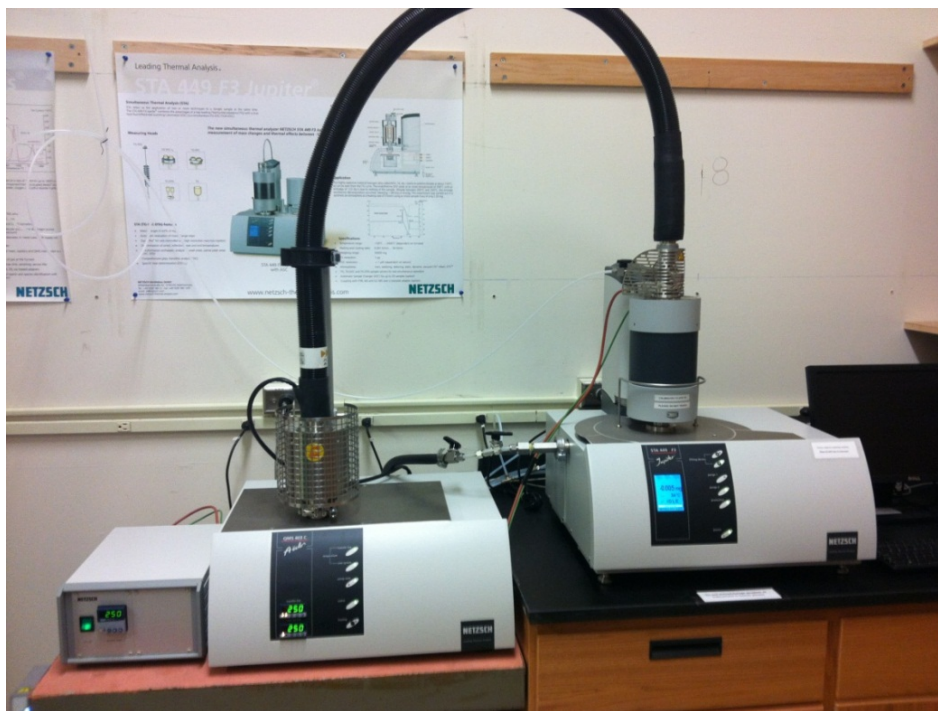


Figure 19. Picture of the TGA/DSC and mass spectrometer coupled setup in NPS laboratory.

In order to maintain the same parameters as used for the Raman experimentation, the following parameters were used for the TGA/DSC experiments.

Table 3. TGA/DSC experimental parameters.

<i>Parameter</i>	<i>GO/urea 1:1 mixture</i>	<i>Pure GO</i>
Heating/Cooling rate	5 °C/min	5 °C/min
Protective gas flow	20 mL/min Ar	20 mL/min Ar
Purge gas flow	20 mL/min Ar	20 mL/min Ar
Sample weight	4.5 mg	4.2 mg

The temperature profile for the TGA/DSC experiments was the same as shown in Figure 14; however, the measurement is continuous with heating/cooling vice pausing to measure as is the case with Raman spectroscopy. A very small amount of sample was used because preliminary TGA/DSC experimentation revealed that the dramatic expansion of GO associated with thermal exfoliation caused the sample to spill out of the TGA/DSC sample holder and onto the instruments thermal shields.

Upon completion of the Raman experiments, the data was truncated, the baseline subtracted, and the data was curve-fit using Renishaw Wire 3.2 software as stated previously. Upon completion of the TGA/DSC experiments, another run of the temperature program was performed under the same conditions as in Table 3, except with empty crucibles in order to obtain a correction curve. This correction curve was subtracted from the experimental data using the NETZSCH Proteus 6.0 software. Finally, all data from Raman, TGA/DSC, and mass spectroscopy was imported into the Origin 8.5 software for analysis and plotting.

3. X-ray Diffraction

X-ray diffraction (XRD) was performed on the pure GO produced by LT Ashley Maxson in order to confirm the quality of the GO. The XRD pattern was recorded using the Bragg-Brentano $\theta/2\theta$ geometry with a copper source. Figure 20 shows the setup of the XRD in the NPS laboratory.



Figure 20. Picture of the inside of NPS XRD (left),
picture of NPS XRD outside (right).

The XRD data was collected using the X'Pert Data Collector software and then analyzed and displayed using the X'Pert High Score software.

III. RESULTS AND DISCUSSION

A. THERMAL GRAVIMETRIC ANALYSIS

Thermal gravimetric analysis (TGA) and differential scanning calorimetry (DSC) experiments were conducted on both the GO/urea mixture and the pure GO using the temperature profile in Figure 14 and the parameters in Table 3. The data was then corrected and processed into each temperature cycle for graphical display (Figure 21).

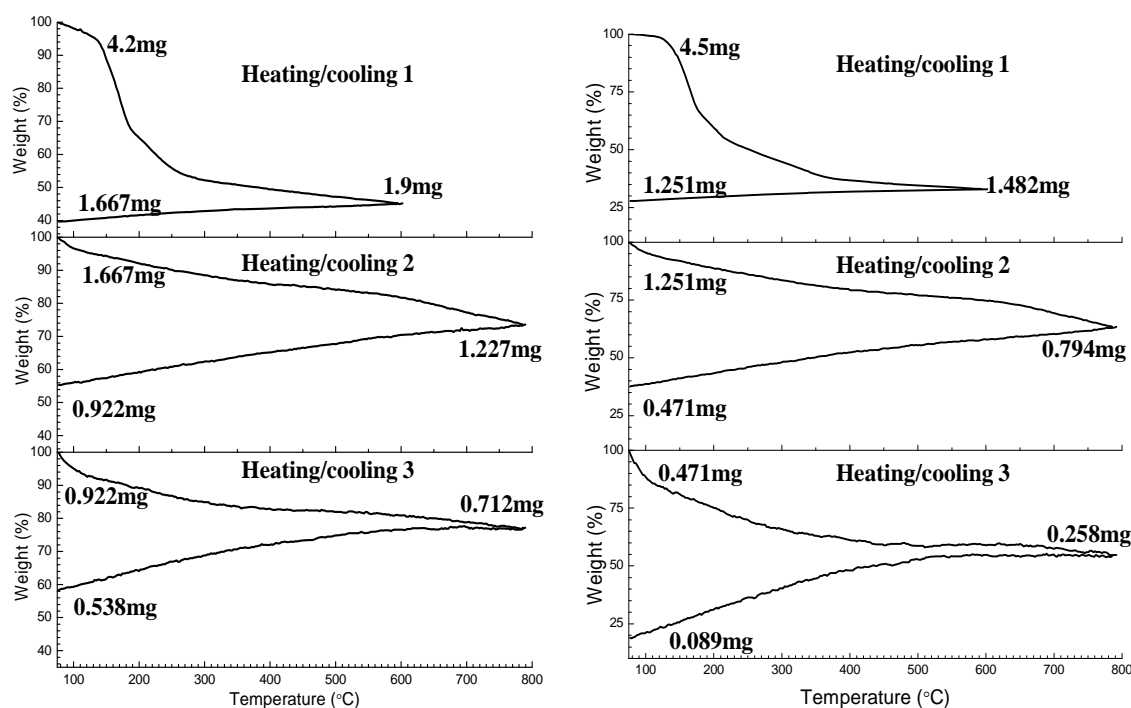


Figure 21. TGA of (left) pure GO and (right) GO/urea 1:1 mixture.

The TGA for pure GO showed a mass loss of 52% for the initial heat-up, followed by mass losses of 7, 11, 8, 5, and 4% for each subsequent temperature cycle, respectively (Figure 21). The large mass loss during the initial heat-up is attributed to the shedding of the oxide groups and some carbon during the thermal exfoliation of GO as CO and CO₂ are evolved. The small mass loss during each of the following temperature cycles is attributed to some oxidation of the sample over time and normal instrument drift [14]. The TGA for GO/urea showed a mass loss of 67% for the initial heat-up, followed by

mass losses of 6, 10, 8, 4, and 4% for each subsequent temperature cycle, respectively. The large mass loss during the initial heat-up is attributed to both a mass loss from the decomposition of urea and the shedding of the oxide groups as well as some carbon during the thermal exfoliation of GO just as was the case with pure GO. Also, just as with pure GO, the small mass loss during each of the following temperature cycles is attributed to some oxidation of the sample over time (which was observed visually in the Raman experimentation) as well as normal instrument drift [14].

Clearly from Figure 21, it is evident that all of the relevant mass loss measured by the TGA experiments occurs during the initial heat up phase. During the initial heat-up, the GO/urea has a higher mass loss due to the fact that urea is being lost along with the oxide groups of GO, and it also begins at a slightly lower temperature, which is shown in Figure 23 and will be discussed later.

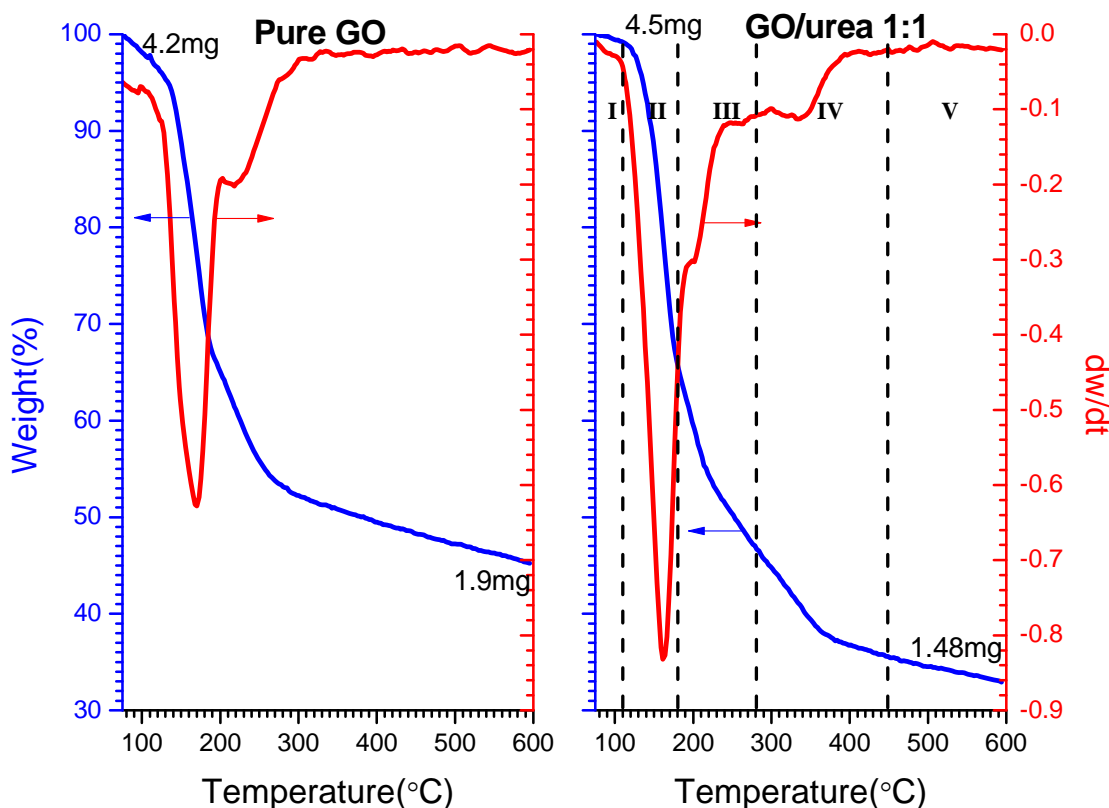


Figure 22. TGA and 1st derivative (dw/dT) of (left) pure GO and (right) GO/urea 1:1 mixture.

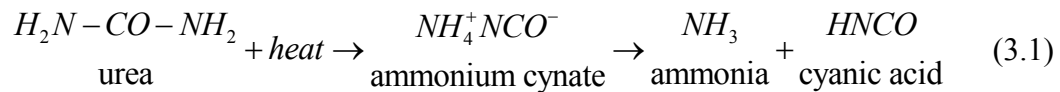
Figure 22 displays the TGA results from the initial heat-up of pure GO and GO/urea 1:1 mixture. The transformation process to graphene is quite different between these two samples, which is reflected in Figure 22.

1. Pure GO

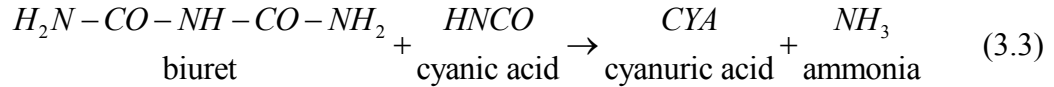
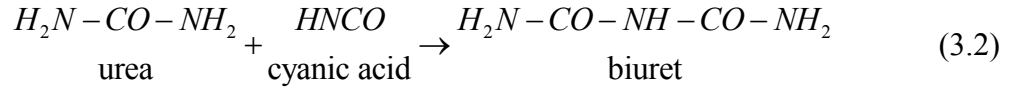
The transformation process of pure GO to graphene via thermal exfoliation occurs through several distinct steps. From 25–130 °C, there are no significant reactions occurring. Then from 130–190 °C, there is a major mass loss of GO due to shedding of the oxide groups yielding a large release of CO and CO₂ (which was also observed in mass spectroscopy). Of note is that this results in a large volume expansion of the GO sample which can lead to spraying of the sample out of the crucible and into the TGA instrument as occurring in both a previous experiment for this study as well as other studies [14]. A second mass loss occurs from 190–300 °C, which is presumed to be a slow removal of the remaining CO and CO₂ gases that were trapped inside the bulk material. Finally after 300 °C, there are no more significant changes as the graphene formed is stable throughout the remaining temperature cycles. The mass spectroscopy results in Figure 24 for pure GO, clearly show this large sudden release of CO and CO₂ as the thermal exfoliation process takes place.

2. GO/urea 1:1

The addition of urea to the GO naturally makes the thermal exfoliation process significantly more complicated, however less violent and more stable. In the case of a GO/urea mixture, the transformation process occurs over five vice four distinct regions, label as regions I, II, III, IV, and V in Figures 22 and 23. Region I; 25 °C to 110 °C, corresponds to the region just prior to the commencement of urea decomposition and just as in the case of pure GO, there is no significant reactions occurring. Then, in region II; 110 °C to 180 °C, the urea begins decomposing and vaporizing evolving ammonia and cyanic acid [35].



This is point where problems were encountered with “fog” in the first Raman experiment which will be discussed in detail later. In Figure 24, there is a local peak in ammonia evolution as the urea decomposes. If there was no GO in the sample, in region III; 180 °C to 280 °C, the cyanic acid produced from the initial urea decomposition would undergo several different reactions [8], [35].



However, the presence of GO and specifically the oxygen groups associated with the GO prohibit the reactions in equations 3.2 and 3.3. Instead, the cyanic acid preferentially reacts with the oxygen groups of the GO to produce more ammonia and some CO₂ [8] (these evolved gases were also observed in the mass spectroscopy). This use of the cyanic acid from urea decomposition as a reducing agent for the GO results in a very clean decomposition of urea and reduction of GO. As far as GO transformation to graphene this has several purposes. First, the stripping of the oxide groups is essential for the formation of graphene. Second, there is a sustained production of gas from the urea decomposition reactions which further helps to expand the GO and overcome the Van der Waals forces between layers resulting in graphene formation. Then in region IV; 280 °C to 450 °C, there is essentially no urea remaining and all of the gas formation has ceased [35] resulting in a slow removal of the remaining gases from the sample and completion of the GO to graphene transformation. Finally in region V; >450 °C, only the resultant graphene remains and the TGA profile very slowly tapers off due to oxidation and instrument drift, which is consistent with the remainder of the temperature profile. In the case of pure urea with no GO in the sample, the decomposition of urea would continue until approximately 600 °C, however due to the preferential reaction of the cyanic acid with the GO, the decomposition is complete much earlier.

The derivative of the mass loss clearly shows the step nature of the different regions. These results agree with previous TGA results of a GO/urea mixture [8] as well

as TGA results of just urea [36]. In this experiment, however, the slope of the mass loss is relatively constant across each region with sharp changes in slope at the boundaries as opposed to more defined humps in previous studies. The results showed a mass loss of 0.5% for region I followed by mass losses of 33.8, 18.6, 11.2, and 2.5% for regions II, III, IV, and V, respectively. This corresponds to no significant reactions in region I, followed by a very large mass loss in region II as the urea decomposes to form gaseous products, then another significant mass loss as the oxide groups of the GO are striped off by the cyanic acid in region III. Region IV shows a slow tapering of the mass loss as no more urea remains and the remaining oxide groups are removed completing the graphene transformation process, and finally a very slow decay of mass in region V that corresponds to the rate of mass loss for all other temperature cycles, and can be attributed to instrument drift.

3. GO and GO/urea 1:1 Major Differences

The differences between the pure GO and the GO/urea TGAs can be seen more clearly with the initial heat-up results from both samples presented together (Figure 23).

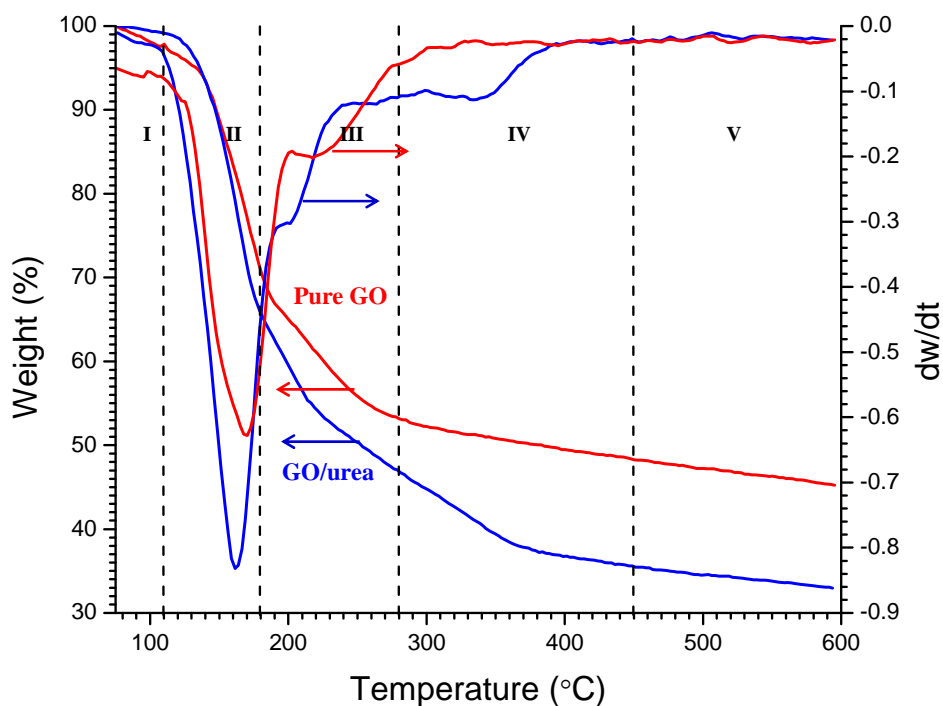


Figure 23. TGA of 1st derivative (dw/dT) of GO and GO/urea 1:1 overlay

When looking at the TGA derivative of the GO/urea mixture as compared with that of pure GO it is easy to see that the process begins slightly earlier in the case of GO/urea, and that the process ends slightly later. The earlier beginning is due to the decomposition of urea occurring at lower temperatures than the pyrolysis of oxygen containing functional groups of GO [14] and the later ending is due to the slow removal of all of the urea decomposition byproducts. It is also easy to see that the GO/urea mixture has five distinct regions while the pure GO has only four.

Furthermore, it is important to note the observation that the GO/urea mixture showed a significantly smaller volume expansion than the pure GO. This is hypothesized to be caused by the evolved gases from urea decomposition allowing the GO to expand slowly in a more controlled manor and remove the oxide groups by means of reducing agents. Whereas in the case of pure GO, the gaseous CO and CO₂ build pressure until eventually overcoming the Van der Waals forces and rapidly expanding the material and releasing gas.

B. MASS SPECTROSCOPY

Mass spectroscopy analysis was coupled with both of the TGA/DSC experiments performed understanding that there is a slight time delay between the TGA/DSC results and the mass spectroscopy results as it takes some finite amount of time for the released gases to traverse the coupling tube (seen in Figure 19) between the two instruments. According to the software this time delay is between 5 to 10 minutes and therefore during data processing the mass spectroscopy data has been shifted by 7.5 minutes (37.5 °C) to account for this delay. Naturally, the results showed a large concentration of mass-to-charge ratio (m/z) 40, which is attributed to the Ar atmosphere used for the experimentation. Additionally, there was no definitive indication of gases evolved after the initial heat-up, meaning that the resultant graphene was stable at least up to 800 °C. The results of the mass spectroscopy were analyzed using the NIST Mass Spectroscopy database and previous research involving mass spectroscopy of urea and its derivatives [36].

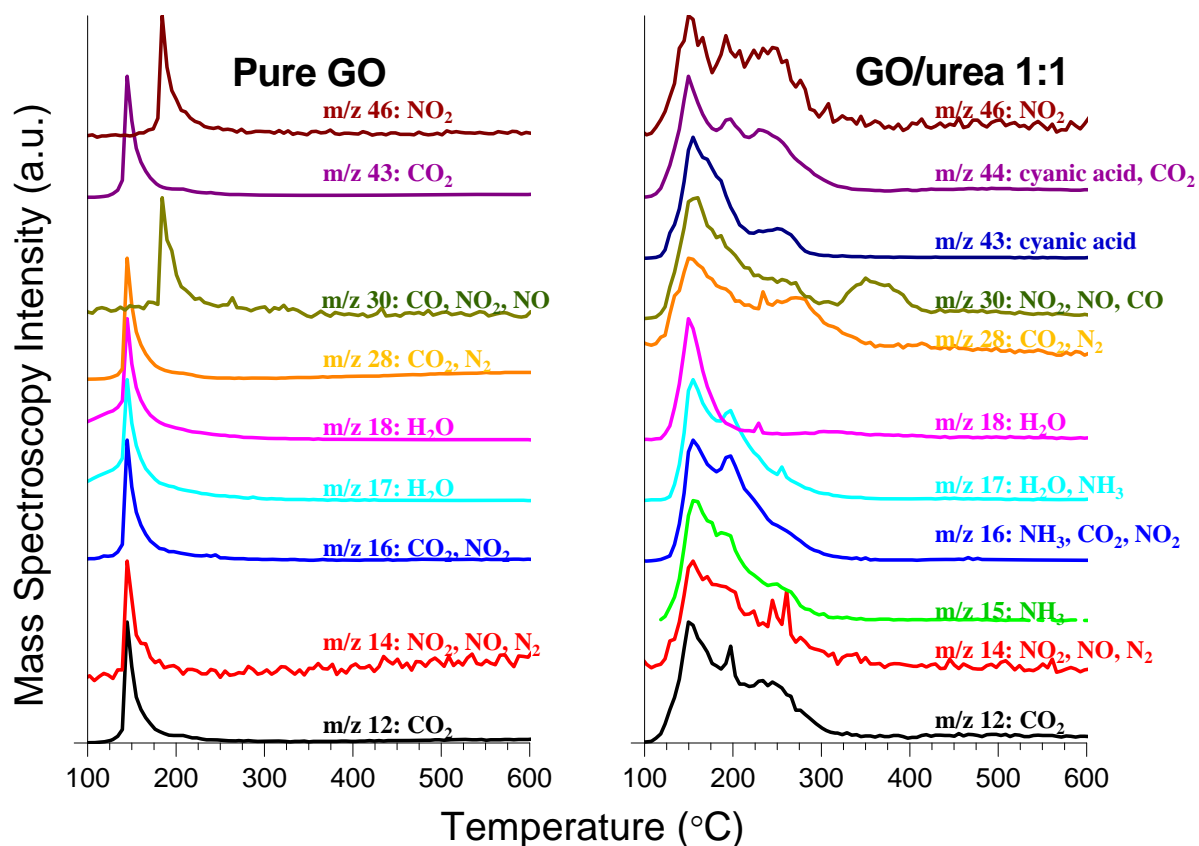


Figure 24. Mass spectroscopy results of Pure GO (left) and GO/urea 1:1 (right)

1. Pure GO

The mass spectroscopy results from pure GO were different from those obtained for the GO/urea mixture, as expected. Only a few characteristic gases were observed in the results, namely water vapor, CO, and CO₂.

In Figure 24 (left); m/z 15 and 43 were not present as they are associated with NH₃ and cyanic acid, respectively, and were therefore excluded from the plot for pure GO. All of the other ions detected are associated mainly with CO, CO₂, and H₂O. They all showed one large peak between 150 and 190 °C corresponding to the major mass loss shown in the TGA results for pure GO (Figures 22 [left] and 23). This rapid release of gas is due to the deoxygenation of the oxygen functional groups of the GO [37]. The water is presumed to be ambient water vapor that was desorbed from the sample surface.

Looking closely at Figure 24, it is evident that there is a very sharp release of gas from the bulk material followed by a broader tail to the peaks. The steep rise to the peaks represents the rapid expansion of GO and release of gases, while the broader decay of the peaks represents the slow diffusion of the trapped gases out of the material.

2. GO/urea 1:1

The mass spectroscopy results from the GO/urea mixture showed all of the expected gaseous species from the complex urea decomposition reaction, as well as some other species associated with removal of the GO oxide groups.

Starting with the highest m/z on the top of Figure 24 (right), m/z 46 is associated with NO_2 , which shows a small release of NO_2 throughout the thermal exfoliation process. As expected, m/z 44 shows production of cyanic acid from the decomposition of urea as well as production of CO_2 from thermal exfoliation of GO. It is also clear in m/z 43 that there are separate peaks of cyanic acid production from Equations (3.1) and (3.3), respectively.

The evolution of carbon and nitrogen containing gases is evidenced by m/z 30 and 28, both of which have a major peak during region II then subsequent peaks and tapering through regions III and IV. This is caused by the relatively slow stripping of the oxide groups of GO, which also adds to the production of NH_3 as shown in m/z 17 and 16. This correlation can clearly be seen by the second peak in m/z 44 (the third peak is attributed to cyanic acid as described above) aligning with the second peak of m/z 17, 16, and 12.

As shown by m/z 18, the H_2O is removed in one large peak just as in the case of pure GO. Comparing m/z 18, which is solely due to H_2O with m/z 17 and 16, it is clear that there are two separate peaks of NH_3 production as discussed earlier with the cyanic acid reaction with the oxygen groups of the GO.

Looking at just m/z 46 and 14, it is clear here that some nitrogen-containing gases are evolved during the transformation process, however at a much lower concentration than other products as evidenced by a comparison with m/z 16 which has contributions from NH_3 and CO_2 as discussed.

Of note is that m/z 16, 17 43, and 44 all of which have contributions from urea decomposition products, show similar structures as discussed previously as the transformation goes through several stages.

3. Nitrogen Containing Gases

One of the objectives of this study was to determine the stability of nitrogen doping of graphene by thermally exfoliating a GO/urea mixture. There was no evidence in the Raman spectroscopy data that nitrogen was leaving the graphene matrix at high temperatures, which seems to support the conclusion that the nitrogen doping is stable at least up to 800 °C in an inert argon atmosphere. In the mass spectroscopy results of the same temperature profile, any evolution of nitrogen can be directly observed. Figure 25 shows just m/z 14 and 16 for each temperature cycle under the associated TGA results for both pure GO and the GO/urea 1:1 mixture. As far as nitrogen containing gases, m/z 14 is associated with N₂, NO, and NO₂ while m/z 16 is associated with NO₂. Note that m/z 16 is also associated with CO₂, NH₃, and urea explaining the large profiles during the initial heat-up; however it is assumed that by the second temperature cycle these two compounds have been eliminated from the sample.

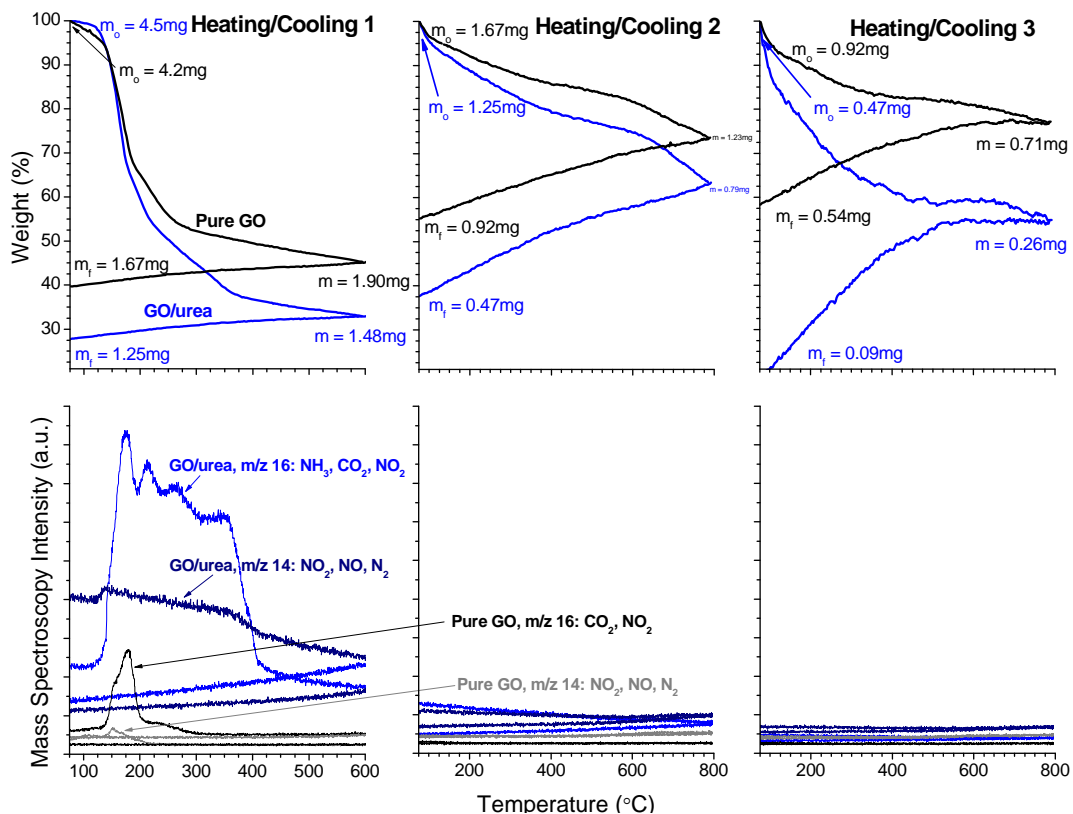


Figure 25. TGA results and mass spectra for nitrogen containing gases.

From Figure 25, it is very apparent that after the initial heat-up the amount of gases evolved from the sample (if any) is extremely low and is very difficult to distinguish over instrument noise and drift. Thus, there is no evidence that any nitrogen containing gases were evolved from the samples during the 2nd and 3rd heat-up during TGA/mass spectroscopy studies (Figure 26).

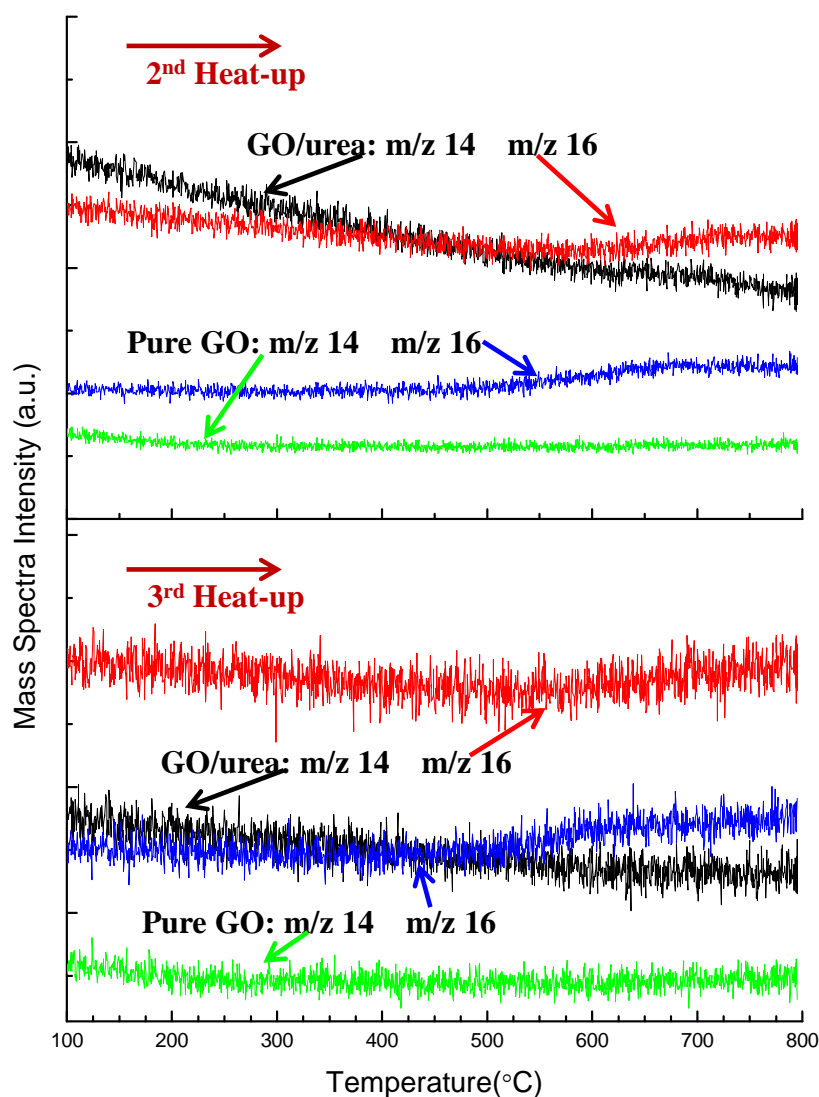


Figure 26. Mass spectra of nitrogen gases associated m/z for pure GO and GO/urea 1:1 mixture

The black and red spectra are the GO/urea mixture and the blue and green spectra are the pure GO sample. Due to the low levels of any gases being evolved and the high noise levels shown in Figure 26, no conclusions can be drawn from mass spectroscopy either way as to the stability of nitrogen in the graphene matrix at higher temperatures. In summary, mass spectroscopy results support the conclusions obtained from Raman spectroscopy. No evidence has been found as to nitrogen leaving the graphene at high temperatures.

C. DIFFERENTIAL SCANNING CALORIMETRY

Similar to TGA, the DSC data was corrected and processed into each temperature cycle for graphical display. The DSC data showed only instrument drift after the initial heat-up with no significant change in the sample and therefore only the DSC data from only the initial heat-up cycle is displayed (Figures 27 and 28). The DSC results of the coupled TGA/DSC experiments showed the same type of results that were observed in the TGA results, specifically four distinct regions of graphene transformation for pure GO and five regions for the GO/urea 1:1 mixture.

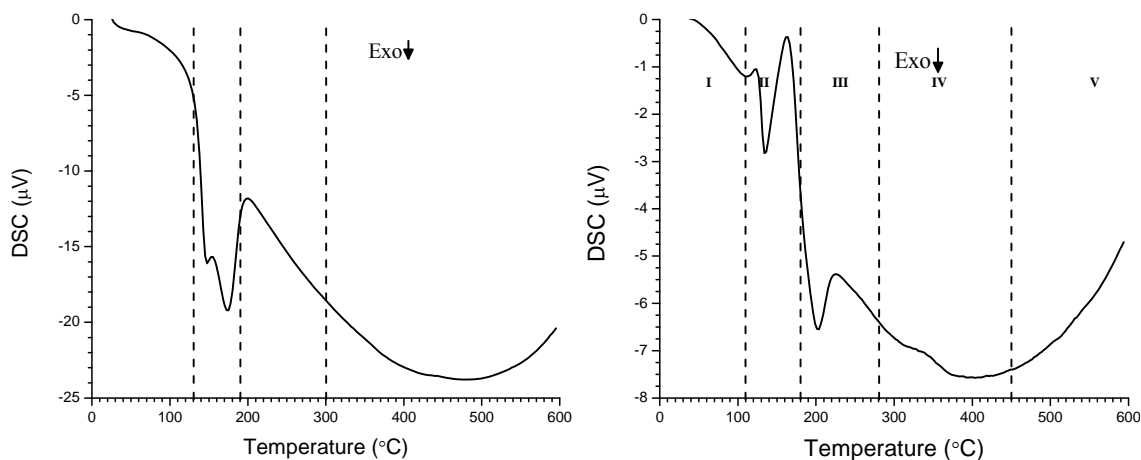


Figure 27. DSC initial heat-up results for (left) pure GO and (right) GO/urea 1:1

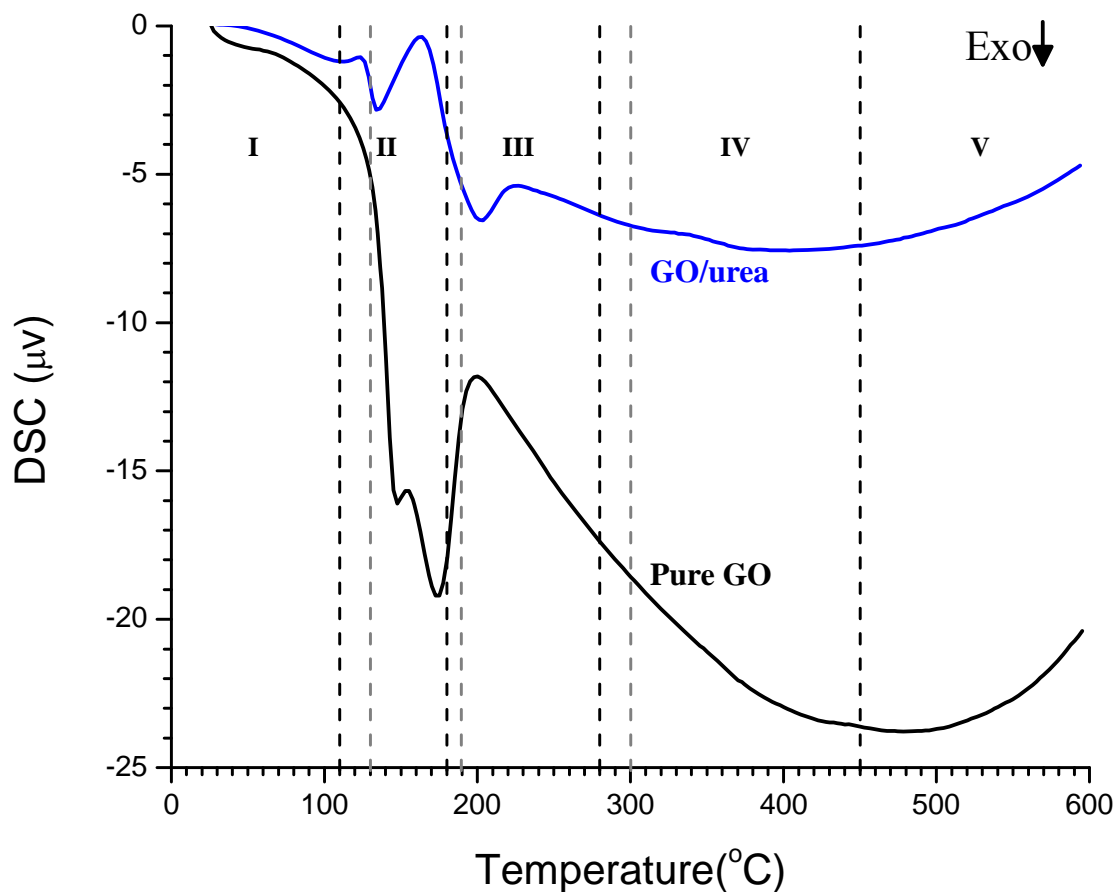


Figure 28. Combined DSC of initial heat-up for pure GO (black) and GO/urea 1:1 (blue)

1. Pure GO

As stated earlier, the thermal exfoliation of GO is a largely exothermic reaction as the oxide groups of the GO are removed and form CO and CO₂. The pure GO DSC results show this reaction as occurring in two exothermic peaks around 160 °C (Figures 27 and 28).

Prior to 130 °C, there are no significant changes in the sample. From 130–190 °C, the pure GO sample exhibits two distinct exothermic peaks. It is hypothesized that the first exothermic peak at 150 °C is mostly likely associated with the removal of the

surface oxide groups from the GO, while the second peak at around 175 °C is associated with the large removal of oxide groups from the bulk of the sample. This behavior of two separate instances of CO and CO₂ formation; a small release followed by a much larger release, was not conclusively observed in the mass spectroscopy results, however the mass spectroscopy results were not definitive either way due to instrument noise as very low levels. With a larger heat-up rate these would merge into a single exothermic peak [37]. The DSC results do not show any significant reactions above 200 °C as the remnant oxide groups are removed and the gases escape the material, however there is a slow, small third release in CO and CO₂ that was observed in mass spectroscopy.

2. GO/urea 1:1

Unlike the thermal exfoliation of pure GO, the thermal exfoliation of GO/urea is a largely endothermic reaction due to the decomposition of urea being endothermic. In region I there is no significant change in the sample. There is a small endothermic peak just after 100 °C associated with the beginning of urea decomposition followed by a much larger endothermic peak just past 150 °C associated with the melting point of urea [8] and the urea decomposition to produce ammonia and cyanic acid. Then in region III there is another small endothermic peak as cyanic acid reacts with the oxygen groups of the GO. Region IV shows a very small endothermic “bump” as the remnant cyanic acid reacts with the remnant oxygen groups completing the transformation to graphene, and finally in region V all reactions are complete with only instrument drift remaining in the DSC results.

Combining the DSC results for the GO/urea mixture and the pure GO (Figure 28), it is apparent that the GO/urea to graphene transformation begins at a slightly lower temperature associated with the urea decomposition, and it is not complete until a higher temperature. Note that in Figure 28, the black dashed lines and region labels correspond to the transformation regions of the GO/urea mixture while the dashed gray lines correspond to the transformation regions of pure GO.

Figure 28 also highlights the differences between the exothermic reaction of pure GO and the endothermic reaction of the GO/urea mixture. This result further supports the

previous assumption that the GO/urea to graphene transformation seems to be a slower and more controlled reaction than the rapid stripping of oxide groups from thermal exfoliation of pure GO.

D. X-RAY DIFFRACTION

XRD analysis was used to characterize the structure of the GO that was produced by the method described in section II.A.1. This measurement was completed by LT Ashley Maxson as part of NPS professor Luhrs' research group using the parameters listed in Table 4. The results from the analysis (Figure 29) were consistent with those observed by previous research that performed XRD analysis on GO produced via the Hummer's method (Figure 30) [8], [38].

Table 4. XRD measurement parameters.

<i>Parameter</i>	<i>Value</i>	<i>Unit</i>
Start	5.01	°2 θ
End	69.99	°2 θ
Step size	0.02	°2 θ
Scan Step Time	1	Sec
Scan Type	Continuous	
Cu-K α -1	1.54060	Å
Cu-K α -2	1.54443	Å
K α -1/K α -2 Ratio	0.5	

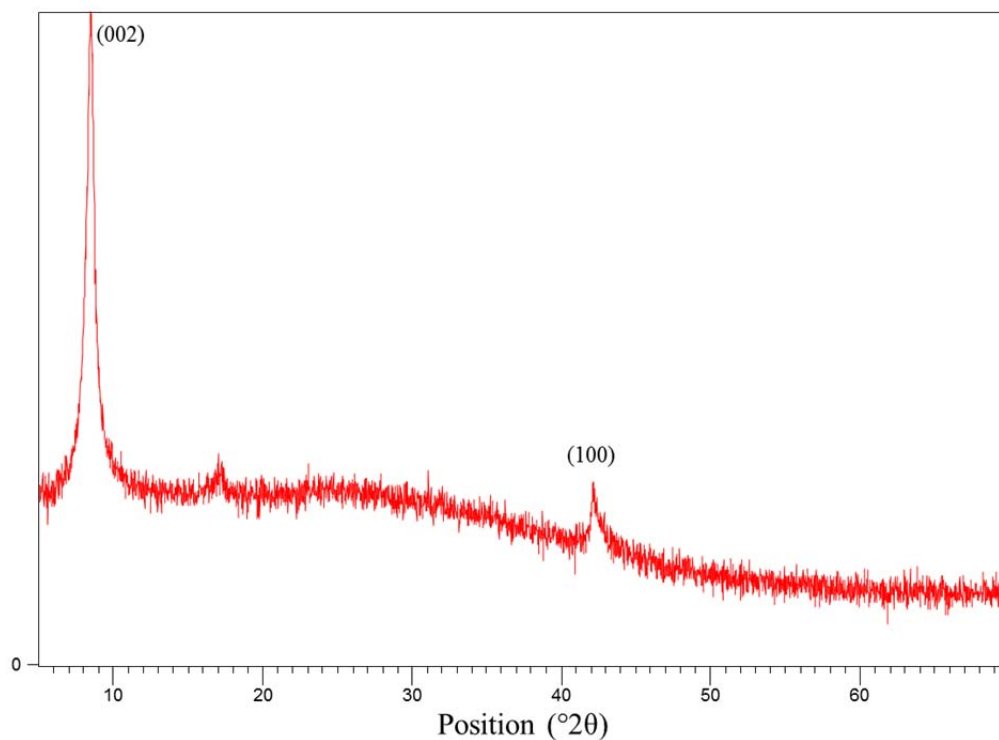


Figure 29. XRD results on produced GO powder.

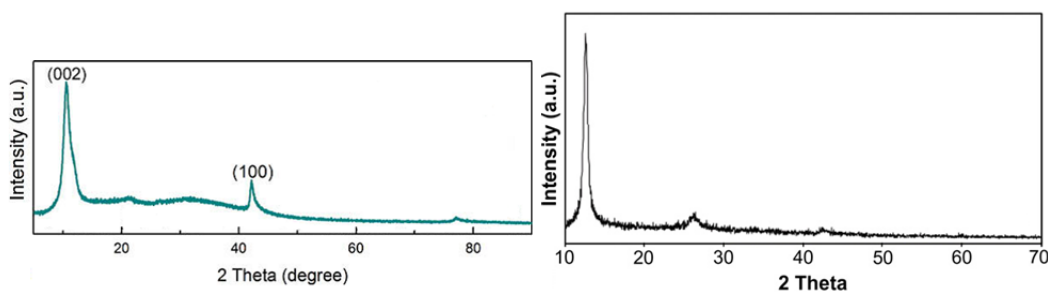


Figure 30. XRD of GO and other materials (From [38] left, [8] right).

Comparing the top XRD spectra of GO in both the left and right panels of Figure 29 to the spectra in Figure 30, it is easily seen that the GO produced in this study is of a very similar structure. There is the characteristic (002) peak at $2\theta = 10^\circ$ which is caused by the oxide functional groups and a much smaller (100) peak at $2\theta = 43^\circ$ caused

by the hexagonal structure of carbon. This study is not focused on XRD analysis, however it was important to confirm that the GO used throughout this study is in fact pure GO.

E. RAMAN SPECTROSCOPY

The measure Raman spectra were curve fit into four curves using the Renishaw Wire 3.2 software (Figure 31). The two main peaks of the Raman spectra are each separated into two peaks; D1, D2, G1, and G2. The D-band is caused by vibrations of the hexagonal ring structure of the carbon atoms and becomes Raman active when defects are present in that structure. The G-band however is caused by vibrations of the carbon-carbon bonds and is essentially unaffected by defects. Therefore, the D/G-band ratio gives a good indication of the structure of the material and the relative number of defects present. Figure 31 shows how the two main peaks in the Raman spectra are broken down into the D1, D2, G1, and G2 peaks and the summation of these peaks providing a good approximation of the Raman spectra.

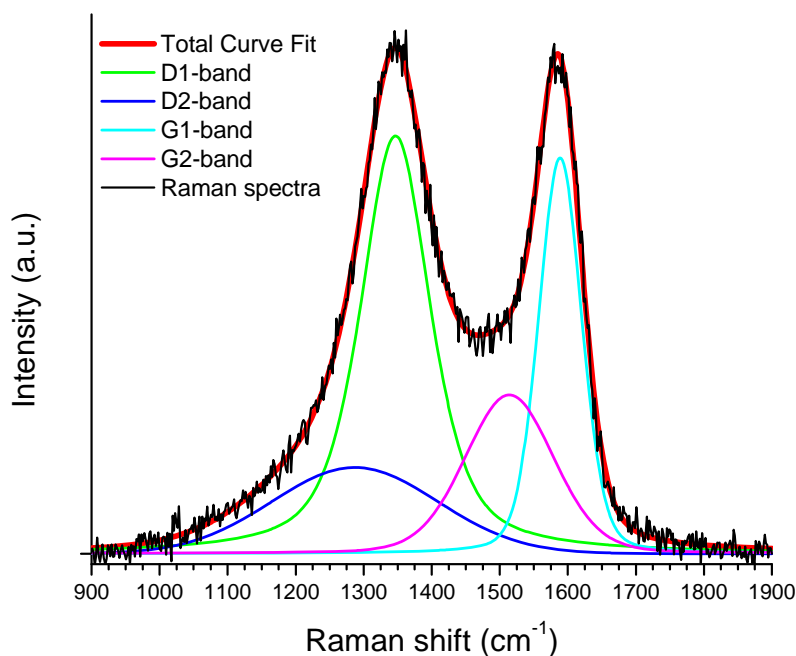


Figure 31. Curve Fitting of an arbitrary graphene sample Raman spectra

1. Determination of Nitrogen Doping

One of the objectives of this study was to conclusively show that thermal exfoliation of a GO/urea mixture will produce nitrogen doped graphene. In order to determine if this statement is true, a series of Raman spectra were recorded on graphene produced from thermal exfoliation of GO/urea mixtures of varying content. The parameters used for these Raman experiments were the same as listed in Table 2. GO/urea weight ratios of 0.3, 1.0, 2.0, 2.5, 4.0, and 5.0 were studied as well as simply thermally exfoliated GO and pure GO prior to any exfoliation.

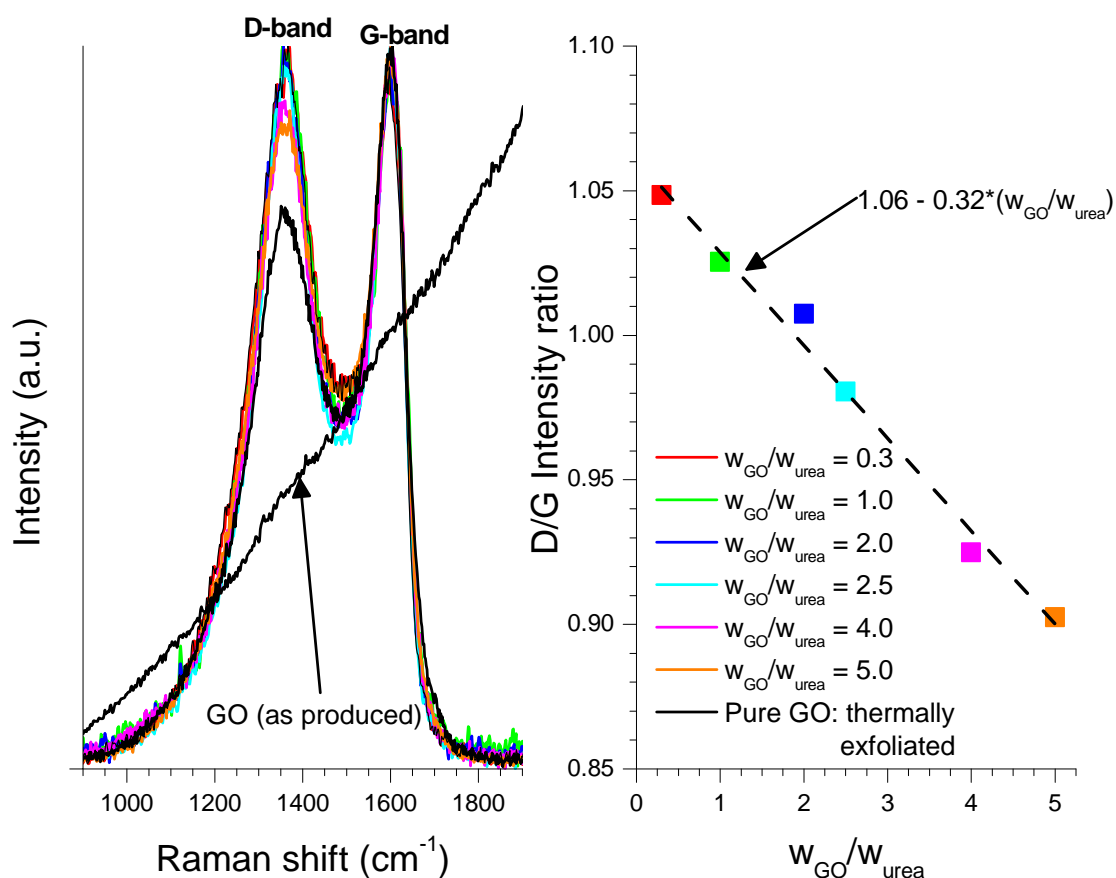


Figure 32. Raman spectra of varying GO/urea concentrations.

Figure 32 shows that there is a direct relationship between the D/G intensity ratio and the GO/urea concentration used to produce graphene. This is due to the more urea that is used will result in a higher level of nitrogen doping and therefore a higher number

of defects in the graphene crystal lattice due to the insertion of nitrogen atoms. This larger number of defects gives rise to a much higher D-band intensity while the G-band intensity is essentially unaffected by the defects. Due to the limited number of data points a simple linear regression was used in Figure 32 to illustrate this point understanding of course that the true behavior of the D/G intensity ratio is more complex. The D/G intensity ratio should approach a value of 0.78 as was measured for thermally exfoliated pure GO (black spectra in Figure 32) as the amount of urea in the sample is decreased to zero.

This part of the study shows that nitrogen is inserted into the crystal lattice when thermally exfoliating a GO/urea mixture to produce graphene. In order to further study the thermal exfoliation process, a GO/urea 1:1 mixture was chosen to perform an *in situ* study to determine if the nitrogen doping (via defect formation) process can be observed during the thermal exfoliation process.

2. GO/urea 1:1 Experiment 1

Raman spectra were recorded every 25 °C while heating a sample of GO/urea 1:1 through the temperature profile shown in Figure 14. These spectra demonstrated both the characteristic shift in peak frequency with heating as well as a shift in D/G band intensity ratio as the GO was thermally exfoliated producing graphene.

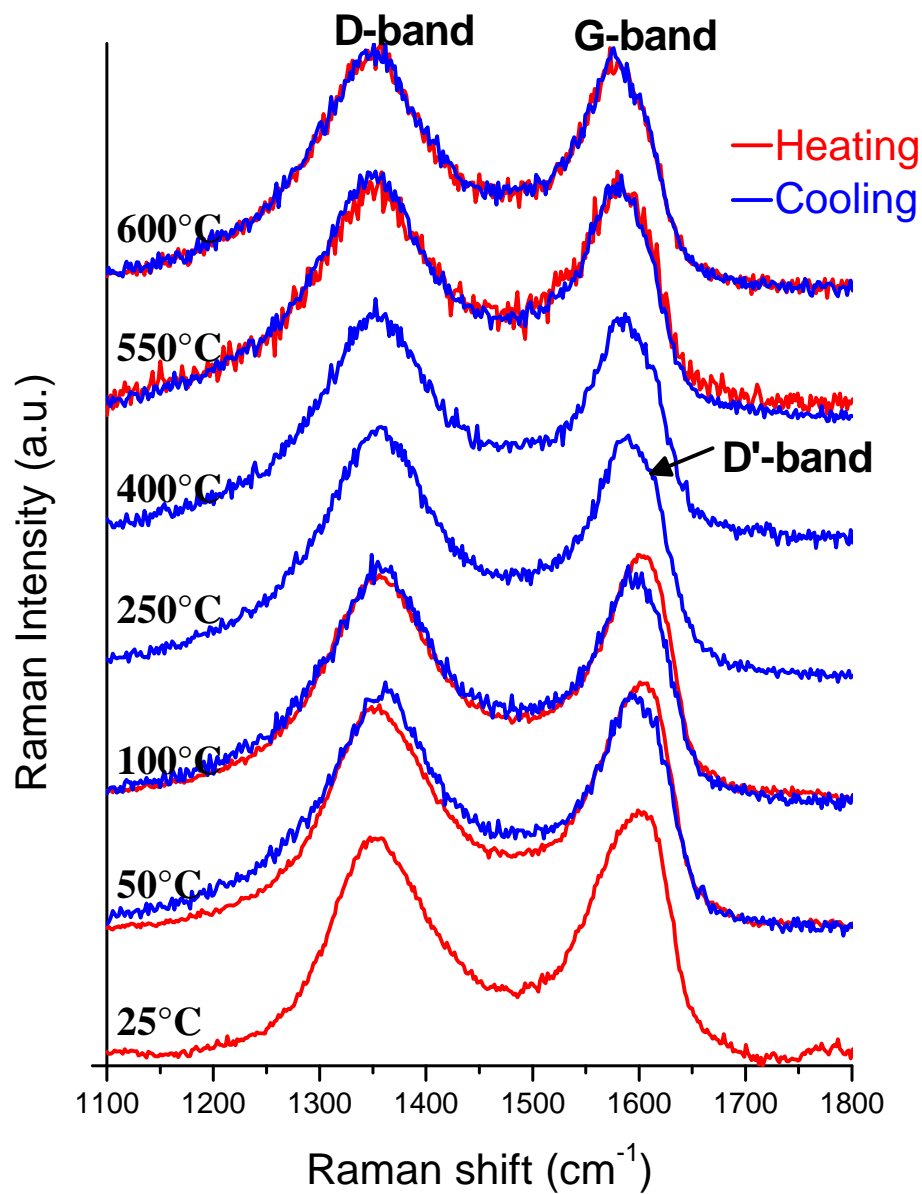


Figure 33. GO/urea Experiment 1, heating/cooling 1 Raman spectra

As shown in Figure 33, the centers of both the D and G-bands shift to the left at different rates as the temperature of the sample increases. Additionally, at 25 °C the GO/urea mixture has a Raman spectrum with the D-band intensity slightly lower than the

G-band intensity, while after heating the sample to produce graphene the Raman spectra shows a D-band intensity slightly higher than the G-band intensity. After the formation of graphene in the first heat-up of the temperature program, this D/G band intensity ratio remains approximately constant throughout the rest of the temperature program (Figures 34 and 35).

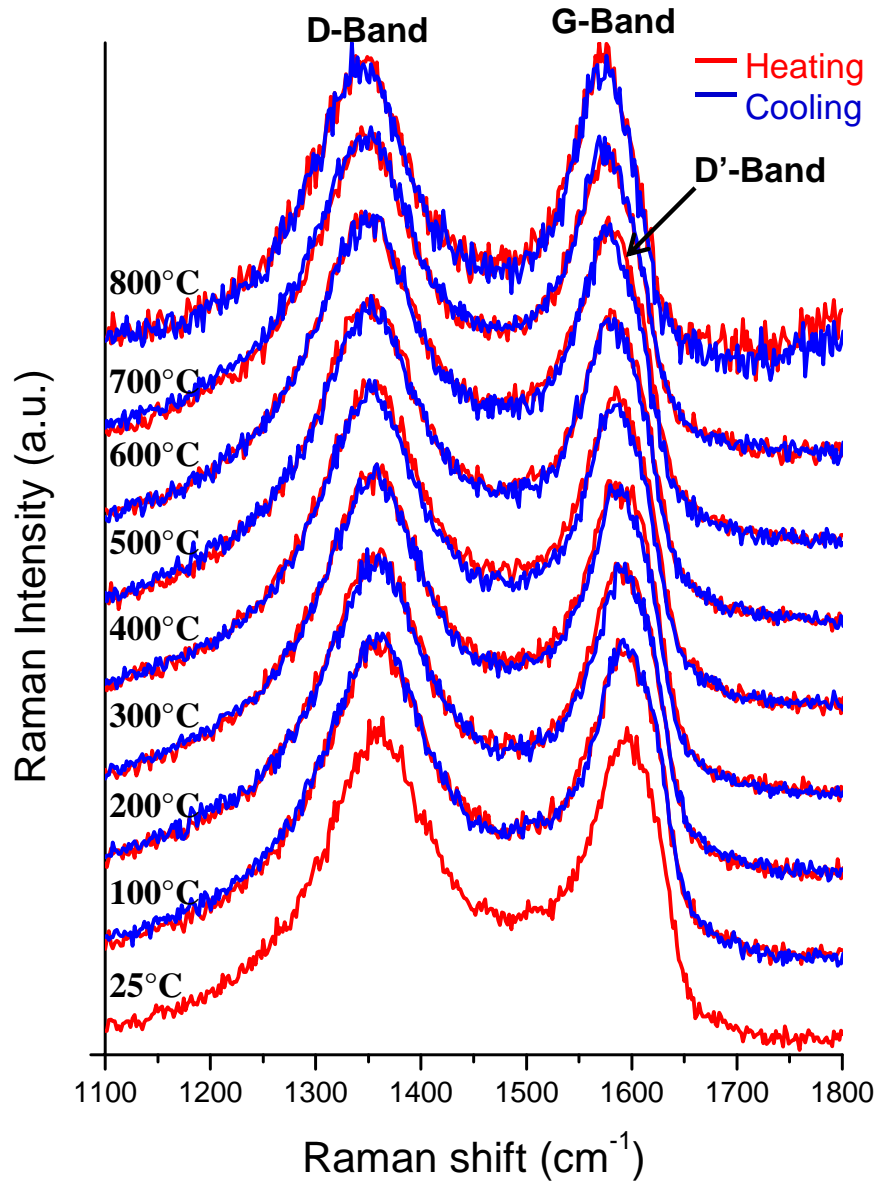


Figure 34. GO/urea Experiment 1, heating/cooling 2 Raman spectra.

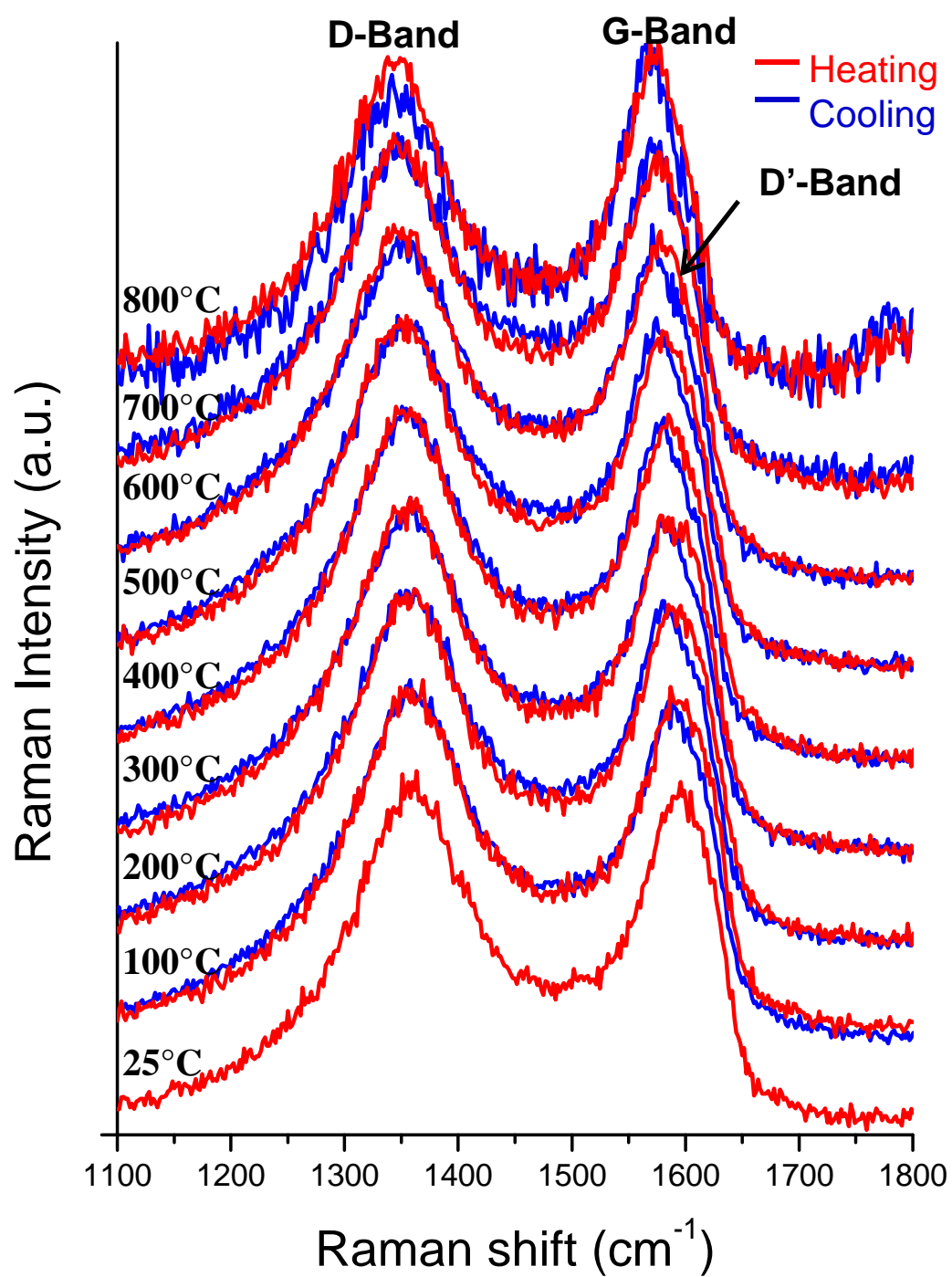


Figure 35. GO/urea Experiment 1, heating/cooling 3 Raman spectra.

The increase in noise level and difficulty in observing the D/G band intensity ratio in the 800 °C measurements in Figures 34 and 35 is attributed to the fact that at approximately 700 °C, the blackbody radiation gives rise to a significant background signal.

In Figure 33, the 150 °C Raman spectra is extremely noisy and no other measurements were observed until reaching 550 °C. This is due to the “fog” problem alluded to earlier. During this experiment, a noticeable “fog” was visually observed at 125 °C due to the decomposition of urea. As the urea in the sample decomposed, the gaseous byproducts described by Equations (3.1) through (3.3) were released into the stage atmosphere. This fog was first visually noticeable at 125 °C and the density progressively increased with increasing temperature. The 150 °C measurement was the last Raman spectra that still showed any recognizable peaks, albeit extremely noisy. The “fog” interfered with the Raman measurements both by scattering the laser off of the gaseous byproducts prior to reaching the sample and by making it impossible to visually focus the laser on the sample. The “fog” persisted until approximately 525 °C when it began to clear and then fully cleared by 550 °C at which point usable spectra were once again obtained.

Although the “fog” prevented the ability to obtain usable spectra during the actual formation process of graphene, the changes in the Raman spectra from a GO/urea mixture to graphene can be observed in the progression of spectra in Figure 33. This change is also seen by plotting curve fit data from each spectrum vs. temperature (Figures 36–38).

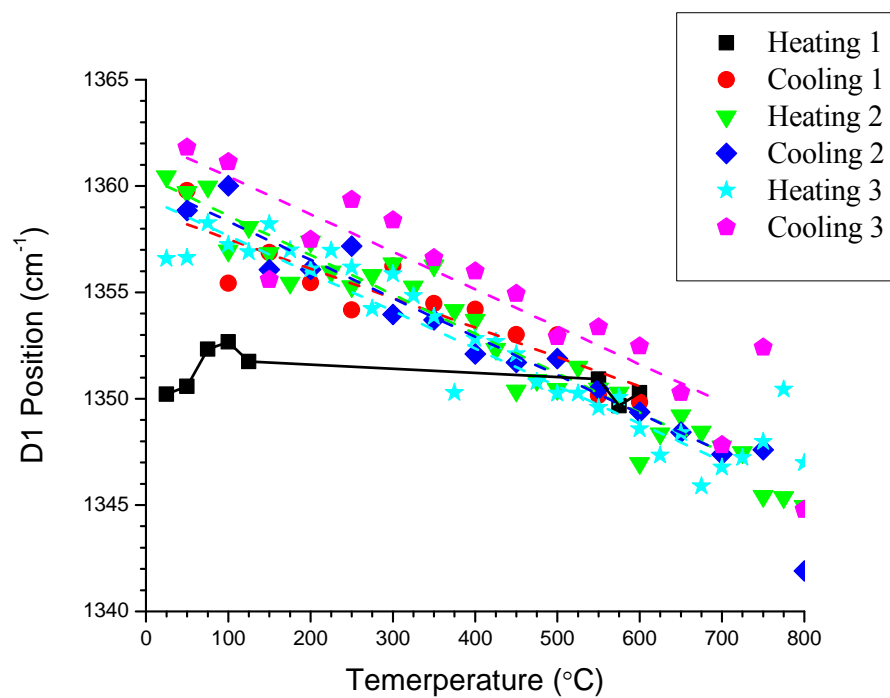


Figure 36. GO/urea Experiment 1, D1 Position.

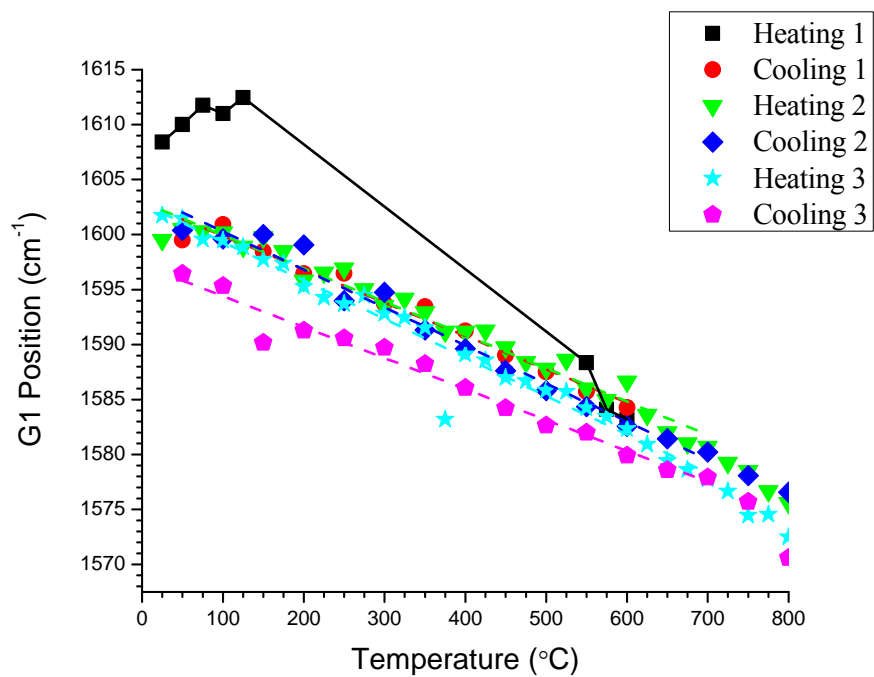


Figure 37. GO/urea Experiment 1, G1 Position.

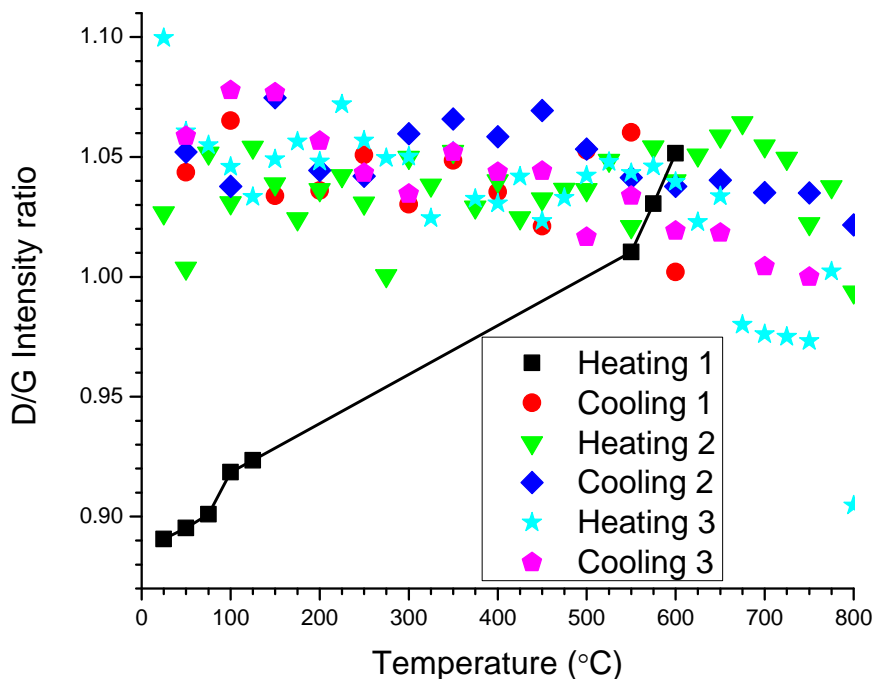


Figure 38. GO/urea Experiment 1, D/G intensity ratio.

Figures 36 and 37 show a linear shift in D1 and G1 band position, respectively, with temperature for all heating and cooling steps of the experiment with the exception of the initial heat-up, which forms graphene. Due to the fact that there was such a large gap in useable spectra for the initial heat-up, the exact behavior of the D1 and G1 band positions cannot be determined for the heat-up in this experiment.

Figure 38 displays a nearly constant D/G intensity ratio for all of the heating/cooling steps except the initial heat-up. As stated earlier, the deviation from the ratio of 1.05 when approaching 800 °C is attributed to a large increase in noise as a result of blackbody radiation. The beginning of the initial heat-up shows a significant difference in behavior than any other portion of the temperature program, and the end of the initial heat-up seems to correspond well with the behavior of the rest of the temperature program, however the “fog” prevented *in situ* observation of this change in behavior.

This experiment provided valuable insight into stability of the graphene during two thermal cycles from 25 to 800 °C, and to the characteristic difference between

Raman signatures of a GO/urea mixture and of resultant graphene. Specifically, the experiment proved that the GO/urea mixture undergoing thermal exfoliation exhibits the same increase in the D/G intensity ratio as pure GO undergoing thermal exfoliation [39]. Unfortunately, the intense “fog” prohibited an *in situ* of this GO/urea to graphene transformation which led to duplicating the experiment in order to obtain data during this transformation process.

3. GO/urea 1:1 Experiment 2

After the failure of Experiment 1 to provide useful data during the GO/urea-graphene transformation process, a duplicate experiment was performed using an extremely small amount of GO/urea sample with the objective to minimize the amount of gas formed during the reactions. All of the measurement parameters for Experiment 2 were the same as for Experiment 1 (listed in Table 2), and the same temperature profile was used for the first two temperature cycles. The third temperature cycle was not performed as the reduction in sample mass left too little material for the third cycle. The large reduction in sample mass in the initial heat-up is due to the decomposition and removal of urea and oxide groups which is followed by a slow reduction in sample mass in the subsequent heating/cooling cycles as discussed in the previous sections.

The Raman spectra of the initial heat-up of Experiment 2 showed the same shift in D and G-band positions as well as an increase in the D/G intensity ratio as temperature increases. Figure 39 shows this progression along with the deviation of the initial heat-up Raman spectra with the first cool-down.

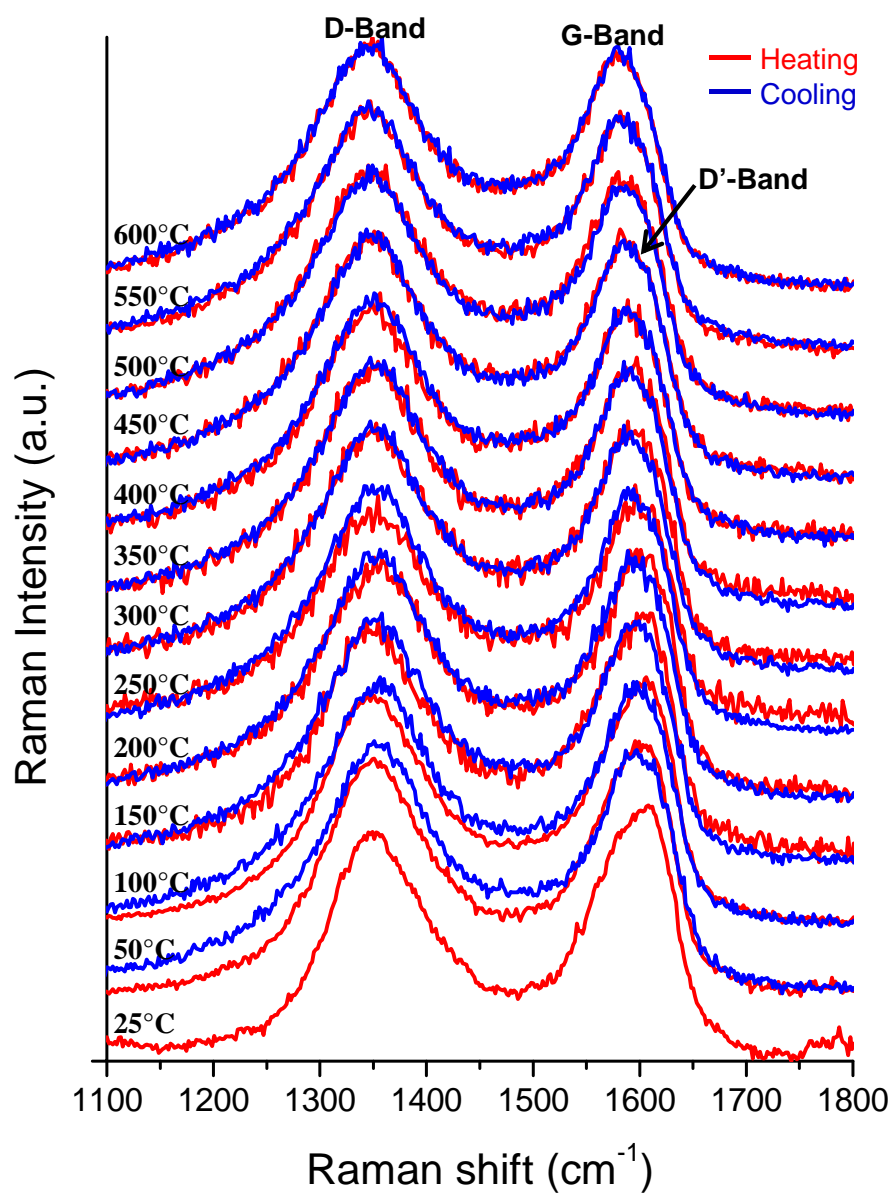


Figure 39. GO/urea Experiment 2, heating/cooling 1 Raman spectra.

The Raman spectra of the subsequent heating/cooling cycle (Figure 40) then showed a linear shift of the D and G-band positions with temperature as expected, but a nearly constant D/G band intensity ratio as the graphene formed by the initial heat-up has a very stable structure. The Raman spectra of both temperature cycles are then shown in parallel in Figure 41. This correlates with the data from Experiment 1 in that the GO/urea

to graphene transformation is completed during the initial heat-up and the material is mostly unchanged during subsequent temperature cycles. Once again, the Raman spectra become increasingly noisy as the temperature approaches 800 °C due to blackbody radiation and has been removed from Figure 41.

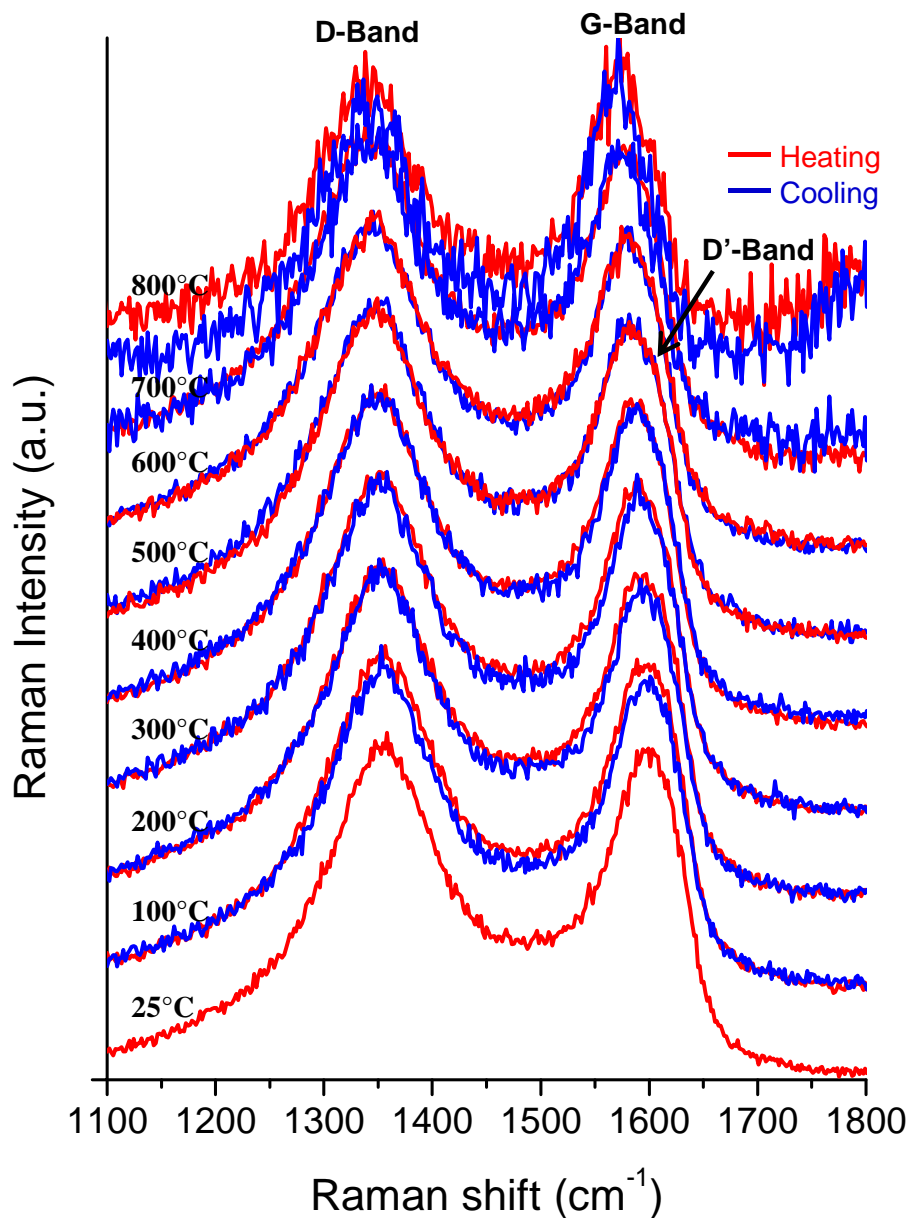


Figure 40. GO/urea Experiment 2, heating/cooling 2 Raman spectra.

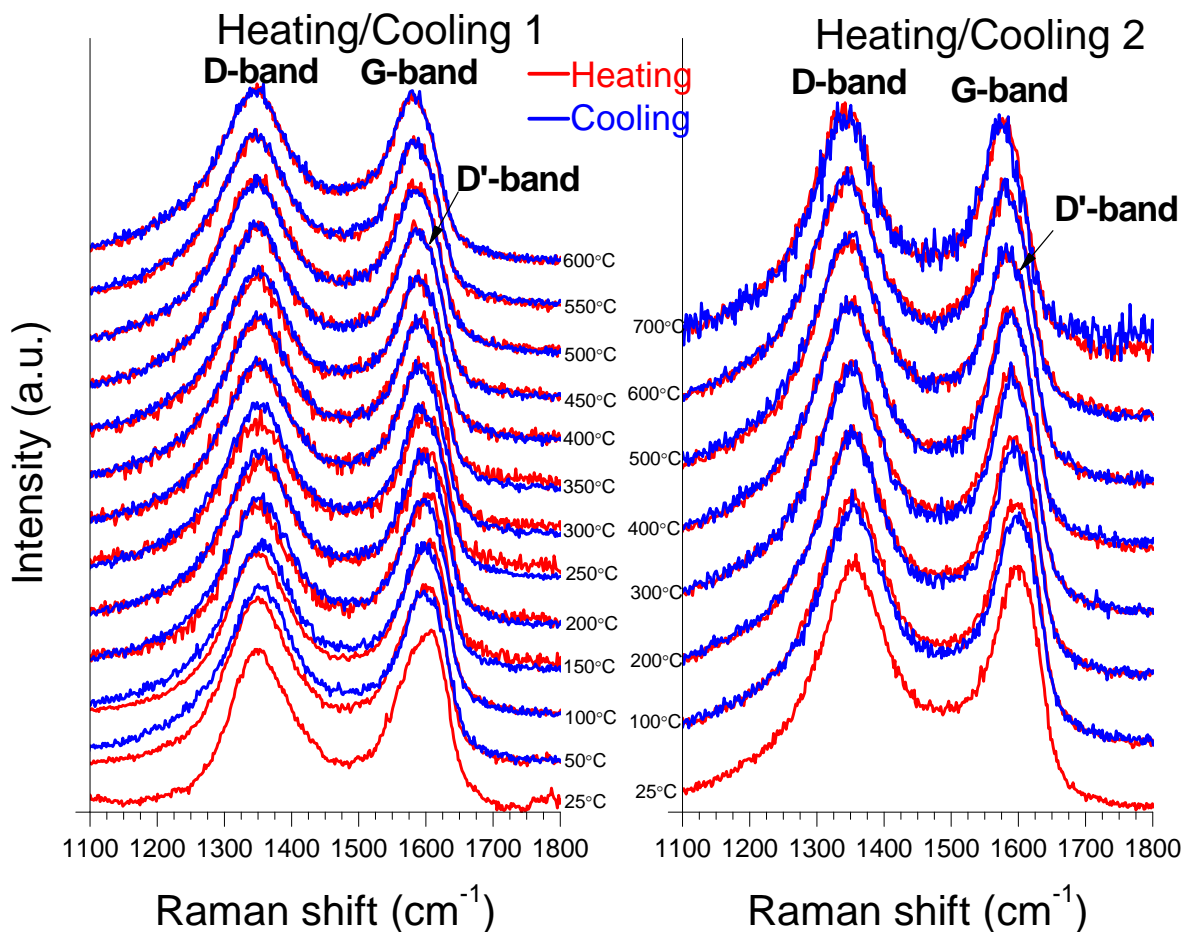


Figure 41. GO/urea Experiment 2 Raman spectra.

Figures 39 and 41 show a shift in the D/G band intensity as the GO/urea mixture is thermally exfoliated to produce graphene as well as a shift in D and G-band positions as the temperature is increased. There is also a characteristic change in the shape of the G band from the initial mixture to the resultant graphene that is attributed to the GO shedding its oxide groups in order to form graphene [24]. Figures 40 and 41 then demonstrate that the resultant graphene is very stable as the D/G band intensity ratio remains relatively constant as does the shape of the G-band. The only significant change is the linear shift in D and G band positions with temperature, as expected, due to the effect of temperature on lattice vibrations.

To obtain more quantitative data on the temperature-induced changes in the Raman spectra, curve fitting was performed.

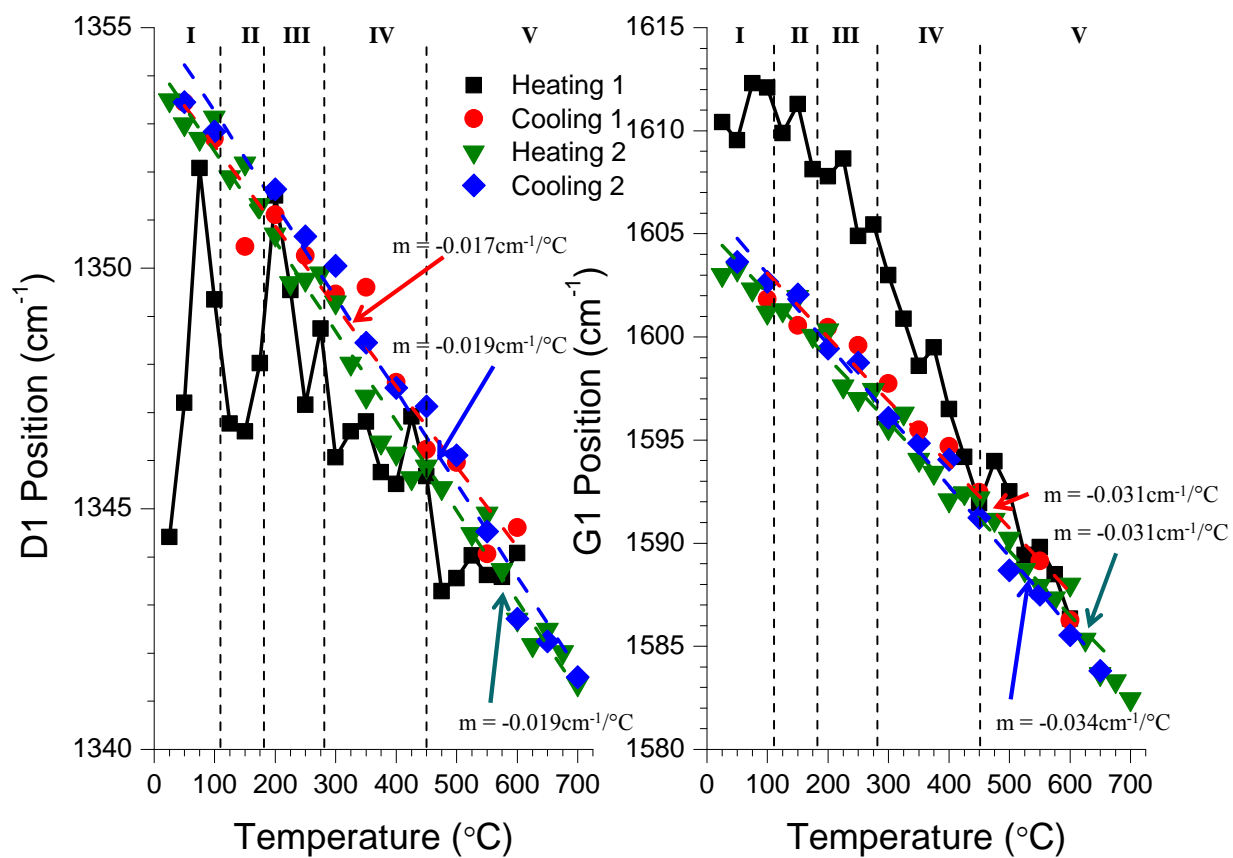


Figure 42. GO/urea Experiment 2, (left) D1 position and (right) G1 position.

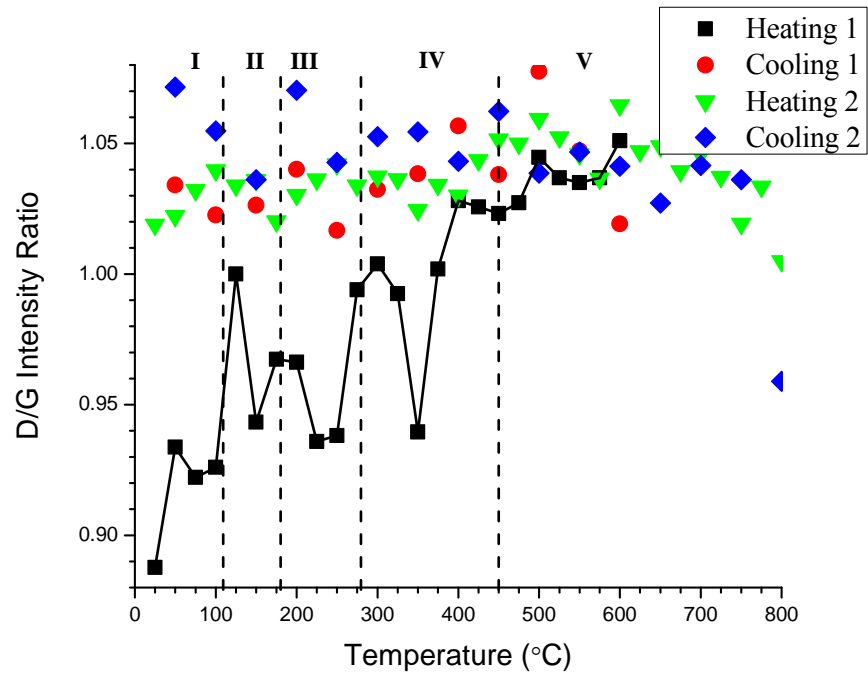


Figure 43. GO/urea Experiment 2, D/G intensity ratio.

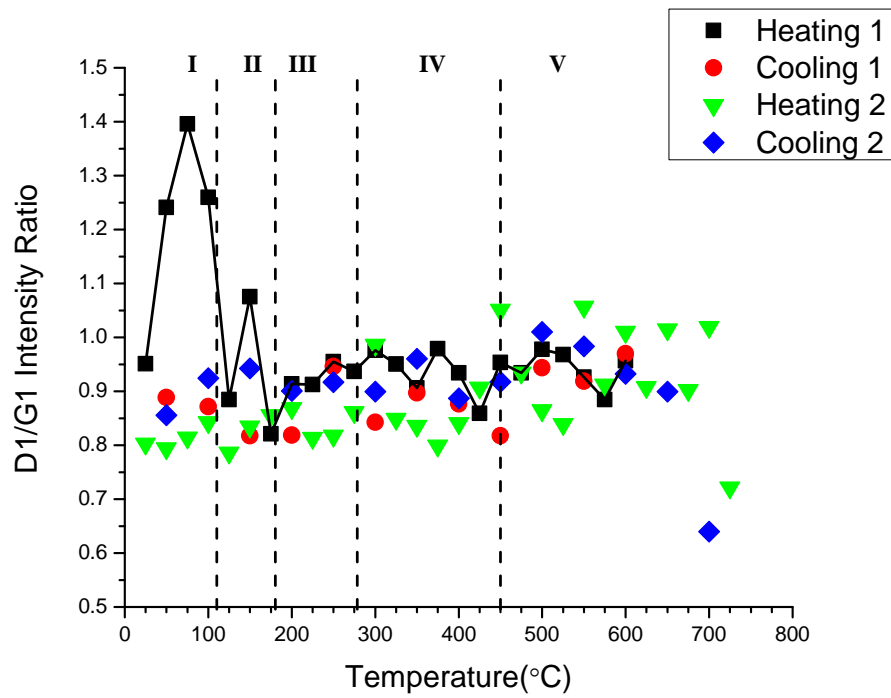


Figure 44. GO/urea Experiment 2, D1/G1 intensity ratio.

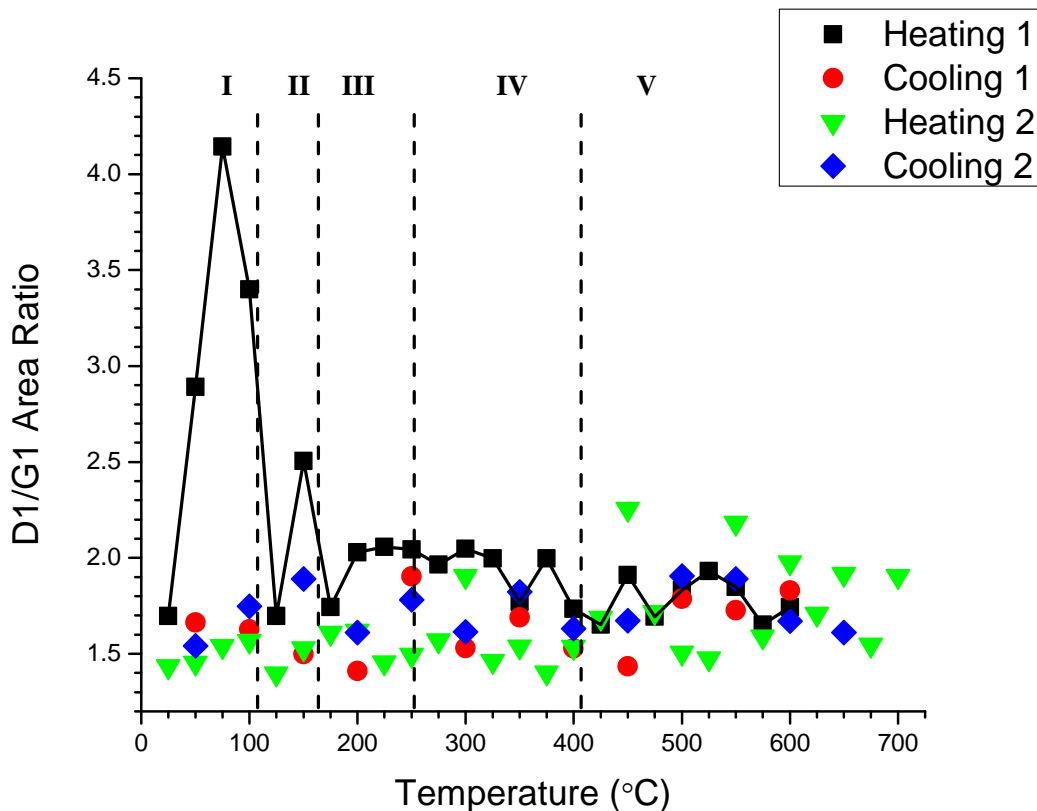


Figure 45. GO/urea Experiment 2, D1/G1 area ratio.

Similar to Experiment 1, data in Figure 42 shows a linear decrease in D1 and G1-band positions, respectively, as temperature increases after the initial heat-up, while Figures 43 and 44 show an almost constant D/G intensity ratio after the initial heat-up. Figure 45 also exhibits a constant behavior of D/G area ratio after the initial heat-up, and just as before the deviation from this behavior as temperature approaches 800 °C in Figures 43 and 44 is explained by a poor SNR as blackbody radiation increases after approximately 725 °C. The data after 725 °C for Figures 42 and 45 has been truncated for this reason. More interestingly in this experiment, the behavior of the initial heat-up of the material was not masked by “fog” and could be observed.

Starting with Figure 42 (right), it is apparent that the G1-band position during the initial heat-up follows a different behavior than throughout the rest of the experiment. For all subsequent temperature cycles, the G1-band position follows a linear behavior with a

slope between $-0.031 \text{ cm}^{-1}/^{\circ}\text{C}$ and $-0.034 \text{ cm}^{-1}/^{\circ}\text{C}$ (STDEV = 0.0017), while from 75°C to 450°C during the initial heat-up the G1-band position clearly does not follow this same linear behavior. This means that the transformation of the GO/urea mixture to graphene is contributing to the G1-band position shift during the initial heat-up while the linear behavior during all other temperature cycles can be attributed to temperature drift. The byproducts produced from the decomposition of urea and stripping of the oxygen groups contributes to the G1 peak at a slightly different Raman shift causing a slight upshift if the G1 position during the transition phase. Also, since the G1-band positions of the initial heat-up exhibit the same behavior of the other temperature cycles after 450°C , the transformation to graphene is complete by this temperature. The G1-band position trend is erratic during the transformation region and it is not possible to distinguish discrete steps as has been seen in TGA/DSC experiments with GO/urea [8] as well as in the TGA/DSC experiments.

The D1-band position in Figure 42 (left) also shows a linear behavior for all temperature cycles. The initial heat-up yielded a slope between $-0.017 \text{ cm}^{-1}/^{\circ}\text{C}$ and $-0.019 \text{ cm}^{-1}/^{\circ}\text{C}$ (STDEV = 0.0012). While the data is erratic during the initial heat-up, there are some signs of the complex structure of the graphene transformation process, with its completion at approximately 450°C , as the D1-band position of the initial heat-up assumes the same linear behavior observed for the other temperature cycles. In this case there is a significant contribution to the D1-band peak from the cyanic acid produced during the decomposition of urea [35]. Just as with the G1-band position, this contribution is at a slightly different Raman shift causing a large upshift in the D1-band position at the end of region I and beginning of region III. Although the data is too noisy for the D1-band position to analyze any discrete steps in the transformation process, it confirms again that the transformation process affects the Raman signature and is complete at approximately 450°C .

The D/G intensity ratios for all temperature cycles after the initial heat-up in Figure 43 shows an almost constant ratio of 1.039 (STDEV = 0.0175), while the initial D/G intensity ratio of the GO/urea mixture at 25°C is over 8 STDEV lower at 0.888. The D/G ratio then increases until reaching an average of 1.036 at 450°C . The data for the

D/G intensity ratio during this transformation phase is noisy which makes it impossible to discern any discrete steps of the transformation process.

Unlike the metrics and figures discussed to this point, the D1/G1 intensity ratios and the D1/G1 area ratios in Figures 44 and 45, respectively, show more discrete steps of the graphene transformation process. Regions I, II, III, IV, and V in Figures 44 and 45 directly correlate to TGA/DSC results and define the transformation process of the GO/urea mixture to graphene discussed earlier. In region I, there is a significant amount of Raman return due to the as produced GO present in the sample prior to thermal exfoliation (Figure 32). While in region II, the “fog” inhibited data collection in Experiment 1, in Experiment 2 the evolved gas from urea decomposition was noticeable, but did not inhibit Raman measurements. There is a local peak in both the D1/G1 intensity ratio and the D1/G1 area ratio at 150 °C corresponding to a rapid rise in cyanic acid as the urea decomposes. Here, the large contributions from ammonia and cyanic acid discussed earlier causing a large upshift in the D1-band position and a smaller upshift in the G1-band position also causes large peaks in the D1/G1 intensity and area ratios. The evolution of gaseous ammonia aids in the expansion of the GO resulting in a slightly changing shape of the G-band Raman peak which can be seen in Figures 39 and 41 (left). It is important to note here that the *in situ* Raman spectroscopy seems to be more sensitive to the beginning of urea decomposition than do other characterization techniques based upon the observation that the large peaks in D1/G1 intensity and area ratios occur just at the end of region I and into region II. In region III; 180 °C to 280 °C, the cyanic acid produced from the initial urea decomposition begins stripping of the oxide groups aiding in the formation of graphene which combined with the sustained production of gas helps to expand the GO and overcome the Van der Waals forces between layers resulting in graphene formation. This is seen in Figure 45 by a slight increase in the D1/G1 area ratio as the graphene formation continues and also in Figures 39 and 41 (left) by the fact that shape change of the G-band is complete by 300 °C. There is also a corresponding rise in the D1/G1 intensity ratio in Figure 44, however the intensity ratio in region III of the initial heat-up does not rise as dramatically as it does in the area ratio. Once again it seems as though the *in situ* Raman spectroscopy is more

sensitive than other techniques as the peaks in D1/G1 intensity and area ratios occur near the end of region II and into region III. Then in region IV; 280 °C to 450 °C, there is essentially no urea remaining and all of the gas formation has ceased [35] resulting the D1/G1 area ratio slowly dropping from 2.0 to 1.7. Finally in region V; >450 °C, only the resultant graphene remains and in assumes consistent behavior throughout the remaining temperature profile.

THIS PAGE INTENTIONALLY LEFT BLANK

IV. CONCLUSION

The synthesis of graphene through the thermal exfoliation of GO is a complex, multistep process, which is further complicated by the addition of urea for nitrogen-doping. In addition to nitrogen doping, the use of urea leads to enhanced process control.

This study employed several different *in situ* techniques to study this transformation process including TGA, DSC, mass spectroscopy, and most notably that of Raman spectroscopy, which proved to be a valuable tool to observe the various stages of the transformation process.

Based on the results obtained in this study, the transformation of a GO/urea mixture to graphene is believed to occur in the following steps:

- Urea decomposes into cyanic acid and ammonia aiding the expansion of the GO
- The cyanic acid undergoes several different reactions including reducing the GO producing additional ammonia and evolving CO₂. This additional gas allows for further expansion of the GO overcoming the Van der Waals forces between graphene layers producing graphene.
- The remaining products slowly decompose leaving just the stable graphene as the product.

Furthermore, the transformation of pure GO can be characterized by the following steps:

- GO sheds the oxide groups on the surface of the material resulting in a small emission of CO and CO₂
- The bulk of the GO sheds the oxide groups resulting in a massive and dramatic release of CO and CO₂ coupled with a very rapid volume expansion.
- The remaining gases in the material are slowly released leaving only the stable graphene as the product.

The findings of the complimentary technique of this study are very consistent with that of previously published research, however it was found that using a relatively low heating rate that there is a small release of gases from GO prior to the large release commonly observed in thermal exfoliation of pure GO. This is the first study however to

perform *in situ* Raman spectroscopy of the GO/urea to graphene transformation, the results of which correlated nicely with the results of the complimentary technique.

This study was able to show that the addition of urea does in fact produce nitrogen doping of the resultant graphene. The characteristic steps of graphene formation when thermally exfoliating a GO/urea mixture were observed via *in situ* Raman spectroscopy. The data obtained is promising as it suggests that Raman spectroscopy is an ideal characterization tool for studying the formation of graphene and characterizing the nitrogen doping level.

Our results also showed that the nitrogen content remains stable during subsequent temperature cycles, suggesting that nitrogen is indeed integrated into the graphene lattice rather than adsorbed at the surface.

LIST OF REFERENCES

- [1] A. K. Geim and K. S. Novoselov. “The rise of graphene.” *Nature Materials*, vol. 6, no. 3, pp. 183–191, Mar., 2007.
- [2] K. Novoselov, D. Jiang, F. Schedin, T. Booth, V. Khotkevich, S. Morozov, and A. Geim. “Two-dimensional atomic crystals.” *Proceedings of the National Academy of Sciences, U. S. A.*, vol. 102, no. 30, pp. 10451, Jul., 2005.
- [3] K. Novoselov, A. Geim, S. Morozov, D. Jiang, Y. Zhang, S. Dubonos, I. Grigorieva, and A. Firsov. “Electric field effect in atomically thin carbon films.” *Science*, vol. 306, no. 5696, pp. 666–669, Oct., 2004.
- [4] B. Partoens and F. Peeters. “From graphene to graphite: Electronic structure around the K point.” *Physical Review B*, vol. 74, no. 7, pp. 075404, Aug., 2006.
- [5] K. S. Novoselov, Z. Jiang, Y. Zhang, S. Morozov, H. Stormer, U. Zeitler, J. Maan, G. Boebinger, P. Kim, and A. Geim. “Room-temperature quantum hall effect in graphene.” *Science*, vol. 315, no. 5817, pp. 1379, Mar., 2007.
- [6] Y. Zhang, Y. W. Tan, H. L. Stormer, and P. Kim. “Experimental observation of the quantum hall effect and berry's phase in graphene.” *Nature*, vol. 438, no. 7065, pp. 201–204, Nov., 2005.
- [7] F. Schedin, A. Geim, S. Morozov, E. Hill, P. Blake, M. Katsnelson, and K. Novoselov. “Detection of individual gas molecules adsorbed on graphene.” *Nature Materials*, vol. 6, no. 9, pp. 652–655, Jul., 2007.
- [8] S. Wakeland, R. Martinez, J. K. Grey, and C. C. Luhrs. “Production of graphene from graphite oxide using urea as expansion–reduction agent.” *Carbon*, vol. 48, no. 12, pp. 3463–3470, May, 2010.
- [9] M. Burghard, H. Klauk, and K. Kern. “Carbon-Based Field-Effect transistors for nanoelectronics.” *Advanced Materials*, vol. 21, no. 25–26, pp. 2586–2600, Jul., 2009.
- [10] Y. M. Lin, H. Y. Chiu, K. A. Jenkins, D. B. Farmer, P. Avouris, and A. Valdes-Garcia. “Dual-gate graphene FETs with f_T of 50 GHz.” *IEEE Electron Device Letters*, vol. 31, no. 1, pp. 68–70, Jan., 2010.
- [11] C. Berger, Z. Song, X. Li, X. Wu, N. Brown, C. Naud, D. Mayou, T. Li, J. Hass, and A. N. Marchenkov. “Electronic confinement and coherence in patterned epitaxial graphene.” *Science*, vol. 312, no. 5777, pp. 1191–1196, May, 2006.

- [12] A. Dato, V. Radmilovic, Z. Lee, J. Phillips, and M. Frenklach. "Substrate-free gas-phase synthesis of graphene sheets." *Nano Letters*, vol. 8, no. 7, pp. 2012–2016, Jun., 2008.
- [13] S. Stankovich, R. D. Piner, X. Chen, N. Wu, S. B. T. Nguyen, and R. S. Ruoff. "Stable aqueous dispersions of graphitic nanoplatelets via the reduction of exfoliated graphite oxide in the presence of poly (sodium 4-styrenesulfonate)." *Journal of Materials Chemistry*, vol. 16, no. 2, pp. 155–158, Nov., 2006.
- [14] S. Stankovich, D. A. Dikin, R. D. Piner, K. A. Kohlhaas, A. Kleinhammes, Y. Jia, Y. Wu, S. B. T. Nguyen, and R. S. Ruoff. "Synthesis of graphene-based nanosheets via chemical reduction of exfoliated graphite oxide." *Carbon*, vol. 45, no. 7, pp. 1558–1565, Mar., 2007.
- [15] F. Li, J. Song, H. Yang, S. Gan, Q. Zhang, D. Han, A. Ivaska, and L. Niu. "One-step synthesis of graphene/SnO₂ nanocomposites and its application in electrochemical supercapacitors." *Nanotechnology*, vol. 20, no. 45, pp. 455602, Nov., 2009.
- [16] N. Liu, F. Luo, H. Wu, Y. Liu, C. Zhang, and J. Chen. "One-Step Ionic-Liquid-Assisted electrochemical synthesis of Ionic-Liquid-Functionalized graphene sheets directly from graphite." *Advanced Functional Materials*, vol. 18, no. 10, pp. 1518–1525, May, 2008.
- [17] X. Li, X. Wang, L. Zhang, S. Lee, and H. Dai. "Chemically derived, ultrasmooth graphene nanoribbon semiconductors." *Science*, vol. 319, no. 5867, pp. 1229–1232, Feb., 2008.
- [18] Z. S. Wu, W. Ren, L. Gao, J. Zhao, Z. Chen, B. Liu, D. Tang, B. Yu, C. Jiang, and H. M. Cheng. "Synthesis of graphene sheets with high electrical conductivity and good thermal stability by hydrogen arc discharge exfoliation." *American Chemical Society Nano.*, vol. 3, no. 2, pp. 411–417, Feb., 2009.
- [19] M. J. McAllister, J. L. Li, D. H. Adamson, H. C. Schniepp, A. A. Abdala, J. Liu, M. Herrera-Alonso, D. L. Milius, R. Car, and R. K. Prud'homme. "Single sheet functionalized graphene by oxidation and thermal expansion of graphite." *Chemistry of Materials*, vol. 19, no. 18, pp. 4396–4404, May, 2007.
- [20] H. C. Schniepp, J. L. Li, M. J. McAllister, H. Sai, M. Herrera-Alonso, D. H. Adamson, R. K. Prud'homme, R. Car, D. A. Saville and I. A. Aksay. "Functionalized single graphene sheets derived from splitting graphite oxide." *The Journal of Physical Chemistry B*, vol. 110, no. 17, pp. 8535–8539, Apr., 2006.
- [21] H. M. Ju, S. H. Huh, S. H. Choi, and H. L. Lee. "Structures of thermally and chemically reduced graphene." *Materials Letters*, vol. 64, no. 3, pp. 357–360, Nov., 2010.

- [22] T. Shen, W. Ge, K. Wang, M. Quan, J. Wang, W. Wei, and C. Koch. "Structural disorder and phase transformation in graphite produced by ball milling." *Nanostructured Materials*, vol. 7, no. 4, pp. 393–399, May, 1996.
- [23] A. Ferrari, J. Meyer, V. Scardaci, C. Casiraghi, M. Lazzeri, F. Mauri, S. Piscanec, D. Jiang, K. Novoselov, and S. Roth. "Raman spectrum of graphene and graphene layers." *Physical Review Letters*, vol. 97, no. 18, pp. 187401, Nov., 2006.
- [24] K. N. Kudin, B. Ozbas, H. C. Schniepp, R. K. Prud'Homme, I. A. Aksay, and R. Car. "Raman spectra of graphite oxide and functionalized graphene sheets." *Nano Letters*, vol. 8, no. 1, pp. 36–41, Dec., 2007.
- [25] D. Graf, F. Molitor, K. Ensslin, C. Stampfer, A. Jungen, C. Hierold, and L. Wirtz. "Spatially resolved raman spectroscopy of single-and few-layer graphene." *Nano Letters*, vol. 7, no. 2, pp. 238–242, Jan., 2007.
- [26] E. Smith, G. Dent, and J. Wiley, *Modern Raman Spectroscopy: A Practical Approach*. Hoboken, NJ: Wiley, 2005.
- [27] *The Nobel Prize in Physics 1930*, [Online, cited: 2012, Jul. 3]. Available: http://www.nobelprize.org/nobel_prizes/physics/laureates/1930/
- [28] T. Dieing, O. Hollricher, and J. Toporski. *Confocal Raman Microscopy*. Berlin, Heidelberg: Springer-Verlag Berlin Heidelberg, 2010.
- [29] P. Larkin. *Infrared and Raman Spectroscopy; Principles and Spectral Interpretation*. Waltham, MA: Elsevier, 2011.
- [30] P. M. Morse. "Diatomic molecules according to the wave mechanics. II. vibrational levels." *Physical Review*, vol. 34, no. 1, pp. 57–64, Jul., 1929.
- [31] Y. Shen. "Distinction between resonance Raman scattering and hot luminescence." *Physical Review B*, vol. 9, no. 2, pp. 622–626, Jan., 1974.
- [32] *UV Raman Spectroscopy*, [Online, cited: 2012, Jul. 3]. Available: <http://www.semrock.com/uv-raman-spectroscopy.aspx>
- [33] L. Panchakarla, K. Subrahmanyam, S. Saha, A. Govindaraj, H. Krishnamurthy, U. Waghmare, and C. Rao. "Synthesis, structure, and properties of boron-and nitrogen- doped graphene." *Advanced Materials*, vol. 21, no. 46, pp. 4726–4730, Dec., 2009.
- [34] W. S. Hummers Jr and R. E. Offeman. "Preparation of graphitic oxide." *Journal of the American Chemical Society*, vol. 80, no.6, pp. 1339, Mar., 1958.

- [35] P. M. Schaber, J. Colson, S. Higgins, D. Thielen, B. Anspach, and J. Brauer. “Thermal decomposition (pyrolysis) of urea in an open reaction vessel.” *Thermochimica Acta*, vol. 424, no. 1, pp. 131–142, Dec., 2004.
- [36] J. P. Chen and K. IsA. “Thermal decomposition of urea and urea derivatives by simultaneous TG/(DTA)/MS.” *Journal of the Mass Spectrometry Society of Japan*, vol. 46, no. 4, pp. 299–303, Jun., 1998.
- [37] K. Yin, H. Li, Y. Xia, H. Bi, J. Sun, Z. Liu, and L. Sun. “Thermodynamic and kinetic analysis of low-temperature thermal reduction of graphene oxide.” *Nano-Micro Letters*, vol. 3, no. 1, pp. 51–55, May, 2011.
- [38] Y. Li, W. Gao, L. Ci, C. Wang, and P. M. Ajayan. “Catalytic performance of Pt nanoparticles on reduced graphene oxide for methanol electro-oxidation.” *Carbon*, vol. 48, no. 4, pp. 1124–1130, Apr., 2010.
- [39] H. Wang, J. T. Robinson, X. Li, and H. Dai. “Solvothermal reduction of chemically exfoliated graphene sheets.” *Journal of the American Chemical Society*, vol. 131, no. 29, pp. 9910–9911, Jul., 2009.

INITIAL DISTRIBUTION LIST

1. Defense Technical Information Center
Ft. Belvoir, Virginia
2. Dudley Knox Library
Naval Postgraduate School
Monterey, California
3. Sebastian Osswald
Naval Postgraduate School
Monterey, California
4. Claudia Luhrs
Naval Postgraduate School
Monterey, California
5. Daphne Kapolka
Naval Postgraduate School
Monterey, California
6. Winford Ellis
Naval Postgraduate School
Monterey, California
7. William Sommer
Naval Postgraduate School
Monterey, California
8. Michael Mowry
Naval Postgraduate School
Monterey, California